Distribution Agreement

In presenting this thesis or dissertation as a partial fulfillment of the requirements for an advanced degree from Emory University, I hereby grant to Emory University and its agents the non-exclusive license to archive, make accessible, and display my thesis or dissertation in whole or in part in all forms of media, now or hereafter known, including display on the world wide web. I understand that I may select some access restrictions as part of the online submission of this thesis or dissertation. I retain all ownership rights to the copyright of the thesis or dissertation. I also retain the right to use in future works (such as articles or books) all or part of this thesis or dissertation

Signature:

______________________________________ ____________

David Stockwell Date

Interfacial Electron Transfer Dynamics between Organic Molecular Adsorbates and Semiconductor Nanoparticles

By

David Stockwell
Doctor of Philosophy

Chemistry

Dr. Tianquan Lian, Advisor

Dr. Michael C. Heaven, Committee Member

Dr. James Kindt, Committee Member

Accepted:

Lisa A. Tedesco, Ph.D.
Dean of the James T. Laney School of Graduate Studies

Date

Interfacial Electron Transfer Dynamics between Organic Molecular Adsorbates and Semiconductor Nanoparticles

By

David Stockwell

B.S., Marietta College, Marietta, OH, 2001

Advisor: Tianquan Lian, Ph.D.

An abstract of
A dissertation submitted to the Faculty of the
James T. Laney School of Graduate Studies of Emory University
in partial fulfillment of the requirements for the degree of
Doctor of Philosophy
in Chemistry
2010

Abstract

Interfacial Electron Transfer Dynamics between Organic Molecular Adsorbates and Semiconductor Nanoparticles

By David Stockwell

Interfacial electron transfer dynamics (ET) from photoexcited organic molecular adsorbates to semiconductor (SC) nanocrystalline thin films have been measured using ultrafast transient mid-infrared and visible spectroscopy. The various factors influencing variation in ET rates, such as the electronic nature of semiconductors, adsorbate driving force and formation of exciplex intermediates were investigated.

Dynamics of ET from C343 to TiO_2, SnO_2 and ZnO nanocrystalline films were compared in order to study the role of exciplex-mediated ET at molecule/semiconductor interfaces. The deactivation of C343 excited state and formation of oxidized C343 were measured by transient visible spectroscopy to follow the rate of charge separation across the interface, forming the exciplex. Dissociation of the exciplex to form free electrons in the semiconductors was probed by electron absorption in the mid-infrared. Charge separation rates were instrument response limited (< 150 fs) and ~1 ps for C343 on TiO_2 and SnO_2, respectively. The faster ET rate to TiO_2 than to SnO_2 is attributed to the higher density of conduction band states in the former. On ZnO, initial charge separation across the interface was shown to be instrument response limited (< 150 fs), but exciplex dissociation over ~12 ps was shown to determine the overall ET rate.

ET dynamics from oligoene dyes to TiO_2, SnO_2 and ZnO nanocrystalline films, and from fluorescein 548 to In_2O_3, SnO_2 and ZnO were compared in order to study both the semiconductor dependence on ET rate and the role of exciplex formation influencing electron diffusion into bulk SC. We show that the role of exciplexes is negligible in TiO_2, In_2O_3 and SnO_2 systems. On ZnO, the exciplex formation is suggested to be dependent on adsorbate coupling to surface states, where oligoene exciplex formation was shown to be instantaneous. Exciplex dissociation mediating electron injection into bulk ZnO is ~5 picoseconds, determining the overall ET rate. Results for fluorescein/ZnO indicate negligible exciplex formation, suggesting that ET is mediated by excited state deactivation, injecting electrons directly into the ZnO conduction band. For the dyes examined, the semiconductor dependence of ET rate follows the previously observed trend of $TiO_2 >> SnO_2 \sim In_2O_3 > ZnO$.

Interfacial Electron Transfer Dynamics between Organic Molecular Adsorbates and Semiconductor Nanoparticles

By

David Stockwell

B.S., Marietta College, Marietta, OH, 2001

Advisor: Tianquan Lian, Ph.D.

A dissertation submitted to the Faculty of the
James T. Laney School of Graduate Studies of Emory University
in partial fulfillment of the requirements for the degree of
Doctor of Philosophy
in Chemistry
2010

Acknowledgement

Without hesitation, I first offer my heartfelt thanks and appreciation to my advisor, Dr. Tianquan Lian, who has supported me throughout my graduate career with both his patience and knowledge while guiding my individual research and allowing me to contribute to the greater good of the group. Without his incentives to think critically and develop laboratory skills, I would not have achieved the levels of experimental consideration and analytical ability that I use to this day. This dissertation is a tribute to his continued support, without which it might have been left in vain. I also wish to extend my sincere thanks and appreciation to the members of my graduate committee, Dr. Michael Heaven and Dr. James Kindt, for both the valuable time and thoughtful advice that they have contributed to my research progress throughout the years.

The colleagues I have had the opportunity to work with have done nothing but further my interest in development of the tools for scientific research and increase the pleasure of discovering new things about the nature of the world. I especially thank Dr. Neil Anderson and Dr. Xin Ai, without the guidance of whom I would not have realized my potential in working with ultrafast lasers and the experiments they provide possible. Jier Huang has been an invaluable friend and colleague in working with my molecular systems, as has been Chantelle Anfuso, to whom I was proud to hand over the reins of laser control and the continuation of the SF project. Dr. Chunxing She and Dr. Jianchang Guo were instrumental in providing information and quality scientific discussion when I needed them most. Teddy Huang proved himself a true colleague every time that I needed semiconductor films, and a good friend

when it was required of him. Shengye Jin made himself available every time I requested fluorescence measurements, for which I thank him to no regard. I am also grateful for the contributions made by Dr. Abey Issac, Dr. Baohua Wu, Dr. Takayuki Kitamura, Dr. Guokun Liu, Rui Yuan, Aziz Boulesbaa, Dr. Wanhee Goh, Dr. Victor Lenchenkov and Issac Zhang. The work relationships and collaborations were always varied, but always ended in a result that was both productive and helpful.

I give great thanks to my entire family. My mother Beverly and father David have been both supportive and critical throughout my entire scholastic career, encouraging me to take every new step in stride, so that I can determine for myself what works and what doesn't. My brother Eric, who saw it fit to live with me for a year while at Georgia Tech, went out of his way to help out in designing laboratory electronics for our group and showed up to every Chemistry event I invited him to in his short Atlanta tenure. My sister Lynn has been understanding of my extended absences from home, and made every effort to stay in contact.

Finally, I thank my loving wife Rebecca, to whom this dissertation is dedicated. She could not have been more supportive and understanding during my graduate career were it asked of her. She has been by my side throughout the writing of my dissertation, encouraging me every step of the way, even as we moved throughout the country. I am wholeheartedly grateful for her dedication and encouragement.

Table of Contents

List of Figures

Chapter 1

Chapter 2

Chapter 3

Chapter 4

Chapter 5

Chapter 6

Chapter 7

List of Tables

Chapter 4

Chapter 5

Chapter 6

Chapter 1. Introduction

1.1. General Introduction

As a renewable, environmentally non-destructive energy source, solar energy has been of significant interest due to both the limitations in resources and environmentally degenerative by-products associated with fossil fuels. Conventional solar cells, created with silicon-based technologies, have shown promise in being a next step towards clean energy generation, although current efficiencies of solar-to-electric power conversion are limited to ~25%, and the production of such silicon solar cell arrays is relatively costly. Recently, alternative methods of harnessing solar energy utilizing charge-separation in multiple materials have been of significant interest. These hybrid solar cells, based on exciton generation and/or separation, show great promise for use as low-cost, high-efficiency energy substitutes, making them ideal for study as potential replacements for the current silicon-based technologies.[1-4]

Dye-sensitized solar cells (DSSC), one of the alternatives currently under investigation, consist of a nanoporous layer of wide band-gap semiconductor material covered in a layer of photosensitive molecules. Rather than utilizing charge separation at a p-n junction as in typical silicon solar cells, photoexcitation of the sensitizer molecules provides the driving force necessary for transport of the electron through the semiconductor as illustrated in Figure 1.1. After absorbing a photon from incident sunlight, the excited dye injects an electron into the conduction band of the nanoporous semiconductor if it is energetically favorable. The charge then diffuses to the conducting glass deposited on the anode and into the circuit. The oxidized dye is regenerated by the electrolyte, typically I^-/I_3^-, and the positive charge remaining in the electrolyte is carried to the cathode. The rate of charge transfer from the excited dye to accepting semiconductor is competitive with the rate of charge recombination back to the oxidized dye versus regeneration of the dye from the electrolyte, determining the overall efficiency of the DSSC. Ideally, a fast and high-yield charge separation from photoexcited dye to semiconductor is desired (Eq 1), where the timescale of charge recombination with the oxidized dye is much longer than the initial charge transfer (Eq 2)

$$dye - SC \xrightarrow{h\upsilon} dye^* - SC \xrightarrow{CS} dye^+ - SC^- \tag{1.1}$$

$$dye^+ - SC^- \xrightarrow{CR} dye - SC \tag{1.2}$$

where dye, dye^* and dye^+ represent the donor ground, excited and oxidized states respectively.

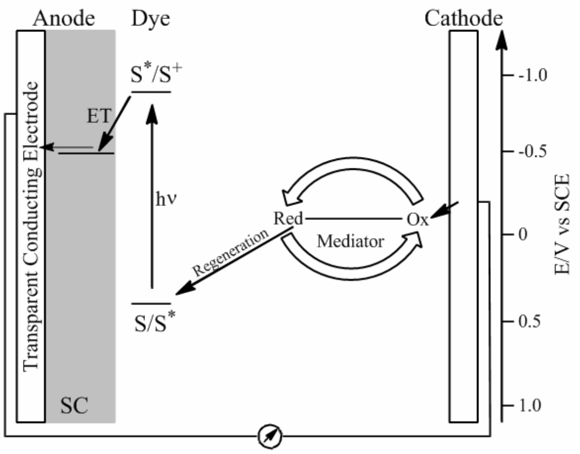

Figure 1.1. Working principle of a DSSC. Excitation of adsorbed dyes leads to electron injection to the nanoporous semiconductor substrate, after which the charges migrate to the conducting electrode and enter the circuit. The oxidized dyes are regenerated by a redox electrolyte (I^-/I_3^-), which is in turn reduced at the counterelectrode, completing the circuit.

Currently, the highest solar to electric conversion efficiencies of ~10% have been achieved in DSSCs based on Ru-(4,4'-dicarboxy-2,2'-bipyridine)$_2$(NCS)$_2$ (RuN3)-sensitized TiO_2 cells, with incident photon to current efficiencies (IPCE) near unity at absorption maxima.[1,5] The high IPCE in RuN3-based TiO_2 solar cells is attributed to ultrafast electron injection from photoexcited RuN3 to the TiO2 conduction band,[6-23] with a long-lived charge separation where the electron has a much slower rate of recombination with oxidized dye or redox mediator.[24-32] As well as TiO_2, other semiconductors such as In_2O_3, SnO_2 and ZnO have been studied in detail with RuN3 in order to investigate the effects of the accepting medium on the charge transfer mechanism.[33-40] It was observed that TiO_2 showed a biphasic injection mechanism, with an ultrafast (<100 fs) charge separation component of >50% and a slower component over several picoseconds. SnO_2 and ZnO showed much smaller ultrafast components and injection was dominated by the slower component (several picoseconds or longer), attributed to the conduction band characteristics of the particular semiconductor.[7]

To this end, interfacial electron transfer (ET) between adsorbed dyes and semiconductor nanoparticles has been a subject of intense research, both for improvement of DSSC efficiency and fundamental understanding of the underlying mechanisms involved in the electron transfer process.[41-44] Although poorly developed compared to ET in homogeneous solution,[45-47] the theory of interfacial ET has been applied by our group to describe factors influencing electron injection by a variety of means, including the nature of the accepting semiconductor, electronic coupling between donor and acceptor and reaction driving force.[6,7,48-50] The research presented in this work continues to focus on these investigations, exploring the dynamics of interfacial ET between various series of organic dyes to semiconductor nanoporous thin films. The dynamics of ET from these dyes and factors influencing ET rate will be discussed in chapters 4, 5 and 6, respectively.

1.2. Electron Transfer from Dyes to Nanoporous Semiconductor Films

1.2.1. Measurement of Interfacial Electron Transfer

Early studies of electron transfer focused mainly on systems where ET is the rate-limiting step, i.e. electrochemical cells where steady-state current/voltage measurements were on the timescale of nanoseconds or longer due to electrolyte and carrier transport.[7,41,44,51-57] Sub-nanosecond measurements of ET processes have been reported, utilizing such methods as time-resolved fluorescence spectroscopy.[41,58,59] In our group's measurements, we have used time-correlated single-photon counting to monitor electron transfer from adsorbate to semiconductor by comparing the fluorescence decay of the adsorbate on both injecting and noninjecting surfaces.[60,61] In instances where ET occurs, excited population of adsorbate is quenched, resulting in both a decreased yield and radiative lifetime τ_{ET} which can be quantified as in Equation 1.1

$$\tau_{ET} = \frac{1}{k_r + k_{nr} + k_{ET}} \tag{1.3}$$

where k_r, k_{nr} and k_{ET} are the rates for radiative, nonradiative and electron transfer processes, respectively. However, fluorescence quenching is capable of arising from factors unassociated with ET such as intermolecular energy transfer, making direct assignment of ET from fluorescence decay ambiguous.

In order to study ET dynamics on the femtosecond timescale, we employ transient pump-probe techniques in both the mid-infrared and visible regions. Because of the large effective surface area of the nanoporous films in our experiments, the adsorbate-semiconductor interface can be directly probed during the ET process, providing a level of detail regarding ultrafast dynamics only recently available given advances in ultrafast laser technology. The dynamics observed depend on the spectral region being probed, where species relevant to ET are individually assignable and can be attributed to both the semiconductor and adsorbate. It has been observed that both conduction band electrons and valence band holes in semiconductors exhibit strong absorbances in the mid-infrared region.[6-9,11,24,34,48,50,62-85] This IR absorbance is believed to originate as a result of free carrier absorption, intra-band transitions and trap absorption due to defect states in the semiconductors.[86] Upon photoexcitation of the adsorbate, the ET process is then directly observable in the mid-IR region, providing an unambiguous probe demonstrating arrival of injected electron to semiconductor conduction band.[6-9,11,24,34,48,50,62-76] Over time, relaxation of the electron through conduction band states can result in a decrease in absorption signal due to cross-section decay, making assignment of the observed signal with either relaxation or adsorbate recombination nontrivial.[71,87,88]

The use of transient visible pump-probe spectroscopy provides the necessary information to correlate adsorbate dynamics with those of injected electrons. The nanoporous films examined in this work utilize adsorbates that absorb light in the visible region of the spectrum, where electronic transitions relating to the intermediate species during ET can be observed.[14,17,18,25,30,32,48,71,89-114] These species include adsorbate ground, excited and oxidized states, which can be monitored over time and provide insight into charge transfer events if there is sufficient separation between spectral bands.[14,17,18,25,30,32,89-93,100-114] By combining the previously mentioned techniques, it is possible to show a direct relationship between the dynamics of electron injection as measured by ultrafast mid-IR absorption, and the transient donor species and intermediates measured by ultrafast visible measurements.[88,115]

1.2.2. Dependence of ET on Accepting Semiconductor

As mentioned previously, many semiconductors such as TiO_2,[6,11,13-23,69,72] SnO_2,[36,40] ZnO[36-38] and In_2O_3[36,37] have been studied as electron acceptors in DSSCs. However, ET dynamics to the latter substrates remain poorly understood due to the focus on TiO_2 as the most appealing semiconductor for commercial applications. As a result, injection dynamics to these substrates are not understood as fully as to TiO_2, often with differing results reported in the literature.[7,9,21,112,116,117] It has been theorized that the electronic structure of the different semiconductor conduction bands is a major contributor to variation in injection rate regardless of band-edge injection potential.[7,34,62] The conduction band of TiO_2 is composed mainly of empty d orbitals of Ti^{4+}, while the conduction bands of SnO_2, In_2O_3 and ZnO consist of empty s and p orbitals of Sn^{4+}, In^{3+} and Zn^{2+} respectively, with s-type character dominating.[118] The TiO_2 d-band character is thought to allow for greater electronic coupling between the accepting conduction band states and the injecting states of the donor molecules. In order to test this hypothesis, ET dynamics from a variety of organic sensitizers to TiO, SnO_2, and ZnO films have been systematically investigated, and will be presented in Chapters 4 and 5. ET dynamics from Fluorescein 548 to SnO_2, In_2O_3 and ZnO are presented in Chapter 6. We find that the injection rates for the four semiconductors follow the trend of $TiO2>>SnO_2\sim In_2O_3>>ZnO$.

1.3. Investigation of Molecular Orientation

The spectroscopy of interfaces has until only recently been a relatively elusive task, owing in part to the low number density of molecules compared to a bulk measurement, and the uncertainty as to whether or not detected signal is resulting from the interface itself or the associated bulk phase.[119-121] Recently, the development of a nondestructive, highly surface-specific probe technique known as Sum Frequency Vibrational Spectroscopy (SFVS) has sparked considerable interest in the properties of interfaces and the structures associated with interfacial processes.[122-127] This technique takes advantage of the forbidden nature of nonlinear photon generation from isotropic media, where the bulk phase produces negligible contributions to the observed signal while the non-centrosymmetric interface, where the symmetry of the bulk phase is broken, generates a coherent response that contains information about interfacial structure.[122,128] Due to its nonlinear nature, there are several requirements for SFVS to be utilized, in that high peak intensity electric fields are required for sufficient signal generation, and there should be little to no material loss from absorption in any of the bulk phases for the incident light before reaching the interface. The technique is straightforward in nature, involving temporally and spatially overlapping two coherent electric fields at an interface and taking advantage of the nonlinear nature of the interface to generate a third coherent field at the sum of the two incident field frequencies. When the fields are resonant with a molecular vibration or electronic transition, the generated signal is enhanced, providing information about the molecule at the interface. Typically one of the two fields is fixed in frequency in the visible range, while the other is tunable in the infrared for vibrational spectroscopy, allowing a broad range of detection of SF photons in the visible region.

As a coherent process, SFVS contains considerable information about the orientations of the interfacial molecules. The generated SF photons have an amplitude, polarization and phase associated with the SF active molecular vibrations, specifically associated with the transition moment orientations of the vibrations with respect to the polarizations of the incident electric fields.[126,127,129] Analysis of the generated signal using these parameters provides information regarding the characteristics of the active vibrations that aid in analyzing the average molecular orientation at the interface. Considerable work has already been done regarding deducing molecular orientations at the liquid/liquid,[130,131] liquid/vapor,[123,132] and solid/vapor[133,134] interfaces. Molecules examined at interfaces range from water, where interfacial structure has been shown to depend on the polarity of the adjacent phase, to alkyl chains and gas phase molecules,[135] where adsorption dynamics and conformation plays a major role in surface modification and catalysis.

A system of particular interest to our group is the dye-sensitized solar cell. In this system, a dye is adsorbed to the surface of semiconductor nanoparticles, where photoexcitation of the dye promotes an electron to a higher electronic state of the dye, and in the presence of sufficient driving force the electron is transferred to the semiconductor conduction band. The rate of electron transfer has been described using Marcus theory, where one of the factors in determining rate is the matrix element describing coupling between donor and acceptor electronic states.[136-139] This coupling is correlated with the orientation of the adsorbate upon the surface as it anchors to the semiconductor. Using transient infrared pump-probe absorption spectroscopy, our group has investigated electron-transfer kinetics of many dye-semiconductor systems. In the course of these investigations, it has become of particular interest to determine the molecular orientation of these adsorbed dyes in order to gain a more quantitative picture of the overall electron transfer process. Chapter 7 of this work presents the initial results of a SFVS study on several Re dyes previously investigated in transient measurements as a precursor to full determination of molecular orientation.

1.4. Summary

In summary, by using femtosecond infrared and visible transient absorption spectroscopies, the interfacial electron transfer dynamics of organic dye-semiconductor nanoparticle composites have been systematically investigated. The dependence of ET rate on accepting semiconductor has been studied for coumarin 343. Additionally, the dependence of ET rate on both Fluorescein 548 and a series of oligoene dyes with varying spacer chain length was studied with regards to accepting semiconductor. Finally, the nonlinear vibrational spectra of several Re polypyridyl dyes on both Au and TiO_2 nanocrystalline films was investigated as a first-principles step towards exploring ET-related conformational dynamics.

The rest of this work will be organized as follows: Chapter 2 introduces the basic theoretical descriptions of interfacial electron transfer and sum frequency vibrational spectroscopy. Chapter 3 summarizes the sample preparations and experimental techniques. Chapter 4 explores the dependence of interfacial ET rate from C343 to various semiconductors. Chapter 5 examines the effect of varying redox potentials with oligoene dyes on differing semiconductor films. Chapter 6 correlates mid-IR and visible spectroscopic results of Fluorescein 548 ET dynamics on various semiconductors. Chapter 7 demonstrates the feasibility of nonlinear vibrational spectroscopy applied to previously examined transition-metal dyes.

References:

(1) O'Regan, B.; Gratzel, M. *Nature* **1991**, *353*, 737.

(2) Bach, U.; Lupo, D.; Comte, P.; Moser, J. E.; Weissortel, F.; Salbeck, J.; Spreitzer, H.; Gratzel, M. *Nature* **1998**, *395*, 583.

(3) Gratzel, M. Mesoporous oxide junctions and nanostructured solar cells. In *Curr. Opin. Colloid Interface Sci.*, 1999; Vol. 4; pp 314.

(4) Brabec, C. J. *Sol. Energy Mater. Sol. Cells* **2004**, *83*, 273.

(5) Nazeeruddin, M. K.; Kay, A.; Rodicio, I.; Humphrybaker, R.; Muller, E.; Liska, P.; Vlachopoulos, N.; Gratzel, M. *J. Am. Chem. Soc.* **1993**, *115*, 6382.

(6) Asbury, J. B.; Anderson, N. A.; Hao, E.; Lian, T. *J. Phys. Chem. B* **2003**, *107*, 7376.

(7) Asbury, J. B.; Hao, E.; Wang, Y.; Ghosh, H. N.; Lian, T. *J. Phys. Chem. B* **2001**, *105*, 4545.

(8) Asbury, J. B.; Wang, Y. Q.; Hao, E. C.; Ghosh, H. N.; Lian, T. *Res. Chem. Interm.* **2001**, *27*, 393.

(9) Asbury, J. B.; Wang, Y.; Lian, T. *J. Phys. Chem. B* **1999**, *103*, 6643.

(10) Ellingson, R. J.; Asbury, J. B.; Ferrere, S.; Ghosh, H. N.; Sprague, J. R.; Lian, T.; Nozik, A. J. *Z. Phys. Chem. (Muenchen)* **1999**, *212*, 77.

(11) Ellingson, R. J.; Asbury, J. B.; Ferrere, S.; Ghosh, H. N.; Sprague, J. R.; Lian, T.; Nozik, A. J. *J. Phys. Chem. B* **1998**, *102*, 6455.

(12) Tachibana, Y.; Haque, S. A.; Mercer, I. P.; Durrant, J. R.; Klug, D. R. *J. Phys. Chem. B* **2000**, *104*, 1198.

(13) Tachibana, Y.; Haque, S. A.; Mercer, I. P.; Moser, J. E.; Klug, D. R.; Durrant, J. R. *J. Phys. Chem. B* **2001**, *105*, 7424.

(14) Tachibana, Y.; Nazeeruddin, M. K.; Gratzel, M.; Klug, D. R.; Durrant, J. R. *Chemical Physics* **2002**, *285*, 127.

(15) Durrant, J. R.; Tachibana, Y.; Mercer, I.; Moser, J. E.; Gratzel, M.; Klug, D. R. *Z. Phys. Chem.* **1999**, *212*, 93.

(16) Tachibana, Y.; Moser, J. E.; Graetzel, M.; Klug, D. R.; Durrant, J. R. *J. Phys. Chem.* **1996**, *100*, 20056.

(17) Kuciauskas, D.; Monat, J. E.; Villahermosa, R.; Gray, H. B.; Lewis, N. S.; McCusker, J. K. *J. Phys. Chem. B* **2002**, *106*, 9347.

(18) Hannappel, T.; Burfeindt, B.; Storck, W.; Willig, F. *J. Phys. Chem. B* **1997**, *101*, 6799.

(19) Kallioinen, J.; Benko, G.; Myllyperkio, P.; Khriachtechev, L.; Skarman, B.; Wallenberg, R.; Tuomikoski, M.; Korppi-Tommola, J. E. I.; Sundstrom, V.; Yartsev, A. P. *Journal of Physical Chemistry B* **2004**, *108*, 6365.

(20) Benko, G.; Kallioinen, J.; Myllyperkio, P.; Trif, F.; Korppi-Tommola, J. E. I.; Yartsev, A. P.; Sundstrom, V. *Journal of Physical Chemistry B* **2004**, *108*, 2862.

(21) Benko, G.; Myllyperkio, P.; Pan, J.; Yartsev, A. P.; Sundstrom, V. *J. Am. Chem. Soc* **2003**, *125*, 1118.

(22) Kallioinen, J.; Benko, G.; Sundstrom, V.; Korppi-Tommola, J. E. I.; Yartsev, A. P. *J. Phys. Chem. B* **2002**, *106*, 4396.

(23) Benko, G.; Kallioinen, J.; Korppi-Tommola, J. E. I.; Yartsev, A. P.; Sundstrom, V. *J. Am. Chem. Soc.* **2002**, *124*, 489.

(24) Heimer, T. A.; Heilweil, E. J.; Bignozzi, C. A.; Meyer, G. J. *J. Phys. Chem. A* **2000**, *104*, 4256.

(25) Kamat, P. V.; Bedja, I.; Hotchandani, S.; Patterson, L. K. *Journal Of Physical Chemistry* **1996**, *100*, 4900.

(26) Haque, S. A.; Tachibana, Y.; Willis, R. L.; Moser, J. E.; Graetzel, M.; Klug, D. R.; Durrant, J. R. *J. Phys. Chem. B* **2000**, *104,* 538.

(27) Palomares, E.; Clifford, J. N.; Haque, S. A.; Lutz, T.; Durrant, J. R. *Journal of the American Chemical Society* **2003**, *125*, 475.

(28) Barzykin, A. V.; Tachiya, M. *Journal of Physical Chemistry B* **2004**, *108*, 8385.

(29) Barzykin, A. V.; Tachiya, M. *J. Phys. Chem. B* **2002**, *106*, 4356.

(30) Hasselmann, G. M.; Meyer, G. J. *J. Phys. Chem. B* **1999**, *103*, 7671.

(31) Nelson, J. *Phys. Rev. B: Condens. Matter Mater. Phys.* **1999**, *59*, 15374.

(32) Nelson, J.; Haque, S. A.; Klug, D. R.; Durrant, J. R. *Phys. Rev. B: Condens. Matter Mater. Phys.* **2001**, *63,* 205321.

(33) Ai, X.; Anderson, N. A.; Guo, J.; Lian, T. *J. Phys. Chem. B* **2005**, *109*, 7088.

(34) Anderson, N. A.; Ai, X.; Lian, T. *J. Phys, Chem. B* **2003**, *107,* 14414.

(35) Stergiopoulos, T.; Arabatzis, I. M.; Cachet, H.; Falaras, P. *Journal of Photochemistry and Photobiology, A: Chemistry* **2003**, *155*, 163.

(36) Hara, K.; Horiguchi, T.; Kinoshita, T.; Sayama, K.; Sugihara, H.; Arakawa, H. *Solar Energy Materials and Solar Cells* **2000**, *64*, 115.

(37) Sayama, K.; Sugihara, H.; Arakawa, H. *Chem. Mater.* **1998**, *10*, 3825.

(38) Rensmo, H.; Keis, K.; Lindstrom, H.; Sodergren, S.; Solbrand, A.; Hagfeldt, A.; Lindquist, S. E.; Wang, L. N.; Muhammed, M. *Journal of Physical Chemistry* **1997**, *101*, 2598.

(39) Bedja, I.; Hotchandani, S.; Kamat, P. V. *J. Phys. Chem.* **1994**, *98*, 4133.

(40) Ferrere, S.; Zaban, A.; Gregg, B. A. *Journal of Physical Chemistry B* **1997**, *101*, 4490.

(41) Miller, R. J. D.; McLendon, G. L.; Nozik, A. J.; Schmickler, W.; Willig, F. *Surface electron transfer processes*; VCH publishers, Inc.: New York, 1995.

(42) Kamat, P. V. *Chemical Reviews* **1993**, *93*, 267.

(43) Kamat, P. V. *Progress In Reaction Kinetics* **1994**, *19*, 277.

(44) Hagfeldt, A.; Gratzel, M. *Chem. Rev.* **1995**, *95*, 49.

(45) Barbara, P. F.; Meyer, T. J.; Ratner, M. A. *J. Phys. Chem.* **1996**, *100*, 13148.

(46) Marcus, R. A.; Sutin, N. *Biochem. Biophys. Acta* **1985**, *811*, 265.

(47) Newton, M. D. *Chem. Rev.* **1991**, *91*, 767.

(48) Anderson, N. A.; Ai, X.; Chen, D.; Mohler, D. L.; Lian, T. *Journal of Physical Chemistry B* **2003**, *107*, 14231.

(49) Anderson, N. A.; Lian, T. *Annual Review of Physical Chemistry* **2005**, *56*, 491.

(50) Asbury, J. B.; Hao, E.; Wang, Y.; Lian, T. *J. Phys. Chem. B* **2000**, *104*, 11957.

(51) Nozik, A. J.; Memming, R. *Journal of Physical Chemistry* **1996**, *100*, 13061.

(52) Lewis, N. S. *Annual Review of Physical Chemistry* **1991**, *42*, 543.

(53) Memming, R. *Topics in Current Chemistry* **1994**, *169*, 105.

(54) Smalley, J. F.; Feldberg, S. W.; Chidsey, C. E. D.; Linford, M. R.; Newton, M. D.; Liu, Y. P. *Journal of Physical Chemistry* **1995**, *99*, 13141.

(55) Sachs, S. B.; Dudek, S. P.; Hsung, R. P.; Sita, L. R.; Smalley, J. F.; Newton, M. D.; Feldberg, S. W.; Chidsey, C. E. D. *Journal of the American Chemical Society* **1997**, *119*, 10563.

(56) Chidsey, C. E. D. *Science* **1991**, *251*, 919.

(57) Finklea, H. O.; Hanshew, D. D. *J. Am. Chem. Soc.* **1992**, *114*, 3173.

(58) Rehm, J. M.; McLendon, G. L.; Nagasawa, Y.; Yoshihara, K.; Moser, J.; Gratzel, M. *J. Phys. Chem.* **1996**, *100*, 9577.

(59) Willig, F.; Eichberger, R.; Sundaresan, N. S.; Parkinson, B. A. *Journal Of the American Chemical Society* **1990**, *112*, 2702.

(60) Jin, S.; Issac, A.; Stockwell, D.; Yin, F.-C.; Kindt, J.; Batista, V. S.; Robert, S.; Lian, T. **to be submitted**.

(61) Goh, W.; Guo, J.; Yuan, R.; Lian, T. “Single molecule study of Rhodamine/ATO nanoparticle junctions”; Proceedings of SPIE-The International Society for Optical Engineering, (Physical Chemistry of Interfaces and Nanomaterials IV), 2005.

(62) Anderson, N. A.; Lian, T. *Coord. Chem. Rev.* **2004**, *248*, 1231.

(63) Ai, X.; Anderson, N. A.; Asbury, J. B.; Hao, E.; Lian, T. *Proceedings of SPIE-The International Society for Optical Engineering* **2003**, *5223*, 147.

(64) Ai, X.; Guo, J.; Anderson, N. A.; Lian, T. *Journal of Physical Chemistry B* **2004**, *108*, 12795.

(65) Hao, E.; Anderson, N. A.; Asbury, J. B.; Lian, T. *J. Phys. Chem. B* **2002**, *106*, 10191.

(66) Anderson, N. A.; Hao, E.; Ai, X.; Hastings, G.; Lian, T. *Chem. Phys. Lett.* **2001**, *347*, 304.

(67) Wang, Y.; Asbury, J. B.; Lian, T. *J. Phys. Chem. A* **2000**, *104*, 4291.

(68) Ghosh, H. N.; Asbury, J. B.; Lian, T. *PINSA-A: Proc. Indian Natl. Sci. Acad., Part A* **2000**, *66*, 177.

(69) Asbury, J. B.; Ellingson, R. J.; Ghosh, H. N.; Ferrere, S.; Nozik, A. J.; Lian, T. *J. Phys. Chem. B* **1999**, *103*, 3110.

(70) Ghosh, H. N.; Asbury, J. B.; Lian, T. *J. Phys. Chem. B* **1998**, *102*, 6482.

(71) Ghosh, H. N.; Asbury, J. B.; Weng, Y.; Lian, T. *J. Phys. Chem. B* **1998**, *102*, 10208.

(72) Heimer, T. A.; Heilweil, E. J. *J. Phys. Chem. B* **1997**, *101*, 10990.

(73) Ai, X.; Anderson, N. A.; Guo, J.; Lian, T. *Journal of Physical Chemistry B* **2005**, *109*, 7088.

(74) Guo, J.; She, C.; Lian, T. *Journal of Physical Chemistry B* **2005**, *109*, 7095.

(75) Guo, J.; Stockwell, D.; Ai, X.; She, C.; Anderson, N. A.; Lian, T. *Journal of Physical Chemistry B* **2006**, *110*, 5238.

(76) She, C.; Anderson, N. A.; Guo, J.; Liu, F.; Goh, W.-H.; Chen, D.-T.; Mohler, D. L.; Tian, Z.-Q.; Hupp, J. T.; Lian, T. *Journal of Physical Chemistry B* **2005**, *109*, 19345.

(77) Guyot-Sionnest, P.; Hines, M. A. *Applied Physics Letters* **1998**, *72*, 686.

(78) Guyot-Sionnest, P.; Shim, M.; Matranga, C.; Hines, M. *Physical Review B-Condensed Matter* **1999**, *60*, R2181.

(79) Shim, M.; Guyot-Sionnest, P. *Nature* **2000**, *407*, 981.

(80) Shim, M.; Guyot-Sionnest, P. *Physical Review B: Condensed Matter and Materials Physics* **2001**, *64*, 245342/1.

(81) Wang, C.; Shim, M.; Guyot-Sionnest, P. *Science* **2001**, *291*, 2390.

(82) Wang, C.; Shim, M.; Guyot-Sionnest, P. *Appl. Phys. Lett.* **2002**, *80*, 4.

(83) Wang, C.; Wehrenberg, B. L.; Woo, C. Y.; Guyot-Sionnest, P. *Journal of Physical Chemistry B* **2004**, *108*, 9027.

(84) Klimov, V. I.; McBranch, D. W.; Leatherdale, C. A.; Bawendi, M. G. *Physical Review B-Condensed Matter* **1999**, *60*, 13740.

(85) Klimov, V. I.; Mikhailovsky, A. A.; McBranch, D. W.; Leatherdale, C. A.; Bawendi, M. G. *Physical Review B: Condensed Matter and Materials Physics* **2000**, *61*, R13349.

(86) Pankove, J. I. *Optical Processes in Semiconductors*; Dover: New York, 1975.

(87) Weng, Y.-X.; Wang, Y.-Q.; Asbury, J. B.; Ghosh, H. N.; Lian, T. *J. Phys. Chem. B* **2000**, *104*, 93.

(88) Huang, J.; Stockwell, D.; Boulesbaa, A.; Guo, J.; Lian, T. *J. Phys. Chem. C* **2008**, *112*, 5203.

(89) Piotrowiak, P.; Galoppini, E.; Wei, Q.; Meyer, G. J.; Wiewior, P. *J. Am. Chem. Soc.* **2003**, *125*, 5278.

(90) Hoertz, P. G.; Carlisle, R. A.; Meyer, G. J.; Wang, D.; Piotrowiak, P.; Galoppini, E. *Nano Letters* **2003**, *3*, 325.

(91) Galoppini, E.; Guo, W.; Zhang, W.; Hoertz, P. G.; Qu, P.; Meyer, G. J. *J. Am. Chem. Soc.* **2002**, *124*, 7801.

(92) Qu, P.; Thompson, D. W.; Meyer, G. J. *Langmuir* **2000**, *16*, 4662.

(93) Furube, A.; Katoh, R.; Hara, K.; Murata, S.; Arakawa, H.; Tachiya, M. *J. Phys. Chem. B* **2003**, *107*, 4162.

(94) Furube, A.; Murai, M.; Watanabe, S.; Hara, K.; Katoh, R.; Tachiya, M. *J. Photochem. Photobiol., A* **2006**, *182*, 273.

(95) Hilgendorff, M.; Sundstroem, V. *J. Phys. Chem. B* **1998**, *102*, 10505.

(96) Huang, J.; Stockwell, D.; Boulesbaa, A.; Guo, J.; Lian, T. *J. Phys. Chem. C* **2008**, *112*, 5203.

(97) Anderson, N. A.; Hao, E.; Ai, X.; Hastings, G.; Lian, T. *Physica E: Low-Dimensional Systems & Nanostructures (Amsterdam, Netherlands)* **2002**, *14*, 215.

(98) Kitamura, T.; Ikeda, M.; Shigaki, K.; Inoue, T.; Anderson, N. A.; Ai, X.; Lian, T.; Yanagida, S. *Chemistry of Materials* **2004**, *16*, 1806.

(99) Szarko, J. M.; Neubauer, A.; Bartelt, A.; Socaciu-Siebert, L.; Birkner, F.; Schwarzburg, K.; Hannappel, T.; Eichberger, R. *J. Phys. Chem. C* **2008**, *112*, 10542.

(100) Haque, S. A.; Tachibana, Y.; Klug, D. R.; Durrant, J. R. *J. Phys. Chem. B* **1998**, *102*, 1745.

(101) Zimmermann, C.; Willig, F.; Ramakrishna, S.; Burfeindt, B.; Pettinger, B.; Eichberger, R.; Storck, W. *Journal of Physical Chemistry B* **2001**, *105*, 9245.

(102) Ramakrishna, S.; Willig, F.; May, V. *Chemical Physics Letters* **2002**, *351*, 242.

(103) Kalloinen, J.; Benko, G.; Sundstrom, V.; Korppi-Tommola, J. E. I.; Yartsev, A. P. *J. Phys. Chem. B* **2002**, *106*, 4396.

(104) Martini, I.; Hodak, J. H.; Hartland, G. V. *J. Phys. Chem. B* **1999**, *103*, 9104.

(105) Butoi, C. I.; Langdon, B. T.; Kelley, D. F. *J. Phys. Chem. B* **1998**, *102*, 9635.

(106) Chikan, V.; Waterland, M. R.; Huang, J. M.; Kelley, D. F. *J. Chem. Phys.* **2000**, *113*, 5448.

(107) Olsen, C. M.; Waterland, M. R.; Kelley, D. F. *J. Phys. Chem. B* **2002**, *106*, 6211.

(108) Cherepy, N. J.; Smestad, G. P.; Gratzel, M.; Zhang, J. Z. *J. Phys. Chem. B.* **1997**, *101*, 9342.

(109) Kilsa, K.; Mayo, E. I.; Kuciauskas, D.; Villahermosa, R.; Lewis, N. S.; Winkler, J. R.; Gray, H. B. *J. Phys. Chem. A* **2003**, *107*, 3379.

(110) Huber, R.; Sporlein, S.; Moser, J. E.; Gratzel, M.; Wachtveitl, J. *J. Phys. Chem. B* **2000**, *104*, 8995.

(111) Katoh, R.; Furube, A.; Hara, K.; Murata, S.; Sugihara, H.; Arakawa, H.; Tachiya, M. *J. Phys. Chem. B* **2002**, *106*, 12957.

(112) Iwai, S.; Hara, K.; Murata, S.; Katoh, R.; Sugihara, H.; Arakawa, H. *J. Chem. Phys.* **2000**, *113*, 3366.

(113) Gaal, D. A.; Hupp, J. T. *J. Am. Chem. Soc.* **2000**, *122*, 10956.

(114) Benkoe, G.; Kallioinen, J.; Myllyperkioe, P.; Trif, F.; Korppi-Tommola, J. E. I.; Yartsev, A. P.; Sundstroem, V. *Journal of Physical Chemistry B* **2004**, *108*, 2862.

(115) Boulesbaa, A.; Issac, A.; Stockwell, D.; Huang, Z.; Huang, J.; Guo, J.; Lian, T. *J. Am. Chem, Soc.* **2007**, *129*, 15132.

(116) Bauer, C.; Boschloo, G.; Mukhtar, E.; Hagfeldt, A. *J. Phys. Chem. B* **2001**, *105*, 5585.

(117) Bauer, C.; Boschloo, G.; Mukhtar, E.; Hagfeldt, A. *International Journal of Photoenergy* **2002**, *4*, 17.

(118) Henrich, V.; Cox, P. *The Surface Science of Metal Oxides*; Cambridge University Press: Cambridge, 1996.

(119) Somorjai, G. A. *Introduction to Surface Chemistry and Catalysis*; Wiley: New York, 1994.

(120) Woodruff, D.; Delchar, T. *Modern Techniques of Surface Science*; Cambridge Univ. Press: Cambridge, 1986.

(121) Zangwill, A. *Physics at Surfaces*; Cambridge Univ. Press: Cambridge, 1988.

(122) Richmond, G. L. *Chemical Reviews (Washington, DC, United States)* **2002**, *102*, 2693.

(123) Allen, H. C.; Raymond, E. A.; Richmond, G. L. *J. Phys. Chem. A* **2001**, *105*, 1649.

(124) Chen, Z.; Shen, Y. R.; Somorjai, G. A. *Ann. Rev. Phys. Chem* **2002**, *53*, 437.

(125) Wolfrum, K.; Lobau, J. *J. Opt. Soc. Am. B* **1997**, *14*, 2505.

(126) Buck, M.; Himmelhaus, M. *J. Vac. Sci. Tech. A* **2001**, *19*, 2717.

(127) McGilp, J. F. *J. Phys. D: Appl. Phys.* **1996**, *29*, 1812.

(128) Shen, Y. R. *The Principles of Nonlinear Optics*; Wiley: New York, 1984.

(129) Bain, C.; Davies, P.; Ong, T.; Ward, R. *Langmuir* **1991**, *7*, 1563.

(130) Shen, Y. R.; Miranda, P. B. *J. Phys. Chem. B* **1999**, *103*, 3292.

(131) Bain, C.; Knock, M.; Bell, G.; Hill, E.; Turner, H. *J. Phys. Chem. B* **2003**, *107*, 10801.

(132) Richmond, G. L. *Annu. Rev. Phys. Chem.* **2001**, *52*, 357.

(133) Bonn, M.; Hess, C.; Wolf, M. *J. Chem. Phys.* **2001**, *115*, 7725.

(134) Hess, C.; Wolf, M.; Roke, S.; Bonn, M. *Surface Science* **2002**, *502-503*, 304.

(135) Jayathilake, H.; Zho, M.; Rosenblatt, C.; Bordenyuk, A.; Weeraman, C.; Benderskii, A. *J. Chem. Phys.* **2006**, *125*, 64706.

(136) Marcus, R. A. *J. Chem. Phys.* **1965**, *43*, 679.

(137) Gao, Y. Q.; Georgievskii, Y.; Marcus, R. A. *J. Chem. Phys.* **2000**, *112*, 3358.

(138) Gao, Y. Q.; Marcus, R. A. *J. Chem. Phys.* **2000**, *113*, 6351.

(139) Gosavi, S.; Marcus, R. A. *J. Phys. Chem. B* **2000**, *104*, 2067.

Chapter 2. Theoretical Considerations

This chapter presents a basic theoretical description of interfacial electron transfer between a molecular adsorbate and semiconductor nanocrystals, as well as the theoretical principles behind the application of sum frequency vibrational spectroscopy. It will begin with a classical treatment of electron transfer between a donor and acceptor, and continue by describing the interfacial electron transfer process involved between a photoexcited adsorbate and the manifold of semiconductor accepting states. Finally, it will conclude with the theory of nonlinear surface vibrational spectroscopy.

2.1 Theory of Interfacial Electron Transfer

2.1.1. Electron transfer from donor to acceptor

In the simplest treatment of electron transfer, we consider a two state model composed of a reactant state D^*A and a product state D^+A^-. The reactant state can be described as a photoexcited donor molecule coupled to the electron acceptor, and the product state described as the oxidized donor and reduced acceptor after the electron transfer process, which is expressed as:

$$D^*A \xrightarrow{k_{ET}} D^+A^- \tag{2.1}$$

The rate of electron transfer k_{ET} in Equation 2.1 can be defined by standard transition state theory as[1-3]

$$k_{ET} = k_e \upsilon_n \exp(-\Delta G^{\neq} / RT) \tag{2.2}$$

in which $\Delta G^{\neq}$ is the free energy of activation for the electron transfer process, and ν_n is the frequency of nuclear motion corresponding to the reaction coordinate as shown below in Figure 2.1.[1-7] The k_e electronic transmission factor in Equation 2.2 is governed by the degree of electronic coupling between the reactant and product states, and will be treated as unity until its considerations are addressed later in this section.

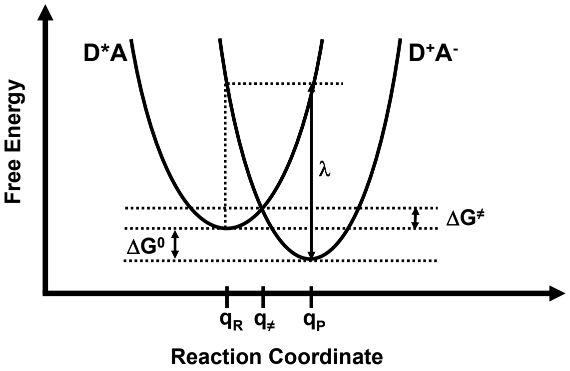

Figure 2.1. Diagram of the potential surfaces involved in the electron transfer process between reactants D^*A and products D^+A^- as a function of reaction coordinate in the Marcus normal region where $\Delta G^0 < \lambda$. ΔG^0 is the free energy difference between equilibrium configurations of D^*A and D^+A^-, λ is the reorganization energy associated with changing equilibrium coordinates from product to reactant configurations, and $\Delta G^{\neq}$ is the free energy of activation.

In Figure 2.1, the two potential wells corresponding to the reaction coordinates q of reactant and product states are approximated by parabolic surfaces, where Equations 2.3 and 2.4

$$V_R = \frac{1}{2} f_R (q - q_R)^2 + G_R \tag{2.3}$$

$$V_P = \frac{1}{2} f_P (q - q_P)^2 + G_P \tag{2.4}$$

define the free energy of the reactant and product surfaces with respect to the nuclear coordinates and their associated equilibrium coordinates q_R and q_P, as well as the equilibrium free energies G_R and G_P. Typically, we can simplify the derivation by making the assumption that the force constants associated with the product and reactant potential surfaces are equal. If, using this notation, we wish to obtain the activation free energy $\Delta G^{\neq}$, we can substitute the activation energy nuclear coordinate $q_{\neq}$ and associated free energy $V_{\neq}$ into Equation 2.3, obtaining

$$V_{\neq} = \frac{1}{2} f\left(q_{\neq} - q_R\right)^2 + G_R \tag{2.5}$$

which upon substitution of $\Delta G^{\neq} = V_{\neq} - V_R$ leads to

$$\Delta G^{\neq} = \frac{1}{2} f\left(q_{\neq} - q_R\right)^2 \tag{2.6}$$

We define the reorganization energy λ as the free energy change that occurs when the system crosses the barrier separating reactant from product states given the product nuclear coordinates, which under the parabolic approximation of Equation 2.4 results in

$$\lambda = \frac{1}{2} f\left(q_R - q_P\right)^2 \tag{2.7}$$

In order to obtain an expression for the nuclear coordinate $q^{\neq}$ corresponding to the crossing point of the two potential surfaces $V_R(q^{\neq})$ and $V_P(q^{\neq})$, we can use Equations 2.3 and 2.4 as an equality, rearranging accordingly to represent $q^{\neq}$ as

$$q^{\neq} = \frac{1}{f} \frac{\Delta G^0}{(q_P - q_R)} + \frac{1}{2}(q_P + q_R) \tag{2.8}$$

which can be substituted into Equation 2.6, yielding the expression

$$\Delta G^{\neq} = \frac{1}{2f}\frac{(\Delta G^{0})^{2}}{(q_{P}-q_{R})^{2}} + \Delta G^{0} + \frac{f}{8}(q_{P}-q_{R})^{2} \tag{2.9}$$

Rearrangement of Equation 2.9 results in

$$\Delta G^{\neq} = \frac{\left(\Delta G^{0} + \frac{1}{2}f(q_{R}-q_{P})^{2}\right)^{2}}{2f(q_{R}-q_{P})^{2}} \tag{2.10}$$

and using Equation 2.7 as a substitution we obtain the familiar equation[6] showing the relation of the free energy of activation $\Delta G^{\neq}$ with the total free energy change of the electron transfer reaction ΔG^0 and reorganization energy λ:

$$\Delta G^{\neq} = \frac{\left(\Delta G^{0} + \lambda\right)^{2}}{4\lambda} \tag{2.11}$$

In this case, λ is defined as the total reorganization energy, which can be represented as the sum of two terms

$$\lambda = \lambda_{in} + \lambda_{out} \tag{2.12}$$

where λ_{in} is the inner-sphere reorganization energy originating from the changes in bond lengths and angles during the electron transfer process. λ_{in} is typically treated harmonically as represented in Equation 2.13:[7]

$$\lambda_{in} = \frac{1}{2}\sum_{i}\overline{f}_{i}(q_{R}^{eq} - q_{P}^{eq})^{2} \tag{2.13}$$

where q_R^{eq} and q_P^{eq} are the equilibrium nuclear coordinates in the reactant state $D^{*}A$ and the product state $D^{+}A^{-}$, respectively. $\overline{f}_i$ is the reduced force constant for the *i*-th bond vibration, which is summed over all significant intramolecular vibrations included in the donor-acceptor pair. The outer term, λ_{out}, corresponds to the outer-sphere reorganization energy associated with the rearrangement of the solvent shell surrounding the reactants. If the solvent is treated as a dielectric continuum, λ_{out} can then be expressed as in Equation 2.14:[4,7]

$$\lambda_{out} = \frac{(\Delta e)^2}{4\pi\varepsilon_0}\left[\frac{1}{2a_D} + \frac{1}{2a_A} - \frac{1}{r_{DA}}\right]\left[\frac{1}{\varepsilon_{op}} - \frac{1}{\varepsilon_s}\right] \tag{2.14}$$

where Δe is the charge transferred in the ET process; a_D and a_A are the radii of the donor and the acceptor, respectively; r_{DA} is the center-to-center distance between the donor and the acceptor; ε_0 is the permittivity of vacuum; and ε_{op} and ε_s are the optical and static dielectric constants, respectively.

It is observed from Equation 2.11 that the transition free energy of activation depends both on the total reaction free energy and reorganization energy. According to this equation and Equation 2.2, the rate of electron transfer from donor to acceptor is maximized in the case where $\Delta G^0 = -\lambda$, and decreases as ΔG^0 increases further. The ramification of this observation is that as ΔG^0 continues to increase past what is known as the normal region ($\Delta G^0 = -\lambda$) and into the inverted region where $\Delta G^0 > -\lambda$, although the driving force for the electron transfer reaction is still increasing, the electron transfer rate is inhibited. This is especially important in the case of back-electron transfer as applied to DSSCs given a sufficiently high driving force from the semiconductor to the oxidized adsorbate, where a low probability of recombination is desired.

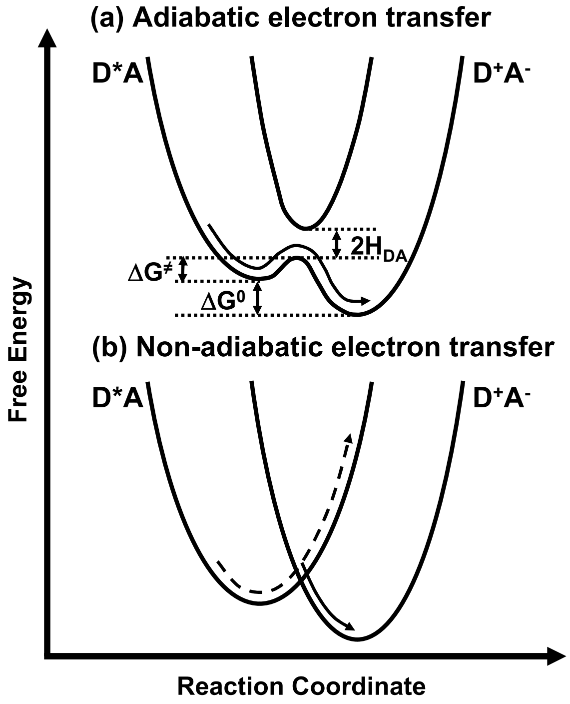

Figure 2.2. Diagram of the potential surfaces involved in the electron transfer process between reactants D^*A and products D^+A^- described using **a)** the adiabatic electron transfer mechanism and **b)** the non-adiabatic mechanism. In the adiabatic case, the potential surface coupling is shown to be indicative of a large perturbation, where the splitting of energy levels is on the order $2H_{DA}$.

As mentioned previously in describing Equation 2.2, the electronic transmission factor k_e is governed by the degree of electronic coupling between the reactant and product states, and is an additional factor in describing significant contributions to differences in electron transfer rate. The treatment described earlier in this section neglected the effects of k_e, instead focusing on the effects of reaction free and reorganization energies that influence ET rate; from this point on it becomes important to include k_e in describing the rate of electron transfer with respect to coupling between the donor and acceptor. In the previous case where it was assumed that k_e was unity in the treatment of Equation 2.2, it physically corresponded to an adiabatic process as shown in Figure 2.2a, where a strong electronic interaction between the reactants resulted in a k_e=1 value. More specifically, the electronic coupling between the donor and acceptor states in the electron transfer reaction can be represented by the electron exchange matrix element H_{DA}, which represents the strength of the coupling energy between the reactant and product states as

$$H_{DA} = \left\langle \psi_R^0 \middle| \overline{H} \middle| \psi_P^0 \right\rangle \tag{2.15}$$

where ψ_R^0 and ψ_P^0 represent the electronic wavefunctions of the reactant and product equilibrium states, and H is the electronic Hamiltonian for the system. For large coupling energy values $\left|H_{DA}\right|^2$, the large perturbation of energy levels causes separation of the intersection region where the transition state immediately proceeds to the product states on the lower potential surface, as shown in Figure 2.2a. As the electronic coupling $\left|H_{DA}\right|^2$ decreases, the potential surfaces of D^*A and D^+A^- perturb each other less, to a point where the surfaces do not significantly interact. In this case the electron transfer is considered non-adiabatic as shown in Figure 2.2b, and can be described using the general rate expression[2,8,9]

$$k_{ET} = \frac{2\pi}{\hbar} \frac{\left|H_{DA}\right|^2}{\sqrt{4\pi\lambda kT}} \exp[-\frac{(\Delta G^0 + \lambda)^2}{4\lambda kT}] \tag{2.16}$$

2.1.2. Interfacial electron transfer between adsorbate and semiconductor

The basic theoretical framework for describing interfacial ET was developed by Marcus,[6] Gerischer[10,11] and Levich and Dogonadeze[12] in the 1960's. In order to describe electron transfer from a molecular adsorbate to the accepting semiconductor, Equation 2.16 must be modified to take into account the fact that rather than a single product state as described in the previous section, the semiconductor conduction band consists of a manifold of states, each capable of participating in the electron transfer process as shown in Figure 2.3.

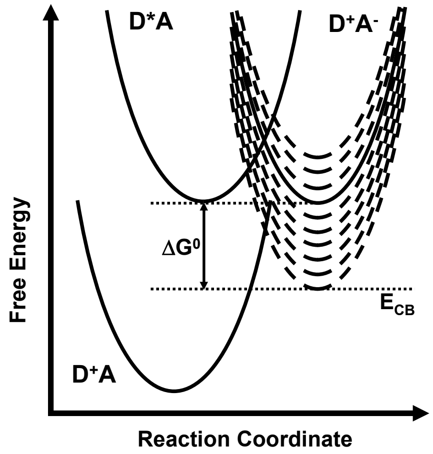

Figure 2.3. Potential energy surface for electron transfer (ET) from a reactant state D^*A to a continuous manifold of product states D^+A^-. In the nonadiabatic limit, the total ET rate is the sum of ET to all possible states, as shown in Equation 2.17.

In the nonadiabatic limit as described previously, the total electron transfer rate from the excited adsorbate to the accepting semiconductor can be expressed as the sum of all ET rates to the various states within the conduction band manifold, as based on Marcus' treatment modifying Equation 2.16 to describe all possible accepting semiconductor states[13-17]

$$k_{ET} = \frac{2\pi}{h}\int_{-\infty}^{\infty} dE\rho(E)\left|\overline{H_{DA}}(E)\right|^2 \frac{1}{\sqrt{4\pi\lambda k_B T}}\exp\left[-\frac{(\lambda+\Delta G_0 - E)^2}{4\lambda k_B T}\right] \qquad (2.17)$$

where $\rho(E)$: density of states at energy E; $\boldsymbol{H}_{DA}(E)$: the average electronic coupling matrix elements between the adsorbate excited state and accepting states in the semiconductor conduction band at energy E; λ: the reorganization energy; $\Delta G_0 = E_{cb} - E_{ox}$: the redox potential difference between the conduction band edge and the excited state of the adsorbed dye; k_B is the Boltzmann constant and T is temperature. A schematic representation of the dependence of Equation 2.17 on the semiconductor density of states with regards to λ and ΔG^0 is shown in Figure 2.4.

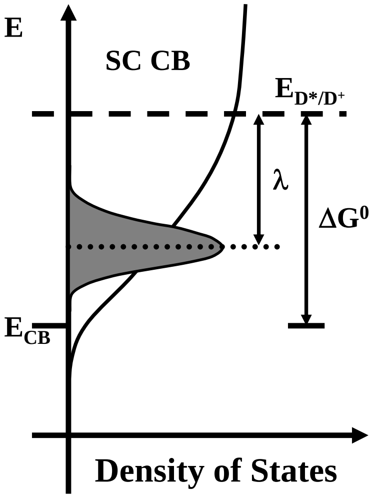

Figure 2.4. Schematic illustration of variation of the density of semiconductor states with energy E. The electron accepting states (grey area) are determined by the adsorbate excited state oxidation potential $E(D^*/D^+)$ and the reorganization energy λ.

According to Equation 2.17 and as shown in Figure 2.4, the electron transfer rate depends on the density of electron-accepting states in the semiconductor in addition to the adsorbate-SC coupling and reorganization energies.[6,13-15] If we assume that the conduction band contributes the majority of character to the electronic description of the accepting states, we can express the density of states in a defect-free semiconductor, i.e. bulk, as[18]

$$\rho_0(E)dE = \frac{(2m^*)^{3/2}}{2\pi^2\hbar^3}\sqrt{E}dE \qquad (2.18)$$

where $^*m_e$ is the effective mass of the electron in the conduction band. In the case of nanocrystalline semiconductors as used in the following studies, the high surface area introduced by the nanometer-size particles introduces significant effects when describing the density of states in terms of localized surface states not typical of the bulk semiconductor. These states typically have the greatest contribution to influencing the electron transfer process at or near the band edge, as shown in Figure 2.4, where the defect states are modeled as an exponential tail extending below the band edge.[19,20]

If we assume that the electronic coupling between donor and acceptor states is independent of energy, the electron transfer rate k_{ET} can be calculated as a function of $E(D^*/D^+)$-E_{CB} at different reorganization energies λ, as shown in Figure 2.5. For all reorganization energies with which k_{ET} is calculated, the injection rate increases when the donor excited state oxidation potential is further above the conduction band edge, and decreases as the driving force $E(D^*/D^+)$-E_{CB} approaches the conduction band edge. When the excited state is well above the conduction band edge, only small variation in injection rate can be observed. However, near the band edge, the change in rate is nearly exponential, indicating the more severe dependence of the ET rate on the variation of density of states.[21]

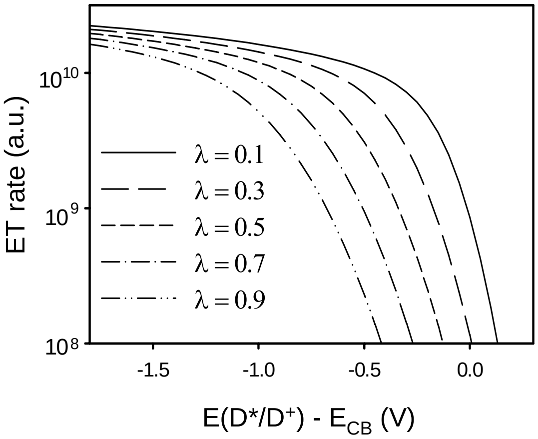

Figure 2.5. Calculated electron transfer rate to a semiconductor as a function of $E(D^*/D^+)$-E_{CB} under different reorganization energies.

2.2 Theory of Sum Frequency Vibrational Spectroscopy

The theory of SFVS is relatively straightforward, shown to be dependent on the nonlinear susceptibility of both the interface and the adsorbate. The technique uses two coherent electric fields overlapped at an interface to generate a third electric field equal to the sum of the two incident energies. At high peak electric field intensities that are comparable to the intramolecular field felt by an electron, the polarization generated in a medium requires that higher order effects be taken into consideration, where the total polarization is written as a series expansion of the incident electric field intensities E and the medium susceptibility $\chi^{(n)}$[22]

$$P = \chi^{(1)}E + \chi^{(2)}EE + \chi^{(3)}EEE + ... \tag{2.19}$$

where the linear and nonlinear properties of the medium are expressed by $\chi^{(n)}$. In the case of two incident electric fields at frequencies ω_1 and ω_2, the first nonlinear term results in polarizations oscillating at $2\omega_1$, $2\omega_2$, ω_1-ω_2, and ω_1+ω_2.[23] Physically this corresponds to second harmonic generation (SHG) of both visible and IR incident beams, difference frequency generation (DFG) at the difference of ω_{vis} and ω_{IR}, and sum frequency generation equal to the sum of ω_{vis} and ω_{IR}. The resultant second order polarization can then be expressed as

$$P^{(2)} = \chi^{(2)} E_{vis} E_{IR} \tag{2.20}$$

The surface selectivity of SFVS arises from the conditions necessary for a second-order polarization to be generated. In a medium where a center of symmetry exists, inversion operation reverses the sign of $P^{(2)}$, E_{vis} and E_{IR}, changing Equation 2.20 to

$$-P^{(2)} = \chi^{(2)} (-E_{vis})(-E_{IR}) \tag{2.21}$$

In order for both Equations 2.20 and 2.21 to be physically valid, the only solution is for $\chi^{(2)} = -\chi^{(2)} = 0$. This implies that in centrosymmetric media, i.e. bulk, the generation of second-order nonlinear terms is characteristically forbidden. At the interface of a medium, however, the inversion symmetry present in bulk is physically broken and inversion of $\chi^{(2)}$ is not necessarily zero, allowing for generation of SF photons from the interface itself with no contribution from bulk material. The intensity of the generated SF signal is shown in Equation 2.22 to be dependent on both the intensity of the incident visible (I_{vis}) and infrared (I_{IR}) fields, as well as the square of the macroscopic susceptibility as described in Equation 2.23 as the sum of a nonresonant contribution due to material response $\chi^{(2)}_{NR}$,[24] and the sum of all active vibrational resonances at frequency ν, $\chi^{(2)}_{\nu}$.

$$I_{SF} \propto \left|\chi^{(2)}\right|^2 I_{vis} I_{IR} \tag{2.22}$$

$$\left|\chi^{(2)}\right| = \left|\chi_{NR}^{(2)} + \sum_{\upsilon} \chi_{\upsilon}^{(2)}\right| \tag{2.23}$$

When the frequency of the infrared beam, $\omega_{IR,}$ is resonant with a vibrational mode ν, the resonant term in $\chi^{(2)}$ dominates the nonlinear susceptibility, and as a result the overall intensity of the SF signal is enhanced. The resonant part of the susceptibility can be further broken into components as described in Equations 2.24 and 2.25,

$$\chi_{\upsilon}^{(2)} \propto \frac{A_{\upsilon}}{\omega_{\upsilon} - \omega_{IR} - i\Gamma} \tag{2.24}$$

where A_ν represents the strength of the ν^{th} transition moment, ω_{υ} represents the frequency of the transition moment, and Γ represents the linewidth of the transition. The amplitude A_ν contains information regarding the molecular hyperpolarizability in lab-fixed coordinates from both the Raman and infrared transition moments[25]

$$A_{\upsilon} = \beta_{\upsilon,ijk} = \alpha_{\upsilon,ij}\,\mu_{\upsilon,k} \tag{2.25}$$

indicating that for a vibrational SF resonance to occur, the transition must be both Raman and infrared active as shown in Figure 2.6. From group theory, a molecule exhibiting a center of inversion can be either IR or Raman active, but not both, supporting the need for a non-centrosymmetric environment from which to observe SF signal. Boundaries between media, such as solid and vapor, are necessarily non-centrosymmetric due to the inherent discontinuity between the two layers, allowing a molecule sitting at the interface boundary to satisfy the requirements for both Raman and IR transition activity.

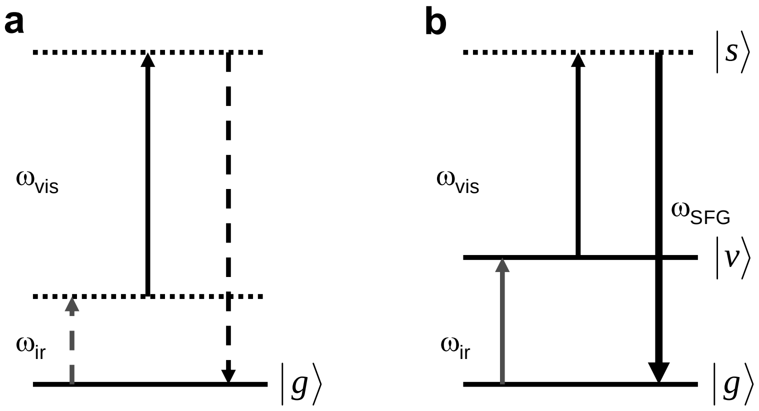

Figure 2.6. a) Off-resonance conditions for molecular SFG signal, where the mid-IR frequency ω_{ir} is not resonant with any transition ν. **b)** On-resonance condition for observation of molecular vibrational SFG signal, where ω_{ir} is resonant with vibrational transition g→ν, and upconverted by ω_{vis} to release photons at ω_{SFG}.

In the simplest representation of molecular symmetry at an interface, an adsorbate with $C_{\infty v}$ character is assumed to be isotropic about its rotation axis, where in the xyz plane defining molecular coordinates, only the z component of $\chi_{ijk}^{(2)}$ has a nonzero projection. Because $\chi_{ijk}^{(2)}$ is a third rank tensor containing 27 elements, this simplifies the description of $\chi_{ijk}^{(2)}$ assuming x and y are indistinguishable. The 4 components left from the 27 possible elements consist of $\chi_{zzz}^{(2)}$, $\chi_{zii}^{(2)}$, $\chi_{izi}^{(2)}$ and $\chi_{iiz}^{(2)}$, where *i* represents the interchangeable x or y and z represents surface normal in the laboratory-fixed frame of reference.[26] Different polarization combinations selectively probe these $\chi^{(2)}$ elements, which are either parallel or perpendicular to the laboratory-frame surface. In the reference frame given, the polarizations can be either S or P polarized, where S polarization corresponds to polarization perpendicular to the incident frame, and P polarization is polarized within the incident frame. The SSP polarization combination probes modes with IR transitions normal to the interfacial plane, while SPS and PSS combinations probe modes with IR transitions within the interfacial plane. The PPP polarization combination probes all components of the active vibrations within the IR pump pulse spectral range. Using these different polarization combinations in series, it is possible to obtain an intensity-dependent profile of the active tensor elements contributing to the SFG signal, which is determined by the molecular orientation at the interface.

References:

(1) Kavarnos, G. J. *Fundamentals of Photoinduced Electron Transfer*; VCH Publishers, Inc.: New York, New York, 1993.

(2) Marcus, R. A.; Sutin, N. *Biochem. Biophys. Acta* **1985**, *811*, 265.

(3) Newton, M. D. *Chem. Rev.* **1991**, *91*, 767.

(4) Marcus, R. A. *J. Chem. Phys.* **1956**, *24*, 966.

(5) Marcus, R. A.; Eyring, H. *Ann. Rev. Phys. Chem.* **1964**, *15*, 155.

(6) Marcus, R. A. *J. Chem. Phys.* **1965**, *43*, 679.

(7) Bolton, J. R.; Mataga, N.; McLendon, G.; Editors *Electron Transfer in Inorganic, Organic, and Biological Systems*, 1991.

(8) Gratzel, M. *Heterogeneous Photochemical Electron Transfer*; CRC Press: Boca Raton, Florida, 1988.

(9) Barbara, P. F.; Meyer, T. J.; Ratner, M. A. *J. Phys. Chem.* **1996**, *100*, 13148.

(10) Gerischer, H. *Z. Phys. Chem. Frankfurt* **1961**, *27*, 48.

(11) Gerischer, H. In *Physical Chemistry: An Advance Treatise*; Eyring, H., Henderson, D., Jost, W., Eds.; Academic Press: New York, 1970; Vol. IXA, p 463.

(12) Levich, V. G.; Dogonadze, R. R. *Dokl. Akad. Nauk SSSR* **1959**, *124*, 123.

(13) Gao, Y. Q.; Georgievskii, Y.; Marcus, R. A. *J. Chem. Phys.* **2000**, *112*, 3358.

(14) Gao, Y. Q.; Marcus, R. A. *J. Chem. Phys.* **2000**, *113*, 6351.

(15) Gosavi, S.; Marcus, R. A. *J. Phys. Chem. B* **2000**, *104*, 2067.

(16) Asbury, J. B.; Hao, E.; Wang, Y.; Ghosh, H. N.; Lian, T. *J. Phys. Chem. B* **2001**, *105*, 4545.

(17) Marcus, R. A. *J. Chem. Phys.* **2000**, *113*, 1618.

(18) Seeger, K. *Semiconductor Physics: an introduction*; Seventh ed.; Springer, 1999.

(19) Pankove, J. I. *Optical Processes in Semiconductors*; Dover: New York, 1975.

(20) Nelson, J.; Kirkpatrick, J.; Ravirajan, P. *Physical Review B: Condensed Matter and Materials Physics* **2004**, *69*, 035337/1.

(21) Anderson, N. A.; Lian, T. *Coord. Chem. Rev.* **2004**, *248*, 1231.

(22) Dick, B.; Gierulski, A.; Marowsky, G.; Reider, G. A. *Appl. Phys. B.* **1985**, *38*, 107.

(23) Shen, Y. R. *The Principles of Nonlinear Optics*; John Wiley&Sons, Inc., 1984.

(24) Sefler, G. A.; Du, Q.; Miranda, P. B.; Shen, Y. R. *Chem. Phys. Lett.* **1995**, *235*, 347.

(25) Hirose, C.; Akamatsu, N.; Domen, K. *J. Chem. Phys.* **1992**, *96*, 997.

(26) Richmond, G. L. *Chemical Reviews (Washington, DC, United States)* **2002**, *102*, 2693.

Chapter 3. Experimental Methods

The samples used in this work are based on metal oxide nanoporous films that have been sensitized by various molecular adsorbates. Preparation of semiconductor colloids used to create the nanoporous and nanocrystalline films is based on published procedures in the literature, but modified slightly to produce homogeneous and transparent films. Various preparation techniques for dye/semiconductor films have been studied in order to determine their effects on the rate of electron transfer. Electron transfer dynamics were obtained using ultrafast pump-probe transient absorption spectroscopies in the visible and mid-infrared regions, as well as with time-correlated single-photon counting fluorescence spectroscopy. Monolayer vibrational spectra were obtained using sum frequency vibrational spectroscopy. Semiconductor film morphology characterization for SFVS as determined by AFM is also included.

3.1. Preparation of Semiconductor Colloid and Nanoporous Films

3.1.1. Preparation of TiO_2 nanoporous thin films

TiO_2 nanoparticle thin films were prepared according to published procedures.[1,2] Briefly, the TiO_2 colloid was prepared by controlled hydrolysis of titanium (IV) isopropoxide in a mixture of glacial acetic acid and water at 0 ^{o}C. The resultant solution of particles was concentrated at 80 ^{o}C for several hours to concentrate, then autoclaved at 230 ^{o}C for 12 hours. The separated solid phase was mixed with several drops of TritonX-100 and stirred for 4 days to disperse the aggregated particles. Several drops of prepared TiO_2 colloid were placed on cleaned sapphire windows, and spread by a polished glass rod to form a homogeneous surface. The films were air-dried and sintered at 400 ^{o}C for 1.5 hours.

3.1.2. Preparation of SnO_2 nanoporous thin films

SnO_2 nanoparticle thin films were prepared from colloid synthesized according to a published procedure.[3] Briefly, $SnCl_4$ was carefully dissolved in HCl, and the resulting solution was added dropwise to water with vigorous stirring at 0 ^{o}C. The solution was pH adjusted to 3.5 with addition of aqueous ammonia, and allowed to sit overnight as nanoparticles precipitated. The precipitate was washed and suspended in water, after which the pH was adjusted to 9.5-10 and the solution dialyzed overnight to produce a colloidal solution of SnO_2. The solution was refluxed for 4 hours and autoclaved at 150 ^{o}C for 1 hour, then 270 ^{o}C for 16 hours. The colloid was concentrated and mixed with 15 drops of TritonX-100, then stirred for 1 day. Films were created by casting several drops onto cleaned sapphire windows and air-drying. Dried films were then baked at 400 ^{o}C for 1 hour.

3.1.3. Preparation of ZnO nanoporous thin films

ZnO colloid and thin films were prepared similar to previously published procedures.[4] Briefly, $Zn(Ac)_2$ was added to absolute ethanol and cooled to 0 ^{o}C. Then, $LiOH{\cdot}H_2O$ was dissolved in ethanol at room temperature, cooled to 0 ^{o}C and slowly added to the Zn(II) solution under vigorous stirring. The supernatant was removed by decantation or centrifugation, and the ZnO precipitate was resuspended in ethanol. The mixture was stored at 4 ^{o}C. Films were created by dropwise deposition on sapphire windows to the desired films thickness, then air-dried. The films were then baked for 1 hour at 400 ^oC.

3.1.4. Preparation of In_2O_3 nanoporous thin films

In_2O_3 nanoparticle colloids were synthesized according to published procedures.[5,6] Briefly, $InCl_3 \cdot 4H_2O$ was dissolved in deionized H_2O (Millipore, 18.3 MΩ/cm) at 0 ^oC under vigorous stirring. After stirring for 30 minutes, aqueous ammonia was added to adjust the pH to ~8, which led to the precipitation of indium hydroxide. The resulting precipitate was centrifuged and dried in vacuum for 10 minutes. The precipitate was mixed with water, 1 drop of 2,4-pentanedione and 10 drops of TritonX-100 and stirred for 2-3 days. The mixture was spread onto sapphire windows with a polished glass rod to form a homogeneous surface and baked at 400 ^oC for 1 hour.

3.1.5. Preparation of ZrO_2 nanoporous thin films

ZrO_2 nanoparticle films were prepared by using ZrO_2 nanoparticle powder obtained from Degussa Corporation. Briefly, 2 g ZrO_2 powder was mixed with 4 ml of water and stirred for 1 week. 10 drops of TritonX-100 was added to the solution, which was stirred overnight. Several drops of prepared ZrO_2 colloid were placed on cleaned sapphire windows, and spread by a polished glass rod to form a homogeneous surface. The films were air-dried and sintered at 400 ^oC for 1.5 hours.

3.2. Preparation and Characterization of Au and TiO_2 Nanocrystalline Films for Sum Frequency Vibrational Spectroscopy

3.2.1. Preparation of Au films

Sapphire windows were cleaned in piranha solution (H_2O_2 30%/H_2SO_4 mixture, 1:3) for 24 hours, then washed with DI water. Au films were then deposited on the cleaned windows and CaF_2 prisms (ISP Optics) using a Lesker PVD-75 Filament Evaporator. The deposition rate of the Au films was 5 angstroms per second at a pressure of $5x10^{-7}$ Torr for 200 seconds, resulting in a film thickness of ~100 nm as measured by a quartz microbalance. After deposition, the samples were stored in a sealed dry environment to prevent surface contamination. AFM characterization of the Au films, as shown in Figure 3.1, indicates average Au particle size of 25 nm, with a surface morphology roughness of ~10 nm.

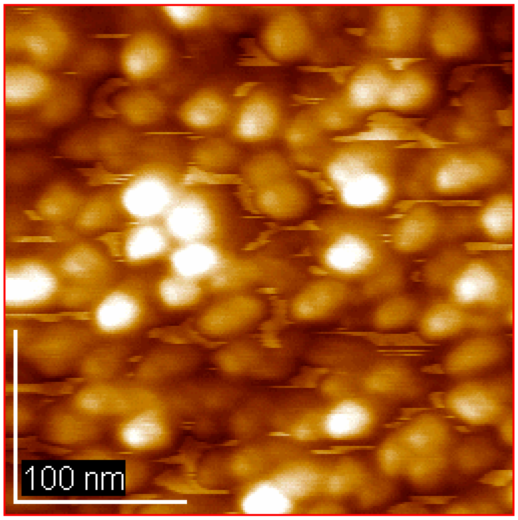

Figure 3.1. AFM image 300 nm x 300 nm of vapor evaporated Au film on a sapphire window. Au surface roughness is ~10 nm with an average particle size of 25 nm.

3.2.2. Preparation of TiO_2 nanocrystalline films on CaF_2 prisms and Au-coated sapphire windows

TiO_2 nanoparticle colloidal solution was prepared as previously described in section 3.1.1, halting the procedure before adding TritonX-100. The colloid was rotary evaporated and the nanocrystals resuspended in ethanol to form a concentrated solution. For both CaF_2 prism (ISP 45-45-90) and Au-coated sapphire substrates, 2 drops of colloid were deposited on the substrate surface, and a glass pipet used to distribute the solution uniformly to completely coat the substrate. As the solution air-dried to deposit the nanocrystalline TiO_2, the samples were continuously monitored to maintain uniformity of the drying surface. Once dried, the nanocrystalline samples were stored in an anhydrous atmosphere to prevent surface contamination, and the surface characterized by AFM to determine uniformity of TiO_2 nanoparticle distribution. As shown in Figure 3.2, the TiO_2 film roughness was measured to be ~3 nm over a surface area of 2 μm. Also present in the AFM image is a 23 nm tall surface defect 300 nm in diameter, formed from uneven surface evaporation and TiO_2 aggregation.

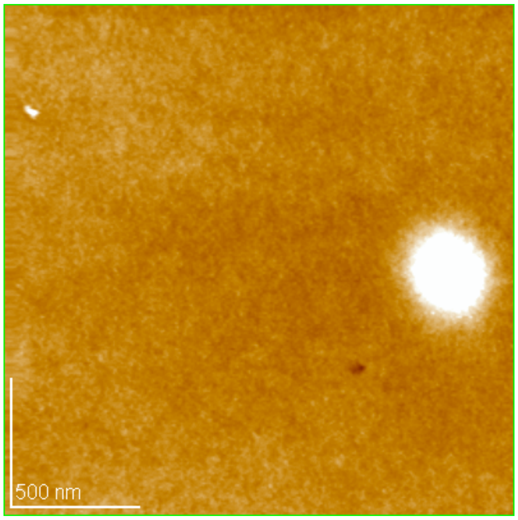

Figure 3.2. AFM image 2 μm x 2 μm of TiO_2 coated Au substrate. Average surface roughness is ~3 nm, with a 23 nm high defect appearing from nanoparticle aggregation as a results of uneven evaporation of the TiO_2 colloid solution.

3.3. Dyes Used in This Work

3.3.1. Coumarin 343

Coumarin 343 (C343) was purchased from Aldrich. It is believed that the dyes bind to the semiconductor surfaces by the carboxylate anchoring group. Figure 3.3 shows the schematic structures of C343.

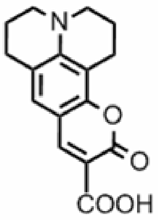

C343

Figure 3.3. Schematic structure of Coumarin 343.

3.3.2. Oligoene Dyes

Oligoene dyes NKX-Y001, NKX-O001, NKX-O002 and NKX-O005 (Y1, O1, O2 and O5, respectively) were obtained courtesy of Nippon Kayaku. Figure 3.4 shows the schematic structures of the oligoene dyes. The dyes are believed to bind to the semiconductor surfaces through the carboxylate anchoring groups at the terminus of each conjugated spacer.

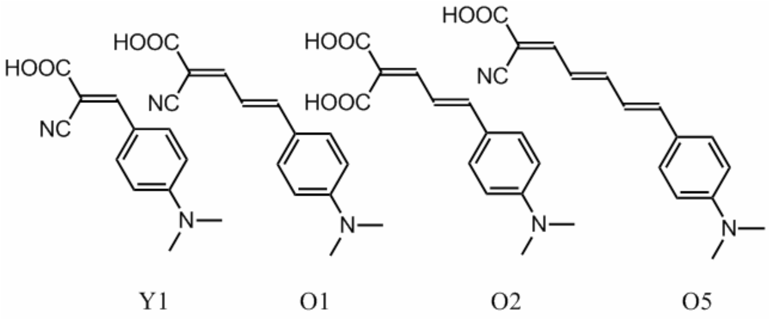

Figure 3.4. Schematic structures of oligoene dyes Y1, O1, O2 and O5.

3.3.3. Rhodamine B and Fluorescein 548

Rhodamine B was purchased from Aldrich. Fluorescein 548 was purchased from Exciton. Both dyes have carboxylic acid groups and are believed to anchor to the semiconductor surfaces through these groups. Figure 3.5 shows the schematic structure of RhB and Fl.

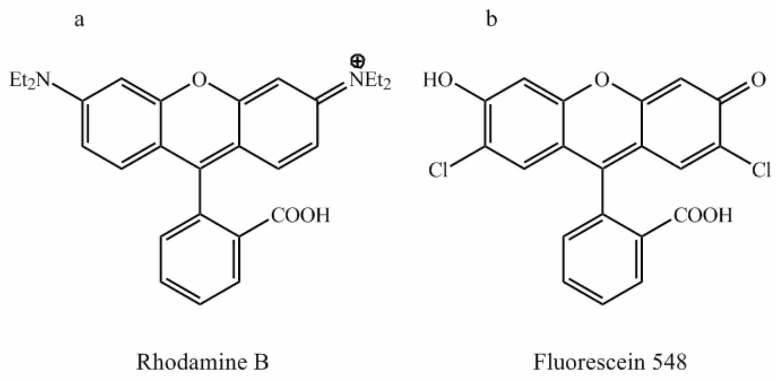

Figure 3.5. Schematic structures of (a) Rhodamine B and (b) Fluorescein 548.

3.3.4. Re polypyridyl complexes

Re(dcbpy)(CO)$_3$Cl [dcbpy = 2,2'-bipyridine-4,4'-COOH] (ReC0) was prepared according to published procedures by Dr. Debbie Mohler`s group at Emory University.[5] Re(dpbpy)(CO)$_3$Cl [dpbpy = 4,4'-(CH$_2$PO(OH)$_2$)2-2,2'-bipyridine] (ReC1P) was prepared according to published procedures by Dr. Joseph T. Hupp`s group at Northwestern University.[6,7]

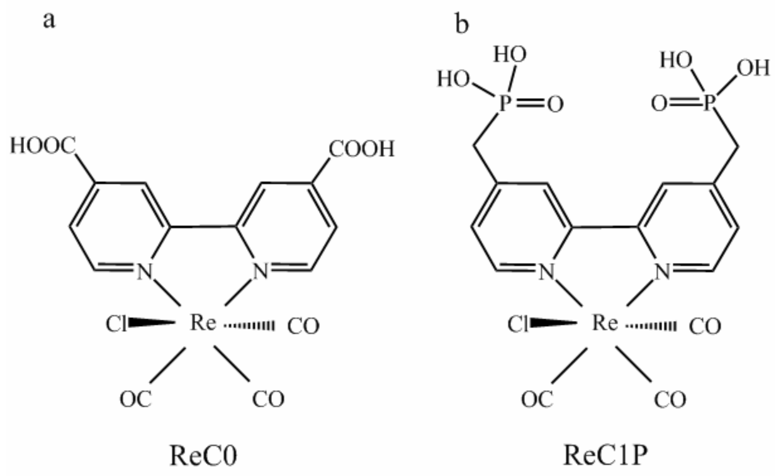

Figure 3.6. Schematic structure of (a) ReC0 and (b) ReC1P.

3.4. Sensitization of Samples

3.4.1. Sensitization of Semiconductor Nanoporous Thin Films

Semiconductor films were sensitized by immersing in ethanolic solutions of each sensitizer dye (~ 1 mg/mL concentration), followed by washing with additional solvent to remove physically adsorbed dyes. The sensitized dyes were then dried in air. The coverage levels of dye on the different semiconductor films was controlled by both the immersion time and dye solution concentration, and monitored by UV-visible absorption. The sample absorbance at the dye peak maximum was typically 0.1-0.2 OD depending on the experimental conditions as discussed in the following chapters. Sample integrity was checked by UV-visible absorption measurements over time, and no noticeable degradation of the dyes was observed during the course of infrared measurements.

3.4.2. Sensitization of Au and TiO_2 Monolayer Films

Calibration samples of octadecanethiol (ODT) were created by soaking the Au-coated sapphire substrates in 3 mM dichloromethane (DCM) ODT solution for 2 hours. The resulting self-assembled monolayers (SAMs) were then characterized as-is for spectral calibration of the SFVS apparatus. SAMs of 11-mercaptoundecanol were created using a similar method, and after confirmation of monolayer adsorption, catalytically modified overnight with 1-[3-(dimethylamino)propyl]-3-ethylcarbodiimide (EDC) and 4-dimethylaminopyridine (DMAP) in the presence of ReC0 to esterify the carboxyl anchoring group of ReC0 to the free alcohol terminating group of 11-mercaptoundecanol. Samples of both ODT and esterified ReC0 were washed with DCM after preparation to remove any thiol molecules not chemically adsorbed to the Au surface.

Both CaF_2- and Au-coated TiO_2 nanocrystalline samples were directly sensitized in Re dye solution. ReC1P samples were created by soaking the samples in EtOH solution of the dye for ~2 hours, then washing the sample surface with EtOH to remove any dye not physically adsorbed to the surface. Sensitization times longer than 2 hours did not result in an increase in signal size, indicating that full surface coverage was obtained within the sensitizing timeframe. ReC0 samples were sensitized in EtOH solution for 24 hours, and washed with EtOH. All samples were examined immediately after sensitization, then stored under dry, dark conditions when not being used to preserve sample integrity for as long as possible.

3.5. Ultrafast Transient Absorption Measurements

3.5.1. Ultrafast Mid-Infrared Transient Absorption Measurements

Ultrafast experiments were carried out in a pump-probe transient absorption scheme.[8-11] The tunable infrared spectrometer used was based on a regeneratively amplified Ti:Sapphire laser system (Coherent Legend, 800 nm, 150 fs, 2.5 mJ/pulse, 1 KHz repetition rate) and two optical parametric amplifiers (OPAs). An IR-OPA (Coherent OPerA) was pumped at 800 nm (1 mJ/pulse) to produce signal and idler outputs at 1380 nm and 1903 nm, respectively. The signal and idler were collinearly mixed in an $AgGaS_2$ crystal to produce, by difference-frequency generation, tunable mid-IR probe pulses with a full width at half-maximum (fwhm) of ~120 cm^{-1} and pulse energy of ~5 μJ at 5000 nm. The IR probe pulses were attenuated with a beam splitter and ND filters (to ~10 nJ) and chirp-corrected with Ge windows before the sample.

Pump pulses at 400 nm were generated by frequency-doubling ~100 μJ of the 800 nm fundamental in a BBO crystal. Pump pulses at all other wavelengths from 470-560 nm were generated by a home-built sum frequency setup, where either the signal or idler outputs (80 and 40 μJ, respectively) of an IR-OPA (Clark-MXR, pumped with 1 mJ of 800nm pulse) were collinearly mixed with the 800 nm beam (~100 μJ) in a BBO crystal to produce tunable pump pulses from 460 nm to 650 nm. The energy of the pump pulses used for these measurements was controlled by a variable-ND filter wheel. The pump and probe beam diameters at the sample were ~350 and 175 μm, respectively, as measured by pinhole transmission. After the sample, the probe (centered at 2000 cm^{-1}) was dispersed in a spectrometer with resolution of 15 nm (5.4 cm^{-1} at 2000 cm^{-1}) and detected with a 32-element mercury cadmium telluride (MCT) array detector. Every other pump pulse was blocked by a synchronized chopper (New Focus 3500) at 500 Hz, and the absorbance change was calculated from sequential pumped vs. unpumped probe pulses.

The instrument response function and zero time delay were determined with a thin Si wafer, which gives an instantaneous mid-IR absorption response after excitation at 400 nm. Typically, the instrument response function was well fit by a Gaussian function with 160 fs fwhm. During the data collection, samples were constantly translated at a speed of 5 mm/min to avoid photodegredation.

3.5.2. Ultrafast Visible Transient Absorption Measurements.

Pump pulses were generated as described in the previous section and focused on the sample with a beam diameter of 300 μm and variable energies as described previously. The visible probe was generated by attenuating and focusing ~2 μJ of the 800 nm fundamental into a rotating 2 mm thick CaF_2 window to produce a white light continuum from 370 to 700 nm. The probe was focused on the sample using protected Al parabolic reflectors to a spot size of 150 μm. After the sample, the probe was focused into a fiber-coupled spectrometer (Ocean Optics HR2000+, 2048 pixel CCD, ~.40 nm/pixel readout) and detected at a frequency of 100 Hz. The pump pulses were chopped by a synchronized chopper to the same frequency. Zero time delay and the instrument response function were obtained with the instantaneous ground state bleach at 435 nm of C343 in ethanol solution. Samples were translated as described previously to prevent long term photodegredation.

3.6. Time Resolved Fluorescence Lifetime Measurements.

Time–resolved fluorescence measurements were performed in the time-correlated single photon counting (TCSPC) mode under right-angle sample geometry.[12-14] Femtosecond laser pulses (~100 fs) with a repetition rate of 80 MHz were generated in a mode-locked Ti:Sapphire laser (Tsunami oscillator pumped by 10 W Millennia Pro, Spectra-Physics). The output centered at 800 nm was doubled in a BBO crystal to generate pump pulses at 400 nm. The emission was detected by a micro-channel-plate-photomultiplier tube (Hamamatsu R3809U-51), the output of which was amplified and analyzed by a TCSPC board (Becker&Hickel SPC 600).

3.7. Sum Frequency Vibrational Spectroscopy Measurements

SFVS spectra were obtained using two different laser systems, the details of which will be outlined briefly. Au-coated sapphire samples were examined using a

Clark-MXR CPA-1000 ultrafast Ti:sapphire laser producing 120 fs pulses with ~900 μJ/pulse of 800 nm fundamental output (12 nm bandwidth FWHM). 600 μJ of fundamental light was split off to pump a Clark-MXR IR-OPA, generating signal and idler near-IR pulses at ~1.4 and 1.9 μm. Tunable mid-IR pulses were generated in an $AgGaS_2$ crystal through difference frequency combination of the signal and idler with energy ~1 μJ/pulse. The remaining 300 μJ of 800 nm fundamental was passed through a delay stage to ensure mid-IR and 800 nm pulses arrived at the sample simultaneously, and filtered with a narrowband interference filter (CVI F01-800-UNBLK-1.00) to narrow the spectral bandwidth to ~12 cm^{-1} (1 nm) centered at 799 nm with pulse energy ~500 nJ.

Total internal reflection (TIR) measurements were performed using a Coherent Legend-H Ti:sapphire laser producing 120 fs fundamental pulses at 800 nm with pulse energy 2.4 mJ. 1.1 mJ of the fundamental was split off and used to pump a Coherent IR-OPA (OPerA) to generate signal and idler near-IR pulses at 1.38 and 1.9 μm. The signal and idler were then passed through an $AgGaS_2$ crystal to create tunable mid-IR pulses with energy ~7 μJ. The remaining 600 μJ of fundamental rejected from the OPerA was then sent through a delay line and filtered to narrow the bandwidth as described previously, leaving ~20 μJ of narrowband visible light for use in the SFVS setup.

The SFVS apparatus was of identical construction for both laser systems used, the only variation being pulse energies at the sample depending on laser. Both narrowband 800 nm and broadband mid-IR pulses passed through half-waveplates, then thin-film polarizers to select the appropriate polarization with which to pump the sample. The beams were focused so that spot size at the sample for each beam is ~500 μm. The resultant SF signal was recollimated, and after passing through an additional halfwaveplate and polarizer to select the desired polarization for detection, filtered using a 700 nm shortpass filter (CVI-SPF-700-1.00) and 800 nm Raman notch filter (CVI-RNF-800.0-1.00) to remove any stray visible light that might interfere with data collection. Remaining signal was focused onto the slit of an imaging spectrograph (Acton Instruments SpectraPro 300i, 1200 groove/mm grating). Detection of the dispersed signal was accomplished with an air-cooled CCD camera (Princeton Instruments VersArray 512B) operating at -40.0 C. with spectral resolution of 1.2 cm^{-1}/pixel.

References

(1) Zaban, A.; Ferrere, S.; Sprague, J.; Gregg, B. A. *J. Phys. Chem. B* **1997**, *101*, 55.

(2) Kalyanasundaram, K.; Gratzel, M. *Coordination Chemistry Reviews* **1998**, *177*, 347.

(3) Nutz, T.; Felde, U. Z.; Haase, M. *J. Chem. Phys.* **1999**, *110*, 12142.

(4) Spanhel, L.; Anderson, M. A. *J. Am. Chem. Soc.* **1991**, *113*, 2826.

(5) Anderson, N. A.; Ai, X.; Chen, D.; Mohler, D. L.; Lian, T. *Journal of Physical Chemistry B* **2003**, *107*, 14231.

(6) Walters, K. A.; Gaal, D. A.; Hupp, J. T. *Journal of Physical Chemistry B* **2002**, *106*, 5139.

(7) Yan, S. G.; Prieskorn, J. S.; Kim, Y.; Hupp, J. T. *Journal of Physical Chemistry B* **2000**, *104*, 10871.

(8) Anderson, N. A.; Asbury, J. B.; Hao, E.; Ai, X.; Lian, T. *Proceedings - Electrochemical Society* **2001**, *2001-10*, 97.

(9) Wang, Y.; Asbury, J. B.; Lian, T. *J. Phys. Chem. A* **2000**, *104*, 4291.

(10) Ghosh, H. N.; Asbury, J. B.; Weng, Y.; Lian, T. *J. Phys. Chem. B* **1998**, *102*, 10208.

(11) Huang, J.; Stockwell, D.; Boulesbaa, A.; Guo, J.; Lian, T. *J. Phys. Chem. C* **2008**, *112*, 5203.

(12) Goh, W.; Guo, J.; Yuan, R.; Lian, T. “Single molecule study of Rhodamine/ATO nanoparticle junctions”; Proceedings of SPIE-The International Society for Optical Engineering, (Physical Chemistry of Interfaces and Nanomaterials IV), 2005.

(13) Jin, S.; Issac, A.; Stockwell, D.; Yin, F.-C.; Kindt, J.; Batista, V. S.; Robert, S.; Lian, T. **to be submitted**.

(14) Issac, A.; Jin, S.; Lian, T. *J. AM. Chem. Soc.* **2008**, *accepted*.

Chapter 4. Interfacial electron transfer from Coumarin-343 to TiO_2, SnO_2 and ZnO nanocrystalline thin films

4.1. Introduction

Interfacial electron transfer (ET) between molecular adsorbates and semiconductor nanocrystals has been a subject of intense interest in recent years due to the wide field of applications available for this class of systems, one of which under high scrutiny has been solar light harvesting for energy conversion purposes.[1-4] The sensitization of wide band-gap semiconductors with organic and inorganic chromophores has shown potential in development of a low cost high-efficiency solar cell that can provide a substitute to more expensive and environmentally destructive silicon-based technologies in use today. Ideally, on photoexcitation of the chromophore, a fast and high-yield charge separation from the chromophore excited state leads to an instantaneous dissociation of an intermediately-bound charge separated pair called an exciplex (exc). This results in a total charge separation (CS) rate that can be used to describe the electron transfer process from photoexcited adsorbate to semiconductor, where the timescale of charge recombination (CR) with the oxidized donor is orders of magnitude longer than the initial charge transfer as shown in Equation 4.1

$$\begin{tikzcd} dye\text{-}SC \arrow[r, "h\nu"] & dye^{*}\text{-}SC \arrow[r, "k_{exc}"] & dye^{\delta+}\text{-}SC^{\delta-} \arrow[r, "k_{CS}"] \arrow[ll, bend left] & dye^{+}\text{-}SC^{-} \arrow[lll, bend left, "k_{CR}"] \end{tikzcd} \tag{4.1}$$

where dye, dye^{*}, $dye^{\delta+}$ and dye^{+} represent the donor ground, excited, charge-separated exciplex and oxidized states respectively. Although TiO_2-based solar cells using Ru-

(4,4’-dicarboxy-2,2’-bipyridine)$_2$(NCS)$_2$ (RuN3) currently exhibit the highest conversion efficiencies to date of 10%, other semiconductors such as SnO_2 and ZnO have been studied in detail with RuN3 as a means to elucidate the mechanisms by which charge transfer occurs based on the nature of both the electron donor and the accepting medium.[5-18] TiO_2 showed a biphasic injection mechanism, with an ultrafast (<100 fs) charge separation component of >50% and a slower component over several picoseconds, while SnO_2 and ZnO showed much smaller ultrafast components and injection was dominated by the slower component (several picoseconds or longer), attributed to the conduction band characteristics of the particular semiconductor.[19] These injection measurements assume straightforward models of one or more excited donor states contributing to the kinetics involved with the charge transfer process. Recently, new observations of dye-semiconductor systems have suggested mechanisms differing from those described above through which electron transfer can occur.

It has been recognized that photoexcitation of one molecule in a coupled system can result in a stable heterogeneous excited-state complex (exciplex) not present in ground-state measurements.[20-22] A more recent study of RuN3 adsorbed on ZnO nanocrystals utilized the near-IR absorption of transient species to suggest an intermediate charge-transfer complex between RuN3 and ZnO. This excited-state complex (exciplex) directly affected the electron injection kinetics based on the donor/acceptor states involved in forming the exciplex.[23,24] A number of factors were suggested in the formation of this exciplex, including ZnO preparation, RuN3 adsorption to various sites on the nanocrystal, and the nature of state mixing to define the exciplex. In related works, charge transfer intermediates have been proposed for a variety of organic dyes on semiconductor films, leading to the need for investigation of mechanistic differences in the electron transfer process as well as differences in electronic structure of the accepting films.[25-28]

Through examination of different sensitizer/semiconductor systems, a greater understanding of the overall electron transfer process has been gained.[29-34] Organic chromophores, which usually exhibit lower conversion efficiencies, provide useful information in that through a combination of spectroscopic methods a clearer picture of charge transfer dynamics is assembled. Observation of transient donor species in comparison to semiconductor free carrier absorption has proved a powerful tool in assigning direct charge-transfer mechanisms to individual species over time. One of the most highly studied systems of organic families is the coumarin dyes, the investigations of which have yielded information regarding electronic structure, transient species, and interactions of the coumarins with chemically-adsorbed surfaces.[35-45]

In this chapter, a comparison is presented of both the transient mid-IR and visible dynamics of Coumarin-343 (C343) adsorbed on TiO_2, SnO_2 and ZnO. C343 is an ideal adsorbate in that it has been well-characterized in previous studies.[36,37,39,41,43,46-48] Transient mid-IR measurements have proven useful in their ability to directly measure arrival of an injected electron into the acceptor conduction band while avoiding spectral overlap of donor species in this region. However, transient visible measurements allow spectral observation of donor-related features that would otherwise be neglected in the course of a single type of measurement. By combining these two techniques, we show a direct relationship between the dynamics of electron injection as measured by ultrafast mid-IR measurements, and the transient donor species and intermediates measured by ultrafast visible measurements. The relationships between the two measurements will be discussed, as well as the proposed differences in electron injection mechanisms between the various semiconductors. Since it is known that organic molecules with large π-conjugated systems aggregate at sufficient concentrations on adsorbate surfaces, this is taken into consideration in presenting results, demonstrating that under the proper conditions interactions between photoexcited C343 are minimized.

4.2. Results

4.2.1. C343/EtOH

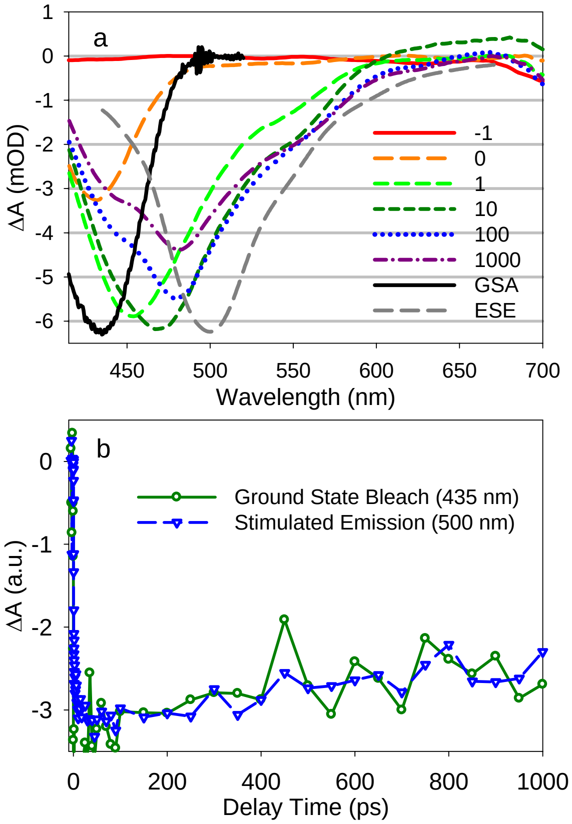

Figure 4.1. (a) Transient visible absorption spectra of C343 in EtOH solution at different delay times after 400 nm excitation. Also plotted against the negative vertical axis for comparison are the static UV-vis absorption (GSA, black solid line) and emission (ESE,

gray dashed line) spectra of C343/EtOH. Features in the transient spectra consist of the bleach of C343 ground state absorption at 435 nm and stimulated emission (470-600) corresponding to excited state C343. (b) Time-resolved kinetics of the ground state bleach at 435 nm (GSB, solid green line) compared with the stimulated emission at 500 nm (dashed blue line). The two features decay with identical kinetics within the time window observed, indicating that excited state population is the only species present.

In order to assign the spectral features associated with C343 observed as a result of direct photoexcitation, we use a solution of C343 in ethanol (EtOH). Photophysics of C343 in solution have been extensively studied, and it is known that the C343 excited state lifetime in EtOH is on the order of nanoseconds, much longer than the time resolution of the transient measurements. As such, we expect after photoexcitation only features associated with the long-lived excited state population in solution. Figure 4.1a shows the transient spectra of C343 in EtOH (4 x 10^{-4} M, 200 μm sample length) after excitation at 400 nm with pulse energy 80 nJ. Low pump energy was used in order to minimize intermolecular energy transfer that might quench excited state population. The different spectra in Figure 4.1a reflect multiple time delays between pump and probe from -1 to 1000 ps, and the ground state absorption and excited state emission (GSA and ESE, respectively) are inverted and scaled for comparison to the features observed in transient measurements. Immediately after photoexcitation, the two features observed in the transient spectra correspond to depletion of ground state C343 and the associated formation of excited state population. The negative feature centered at 435 nm is the ground state bleach (GSB) of C343, where the instantaneous decrease in population is reflected by the negative lineshape of the GSA. Similarly, the excited state population formed after photoexcitation is represented in the spectra by the negative feature from 470-600 nm corresponding to stimulated emission (SE), matching the spectrum of ESE. The excited state absorption of C343 is not within the spectral window available for the measurements, but the presence of stimulated emission confirms excited C343 for the purpose of observing changes in population of the species. At early time over tens of picoseconds, there is a dynamic Stokes shift of emission wavelength due to solvent reorientation in EtOH as demonstrated by the early time spectra.

Figure 4.1b shows the time-dependent kinetics of the GSB at 435 nm and SE at 500 nm up to 1 ns. The two wavelengths have been averaged over a 10 nm width and scaled to better reflect the similarities in late-time kinetics. At early time, as mentioned previously, the Stokes shift of emission wavelength causes the kinetics to be represented by a slower rise than the actual instantaneous formation. At later times after tens of picoseconds, however, it can be clearly observed that ground state depopulation and excited state emission are correlated, where the small recovery of ground state bleach up to 1 ns is reflected in the decrease in emission intensity. These observations are further supported by fluorescence lifetime measurements that show the excited state of C343 in EtOH to be nanoseconds long (not shown). With no other favorable pathways for energy transfer from excited C343, we show that within the time duration of the transient measurements the relative change in excited state population due to photoexcitation is within the limits of expected radiative lifetimes for the system.

4.2.2. C343/TiO$_2$

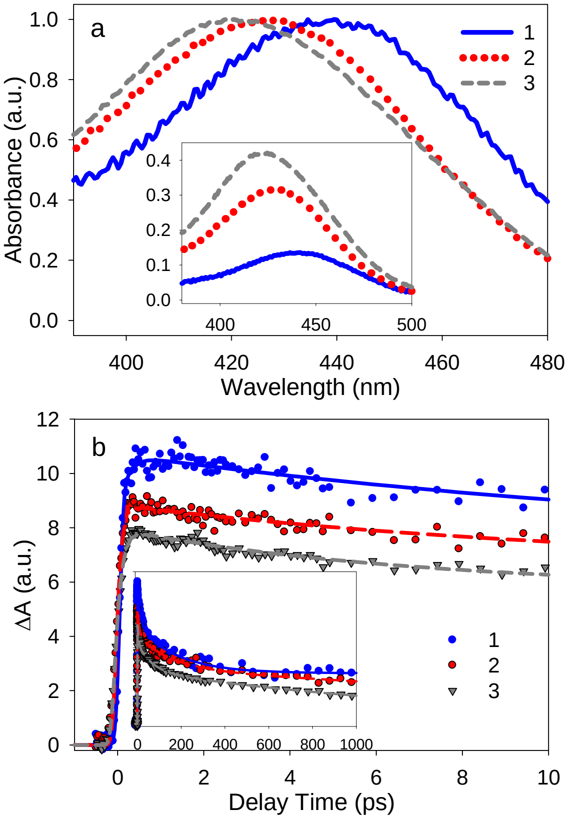

Figure 4.2. (a) C343/TiO$_2$ UV-visible spectra of three different dye coverage levels, 1 (0.08 OD), 2 (0.16 OD) and 3 (0.24 OD). The noticeable blueshift of absorption maxima as coverage increases indicates onset of H-aggregation. The inset shows the original spectra. (b) Time-resolved mid-IR absorption kinetics of loading samples 1, 2 and 3 scaled to reflect the number of absorbed photons at 400 nm. The inset shows the same kinetics up to 1 ns.

4.2.2.1 Transient IR measurement of dye coverage dependence.

As mentioned in the previous section, intermolecular quenching as a result of dye aggregation on the semiconductor surface affects the excited state lifetime of C343 when compared to solution-phase measurements. It is well known that organic molecules with large π– conjugated systems form ordered aggregates at sufficiently high coverage, requiring a study into the effects of C343 coverage on other substrates, and how these potential aggregates influence injection at varying surface concentration levels. Figure 4.2a shows the normalized UV-visible absorption spectra of C343 adsorbed on TiO_2 at three different loading levels and the inset shows the actual absorbances of the films, with loading levels at 400 nm of 0.08, 0.16 and 0.24 OD for samples 1, 2 and 3, respectively. Immediately evident from examination of the normalized spectra is a 15 nm blueshift of the absorption maximum as C343 loading increases. From a more detailed study of loading versus absorption peak (not shown), this change begins nearly immediately, indicating that C343 tends to aggregate on TiO_2 even at very low levels. It is believed that this blueshift of absorption maximum is a direct result of H-aggregation on the surface.

Shown in Figure 4.2b are the early time absorption dynamics of injected electrons in TiO_2 following 400 nm excitation of the adsorbed C343 and the inset shows electron absorption dynamics extended to later time scale. Upon photoexcitation of C343, an electron is promoted from the HOMO to the LUMO, energetically ~0.7 eV above the TiO_2 conduction band edge with sufficient driving force for electron transfer from C343 to TiO_2 through the salicylate anchoring group[49]. Upon injection of an electron to the TiO_2 conduction band a broad positive free carrier absorption in the mid-IR region is observed as shown for TiO_2 in Figure 4.2b. The probe wavelength used was ~5000 nm, where the absorption of C343 is negligible, resulting in signal that reflects only the population of injected electrons at a given delay time. The signal amplitudes are scaled to reflect the number of absorbed excitation photons at 400 nm in order to indicate the relative injection yields at each coverage level. A comparison of the three different loading levels shows a noticeable effect of increasing dye concentration on injection yield. Electron injection from C343 to TiO_2 is instantaneous for all three samples; however, the relative injection yields of the higher-loading samples are ~10% and 15% lower for samples 2 and 3, respectively, when compared to sample 1. These changes in injection yield at higher loading levels are attributed to intermolecular quenching of the C343 excited state as a result of aggregation.

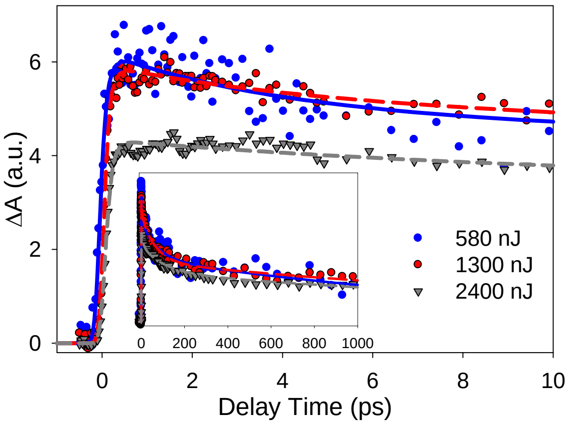

Figure 4.3. Time-resolved mid-IR absorption kinetics of C343/TiO_2 films pumped at different 400 nm excitation densities of 1894, 4245 and 7837 $\mu J/cm^2$ (shown as 580, 1300 and 2400 nJ, respectively) The signals have been scaled by the corresponding pump power. The inset shows the same kinetics up to 1 ns.

4.2.2.2 Transient IR measurement and excitation power dependence.

At sufficiently low dye coverage levels, it is expected that the excited state deactivation pathway due to molecular aggregation becomes negligible. However, it has been previously shown using RuN3-sensitized SnO_2 that molecular proximity is not necessarily required for competive quenching processes. Even in samples with negligible aggregate formation, high excitation power densities have the capability to introduce nonradiative intermolecular energy transfer by exciting sufficient quantities of neighboring adsorbates. In order to examine this effect on injection dynamics, three different excitation densities of 1894, 4245 and 7837 $\mu J/cm^2$ (corresponding to 580, 1300 and 2400 nJ/pulse, respectively) at 400 nm were used to pump a C343/TiO_2 film with absorbance at 400 nm of 0.09 OD. By minimizing aggregate-induced quenching, we were able to make a determination of the excitation powers necessary to minimize intermolecular interactions. Figure 4.3 shows the IR transient absorption kinetics of C343/TiO_2 at the three pump powers mentioned previously. The signal sizes have been scaled by the corresponding pump powers in order to reflect the relative injection yields as affected by excitation density. Clearly, at the highest pump power (2400 nJ) the injection yield is decreased compared to the two lower pump powers. At these two pump powers (1300 and 580 nJ), the kinetics and injection yield are nearly identical, suggesting that at these excitation powers and C343 coverage level, quenching between excited adsorbates is unaffected by either molecular aggregation or overpumping of neighboring dyes. Further comparison of C343 injection kinetics with other systems will subsequently use data collected under similar conditions for analysis and discussion.

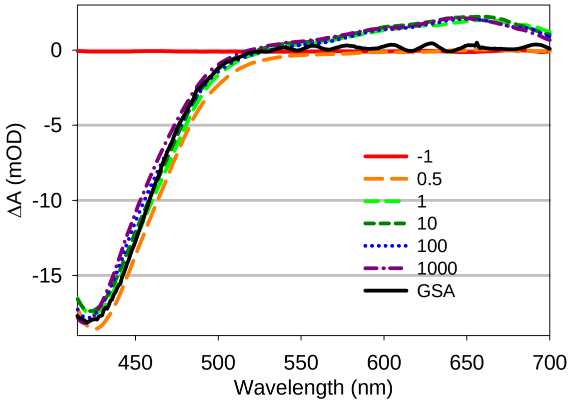

Figure 4.4. Transient visible absorption spectra of C343/TiO_2 at delay times up to 1 ns after 400 nm excitation. The ground state absorption (GSA, thick black line) has been inverted and scaled for a better comparison with the corresponding bleach. The legend indicate the delay time for each spectrum in picoseconds. The growth of C343 cation absorption at 630 nm is instantaneous, indicating sub-150 fs electron transfer from C343 to TiO_2. At later delay times, the spectra show only the constant presence of the C343 cation absorption and ground state, indicating a long-lived charge separation.

4.2.2.3 Transient visible spectra of C343/TiO_2.

In addition to probing the mid-IR absorption of injected electrons in TiO_2, we use transient visible absorption spectroscopy in order to observe the dynamics of C343 species during the charge transfer process. Figure 4.4 shows the transient visible absorption spectra of C343/TiO_2 (sample absorbance 0.15 OD at 400 nm, pumped with 35 nJ/pulse) up to 1 ns after excitation. The observed species consist of the ground state bleach at 430 nm, and cation absorption at 630 nm. The presence of stimulated emission corresponding to longer-lived excited state C343 is negligible, indicating an injection yield near unity. The static UV-visible ground state absorption (GSA) of C343/TiO_2, shown as a thick black line, has been inverted and scaled for comparison. After initial excitation of C343, we observe the instantaneous formation of the cation absorption band. At later delay times, the transient spectra consist of only two features corresponding to ground state bleach of C343 and the absorption due to oxidized C343. This can be confirmed by the presence of an isosbestic point at 520 nm through the entire later time delay windows, indicating that no other species are formed or depleted. This suggests that nearly all excited C343 is depleted to form cation, and the charge separation after electron injection to TiO_2 is very long lived, greater than the observation limit our 1 ns time window allows.

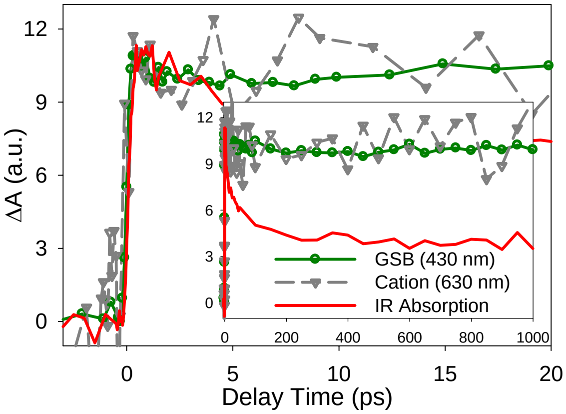

Figure 4.5. Comparison of early-time dynamics of mid-IR electron absorption in TiO_2 (red solid line) with C343 cation absorption (open triangles, dashed line). The signal from oxidized C343 has been averaged over 600-650 nm to increase signal-to-noise and scaled to provide better comparison with the IR injection dynamics. The good agreement confirms the instantaneous process of electron injection. The inset shows a comparison of late-time dynamics of mid-IR electron absorption with C343 cation absorption. The

difference in kinetics between the two species suggests relaxation of the injected electron through the conduction band of TiO_2 due to the decay in IR absorption compared to the constant presence of oxidized C343 in the visible region with no obvious ground state recovery.

4.2.2.4 Comparison of IR absorption and visible spectral signatures.

By comparing kinetics of the different species formed through charge transfer using mid-IR and visible transient absorption, we provide a clear comparison of injection dynamics from both the donor and acceptor standpoints, allowing an unambiguous assignment of the observed signals. Figure 4.5 shows the early time dynamics of mid-IR electron absorption in C343/TiO_2 compared to the absorption of C343 cation at 630 nm. The IR signal was obtained from a C343/TiO_2 film with sample absorbance of 0.11 OD using a pump power of 160 nJ in order to minimize both aggregate- and excitation-dependent quenching effects. The kinetics of cation absorption were obtained by averaging the total absorption from 600-650 nm, where it is shown in Figure 4.4 to be the only contribution to the spectra in that region. Clearly, the good agreement between both signals indicates an instantaneous injection process, forming the C343 cation and injected electrons in TiO_2. The inset of Figure 4.5 shows the late-time dynamics as a comparison of IR electron absorption in TiO_2 with absorption of the C343 cation at 630 nm and C343 ground state bleach at 430 nm. After 150 fs, when injection is shown to be complete as in Figure 4.5, the signals deviate in kinetics. The good agreement between constant oxidized C343 absorption and the lack of ground state regeneration suggests that the decay in IR signal results from electron cross-section decay as it relaxes through the conduction band in TiO_2, rather than recombination of the electron with C343 cation. By demonstrating that the early time dynamics indicate charge transfer through both IR and visible features, we show that injection dynamics in different semiconductors can be well represented by their IR absorption, due to greater signal-to noise ratio.

4.2.3. C343/SnO_2

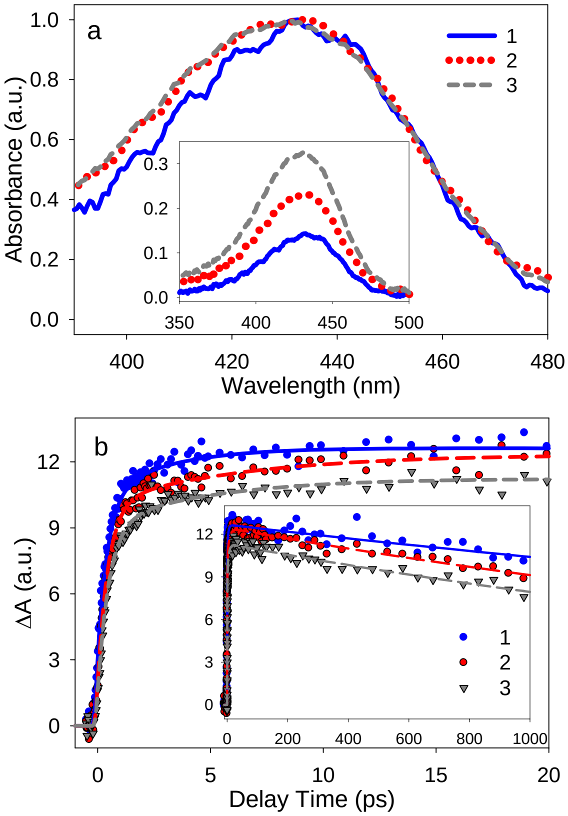

Figure 4.6. (a) UV-visible spectra of C343/SnO_2 films at three different dye coverage levels, 1 (0.07 OD), 2 (0.14 OD) and 3 (0.19 OD). The spectra have been normalized to compare the coverage levels with peak maxima. The inset shows the original spectra. (b) IR transient absorption kinetic traces after 400 nm excitation. The inset shows the data extended to longer time scale. Signal sizes have been scaled by the number of absorbed excitation photons, reflecting the relative injection yield of each sample.

4.2.3.1 Transient IR measurement of dye coverage dependence.

Figure 4.6a shows the UV-visible spectra of different C343/SnO_2 films at different dye coverage levels (0.07, 0.14, and 0.19 OD at 400 nm for samples 1, 2 and 3 respectively). The spectra have been normalized for comparison and show negligible absorption peak shift resulting from aggregation as C343 concentration increases. The inset shows the absorbance of the films before normalization. The IR absorption of injected electrons in these films is shown in Figure 4.6b, where after 400 nm excitation (~260 nJ/pulse) the transient absorption was recorded, centered at 5000 nm. The signal amplitudes have been scaled by the number of absorbed photons (sample OD) in order to show a better comparison of the effect of increasing C343 concentration. Injection kinetics for the three samples are nearly identical, even at longer delay time up to 1 ns (inset), but samples 1 and 2 (corresponding to 0.07 and 0.14 OD, respectively) show a higher injection yield than sample 3 (0.19 OD). Because aggregation has been determined to be negligible, the lower injection yield resulting from increasing C343 concentration is attributed to intermolecular energy transfer, quenching excited state C343 as a result of molecular proximity on the SnO_2 surface.

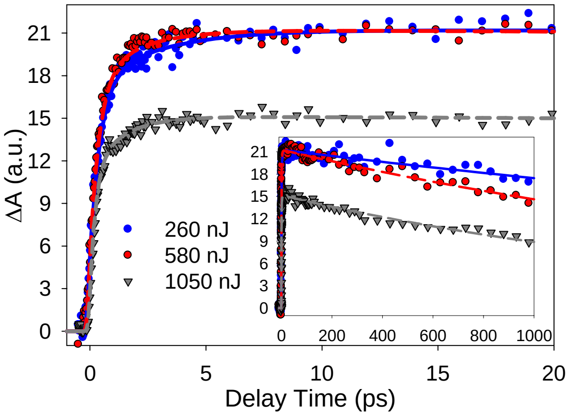

Figure 4.7. Transient IR absorption kinetics of C343/SnO_2 (0.14 OD) at different excitation densities of 849, 1894 and 3429 μJ/cm^2 (shown as 260, 580 and 1050 nJ/pulse). Signal sizes have been scaled by the corresponding pump powers in order to compare the relative injection yield. The inset indicates signal at later time delay.

4.2.3.2 Transient IR measurement and excitation power dependence.

Figure 4.7 shows the IR absorption kinetics of a C343/SnO_2 film (absorbance 0.09 OD at 400 nm) pumped with three excitation densities at 400 nm of 849, 1894 and 3429 μJ/cm^2 (shown in Figure 4.7 as 260, 580 and 1050 nJ/pulse). The signal sizes have been scaled by the corresponding pump powers in order to reflect the relative injection yields, with longer time delay shown in the inset. At all excitation densities, the electron absorption follows similar kinetics, but for lower pump powers of 260 and 580 nJ, the relative injection yield is the same while the highest pump power of 1050 nJ gives a relative yield ~25% less, as well as the exclusion of a small slower injection component lasting ~20 ps. This suggests that at pump powers of significant intensity, quenching between neighboring excited C343 on SnO_2 becomes a competitive relaxation pathway even in the absence of aggregation. At sufficiently low pump powers, as in the 260 and 580 nJ samples, this quenching is shown to be negligible. At low coverage, the slower injection component results from longer-lived excited states of C343 which are subsequently suppressed once surface concentration allows for intermolecular energy transfer to occur. Therefore, at higher dye coverage, the percentage of molecules that would normally undergo slower electron transfer is negligible, resulting in an overall decrease in injection efficiency between C343 and SnO_2. Comparisons of dynamics of C343/SnO_2 will subsequently be shown using data taken under conditions that minimize the quenching effects of molecular proximity and excitation density.

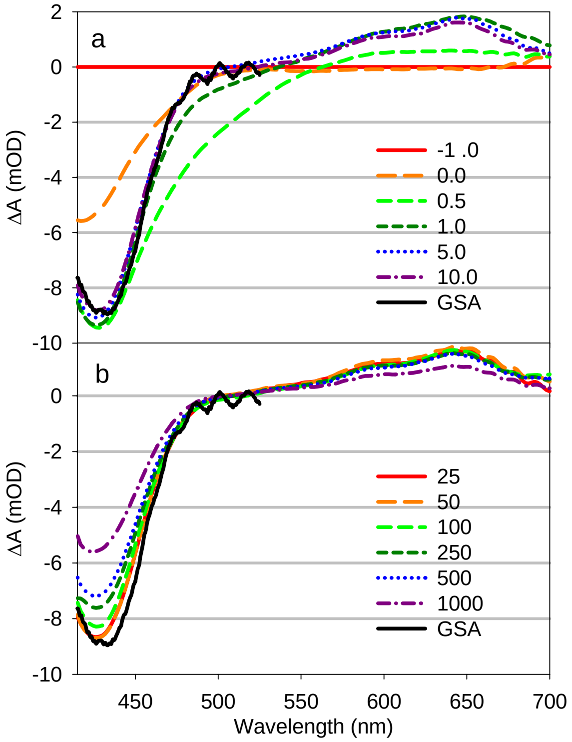

Figure 4.8. Transient visible absorption spectra of C343/SnO_2 at delay times (a) -1.0 to 10 ps and (b) 25 to 1000 ps after 400 nm excitation. The ground state absorption (GSA,

thick black line) has been inverted and scaled for a better comparison with the corresponding bleach. The legends indicate the delay time for each spectrum in picoseconds. At early time delays (a), the spectra show the formation and rapid decay of stimulated emission corresponding to excited state C343 at 500 nm. The growth of C343 cation absorption at 630 nm follows the decay of stimulated emission, indicating complete electron transfer from C343 to SnO_2. At later delay times (b) after 10 ps, the spectra show only the decay of the C343 cation absorption and recovery of the ground state bleach at 430 nm, which exhibit identical kinetics and can be attributed to the recombination of injected electrons with oxidized C343.

4.2.3.3 Transient visible spectra of C343/SnO_2.

Figures 4.8a and 4.8b show the visible transient absorption spectra of C343/SnO_2 at different delay times after excitation (sample absorbance 0.14 OD at 400 nm, with pump power 580 nJ/pulse). The transient spectra at early delay time (up to 10 ps) are shown in Figure 4.8a. Directly after excitation, the ground state bleach of C343 at 430 nm is observed, as well as stimulated emission associated with the excited state of C343 from 470-530 nm. The ground state absorption spectrum (GSA) is shown inverted for comparison (black solid line). Up to 5 ps, we observe the decay in signal from C343 stimulated emission, and the formation of the C343 cation absorption at 630 nm, indicating electron injection within this window from excited C343 to SnO_2. After 10 ps, as shown in Figure 4.8b, the only features contributing to the difference spectra are the C343 cation absorption and ground state bleach, as evidenced by the identical relative absorption/bleach ratios at different time delays and isosbestic point present at 505 nm.

This gives additional evidence that the electron transfer process is completed well within the early time window, and any changes in relative signal intensities for oxidized and ground state C343 are directly related to the process of electron recombination from SnO_2 to oxidized C343.

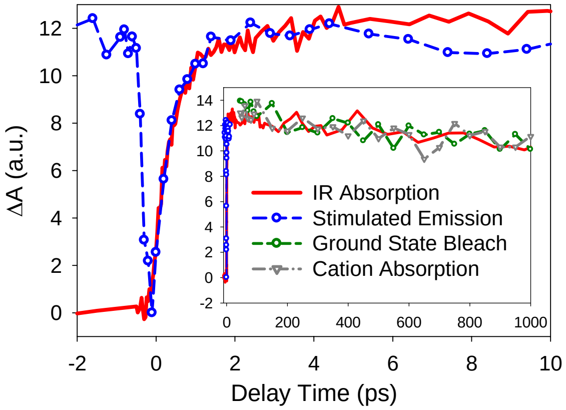

Figure 4.9. Comparison of early-time dynamics of mid-IR electron absorption in SnO_2 (red solid line) and C343 stimulated emission (SE) quenching at 500 nm (blue open circles, dashed line). The signal from SE has been averaged over 490-510 nm to increase signal-to-noise, and inverted and scaled to provide better comparison with the IR injection dynamics. The good agreement confirms the process of electron injection. Inset: comparison of late-time dynamics of mid-IR electron absorption with C343 cation absorption at 630 nm (gray open triangles, dash-dotted line) and ground state bleach at 430 nm (green open circles, dashed line). The signals from C343 cation absorption and GS bleach have been scaled accordingly for comparison with the IR absorption. The good agreement in kinetics between the three species indicates recombination of the injected electron with C343, reforming molecules in the ground state.

4.2.3.4 Comparison of IR absorption and visible spectral signatures.

A comparison of the IR electron absorption kinetics in SnO_2 with the excited state (stimulated emission) quenching of C343 is shown in Figure 4.9. The SE kinetics were obtained by averaging the signal from 490-510 nm at different time delays, and scaled for a better comparison with the electron absorption kinetics at 5000 nm. The kinetics of electron absorption in SnO_2 agree well with the C343 excited state quenching, indicating electron transfer from C343 to SnO_2 with negligible competitive deactivation pathways contributing to the observed signal.

At later time delay, as shown in the inset of Figure 4.9, the decay in oxidized C343 absorption (630 nm) and ground state bleach recovery (430 nm) agree well with the observed decay in electron absorption. These signals indicate that at later times, the decrease in mid-IR electron absorption is a direct observation of recombination from SnO_2 to oxidized C343, rather than electron cross section decay as a result of relaxation through the SnO_2 conduction band.

4.2.4. C343/ZnO

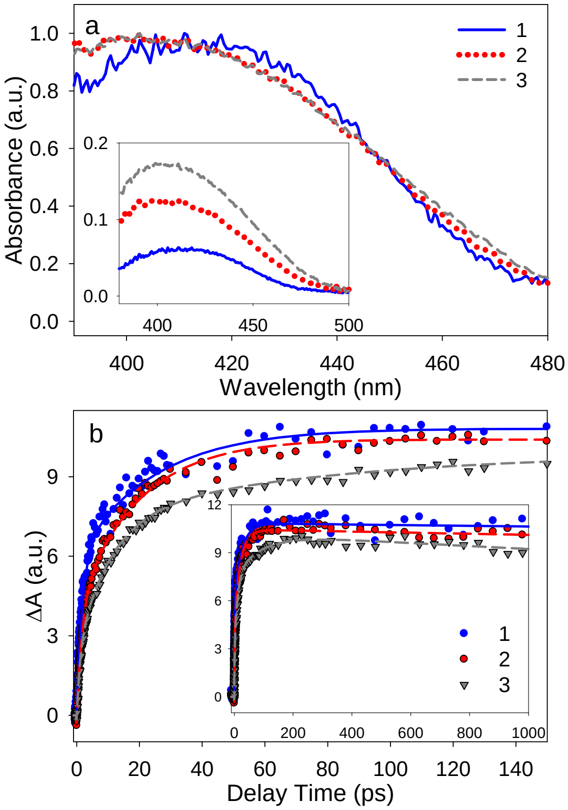

Figure 4.10. (a) UV-visible spectra of C343/ZnO films at three different dye coverage levels, 1 (0.06 OD), 2 (0.12 OD) and 3 (0.17 OD). The spectra have been normalized to compare the coverage levels with peak maxima. The inset shows the original spectra. (b) IR transient absorption kinetic traces for all samples after 400 nm excitation. The inset shows the data extended to 1 ns. Signal sizes have been scaled by the number of absorbed excitation photons, reflecting the relative injection yield of each sample.

4.2.4.1 Transient IR measurement of dye coverage dependence.

The normalized absorption spectra for samples of C343/ZnO with different dye coverages (0.06, 0.12 and 0.17 OD for samples 1, 2 and 3 at 400 nm, respectively) are shown in Figure 4.10a, where the inset shows the actual absorbance of the three films. An

8 nm blueshift of absorption peak maximum is evident as dye loading increases, from 413 nm at low coverage to 405 nm at higher coverage. This shift in absorption maximum is attributed to H-aggregation of the C343 dyes as concentration on the ZnO surface increases, even at relatively low loading levels.

Shown in Figure 4.10b are the transient electron absorption measurements for all samples. The samples were pumped at 400 nm with ~460 nJ/pulse and probed at 5000 nm. The signal sizes are scaled to reflect the relative injection yield of each sample based on the number of absorbed photons at 400 nm. The injection kinetics are quite similar for all samples, however the high-loading sample 3 shows a ~10% decrease in relative injection yield when compared to samples 1 and 2. There are several possible explanations for the reduced injection yield. The first of these is excited state quenching due to aggregation as mentioned previously. A second source of reduced injection efficiency may also arise from the high loading level in sample 3 in a manner similar to that of the C343/SnO_2 high coverage sample presented in the previous section. At sufficiently high coverage even under low excitation powers, the C343 excited state may be deactivated by both aggregation and excited state quenching resulting from intermolecular proximity when not preferentially ordered on the surface.

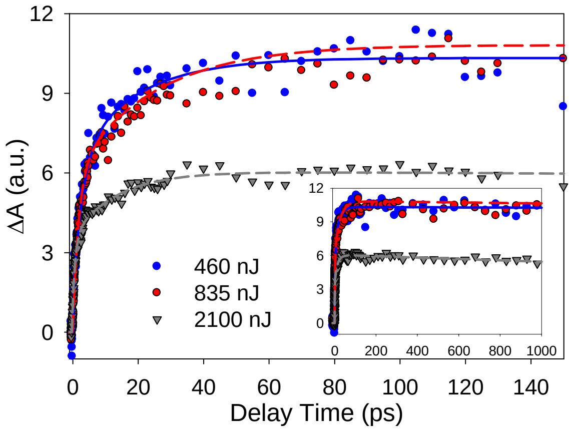

Figure 4.11. Transient IR absorption kinetics of C343/ZnO (0.09 OD) at different excitation densities of 1502, 2727 and 6857 μJ/cm^2 (shown as 460, 835 and 2100 nJ/pulse). Signal sizes have been scaled by the corresponding pump powers in order to compare the relative injection yield. The inset indicates signal at later time delay.

4.2.4.2 Transient IR measurement and excitation power dependence.

The transient electron absorption kinetics of a sample of C343/ZnO (peak absorbance 0.12 OD at 400 nm) pumped at three different excitation densities at 400 nm (1502, 2727 and 6857 μJ/cm^2, represented as 460, 835 and 2100 nJ/pulse for samples 1, 2 and 3, respectively) are shown in Figure 4.11. The transient absorptions for each sample have been normalized to correspond to the excitation densities used, in order to reflect the relative injection yields. At the two lowest pump powers, the injection kinetics of the electron in ZnO are nearly identical, with relative yields invariant to the number of excitation photons. This indicates that at these lower pump powers, quenching between nearby excited C343 dyes is negligible at this coverage level. The highest pump power sample shows similar injection kinetics, but has an injection yield ~40% lower than the samples under lower power irradiation. This lower yield, as well as the absence of a slower injection component observed in samples 1 and 2, indicates that much in the same way as the SnO_2 and TiO_2 samples, high excitation flux is sufficient to induce intermolecular energy transfer even between neighboring molecules not close enough to form ordered complexes.

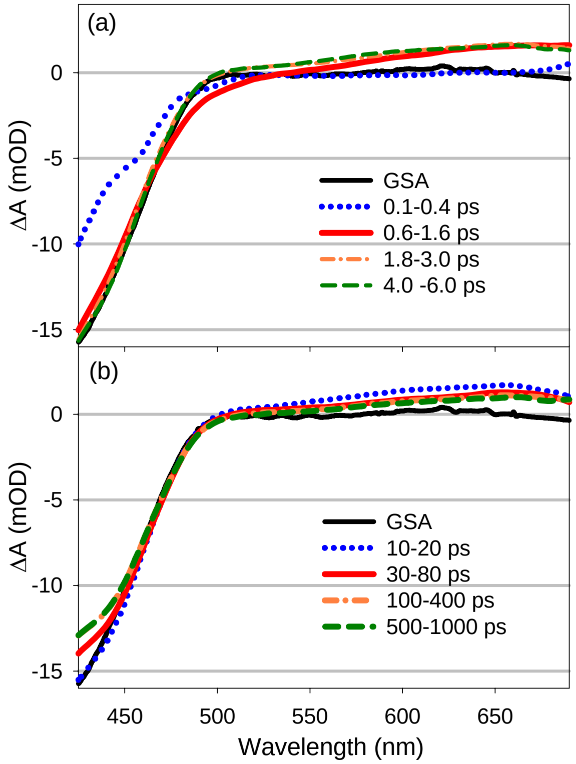

Figure 4.12. Transient visible absorption spectra of C343/ZnO at delay times (a) 0.1 to 6 ps and (b) 10 to 1000 ps after 400 nm excitation. The spectra have been averaged within the indicated time window to reduce sample-induced noise. The ground state absorption (GSA, thick black line) has been inverted and scaled for a better comparison with the corresponding bleach. The legends indicate the delay time for each spectrum in picoseconds. At early time delays (a), the spectra show both the instantaneous bleach of ground state C343 at 420 nm and instantaneous formation of a broad charge-transfer exciplex absorption at 630 nm with negligible stimulated emission corresponding to

excited C343. At later delay times (b) after 10 ps, the spectra show the decay of exciplex absorption leaving C343 cation-like absorption at 630 nm, indicating electron transfer from C343 to ZnO. The presence of C343 ground state bleach indicates recombination of injected electrons with oxidized C343 beyond the timescale of our measurements.

4.2.4.3 Transient visible spectra of C343/ZnO.

The transient visible absorption spectra of C343/ZnO are shown in Figure 4.12. The spectra are reproduced courtesy of Ye Yang.[50] In an independent study performed, he noted that different batches of ZnO films prepared resulted in populations of unbound C343 contributing to the transient absorption spectra observed, where stimulated emission was reproducibly observed at longer delay times that was not associated with the electron transfer process, and took steps to carefully control this variable in his studies of C343 adsorbed on ZnO. At early delay time (~5 ps) as shown in Figure 4.12a, the spectrum consists of the ground state bleach of C343 at 420 nm, and absorption of an ionic charge-transfer exciplex formed between excited C343 and ZnO in the region of the oxidized C343 absorption. The amplitude of stimulated emission at 500 nm is small even at the earliest delay time and decays completely by 2 ps, which suggests fast quenching of C343 excited state that is consistent with the absorption of the charge-transfer exciplex that forms instantaneously. At later time delays, shown in Figure 4.12b, the absorption at 630 nm assigned to the C343-ZnO exciplex decays, the mechanism of which will be discussed later, resulting in what we assign as pure C343 cation absorption at 630 nm after several hundred picoseconds. Simultaneously, at time delays corresponding to the decay of the cation-like exciplex absorption, the ground state bleach begins to recover as a result of exciplex dissociation. There is a ~25% decay in amplitude for the ground state bleach at 420 nm at delay times from 150 ps to 1 ns compared to the ~60% decay of the cation absorption, indicating that there may be different extinction coefficients between the exciplex and cation states of C343. The long-lived recovery of the C343 ground state bleach, however, indicates that recombination of the electron from bulk ZnO to oxidized C343 is on a timescale longer than the course of our measurements.

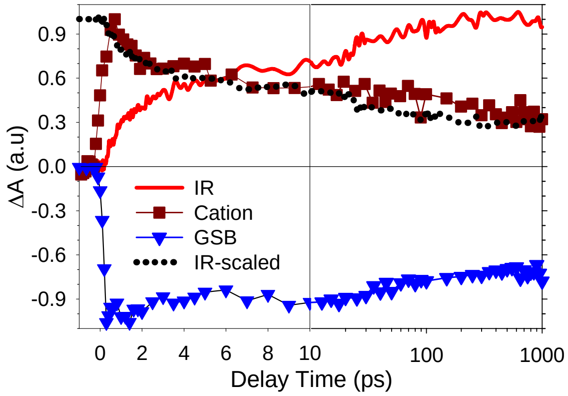

Figure 4.13. Comparison of early-time dynamics of mid-IR electron absorption in ZnO (red solid line) and C343-ZnO cation-like exciplex absorption (brown squares) with the C343 ground state bleach recovery (blue triangles). The mid-IR signal has also been inverted and scaled for better comparison with the decay of the cation-like absorption (black dotted line). The signal from exciplex absorption has been averaged over 610-650 nm to increase signal-to-noise, and scaled to provide better comparison with the IR injection dynamics. The good agreement suggests the process of electron injection through an exciplex intermediate. The right window shows a comparison of late-time dynamics of the transient species. The signals from C343 GSB and cation absorption have been scaled accordingly for comparison with the IR absorption. The good

agreement in kinetics between the two species indicates that recombination of the injected electron with C343 is slower than the timescale of our measurements.

4.2.4.4 Comparison of IR absorption and visible spectral signatures.

In Figure 4.13, we compare the dynamics of mid-IR electron absorption with the observed visible kinetics at different wavelengths. The figure is reproduced from the careful transient absorption study of C343 on ZnO done by Ye Yang as shown in Figure 4.12.[50] Due to the larger ZnO particle size and sensitivity of the transient visible measurements to both surface coverage and homogeneity, the ZnO film introduced significant fluctuations in the observed signal compared to the other films. At 630 nm (brown squares), we show the instantaneous formation and decay of the absorption we have assigned to the ionic-type exciplex formed between C343 and ZnO, scaled for comparison with the mid-IR electron absorption signal. The electron absorption is shown scaled for comparison with its overall growth (solid red line) and inverted and scaled for comparison to the decay of the cation-like absorption at 630 nm (black dotted line). It is obvious that the decay of this exciplex absorption correlates well with the rise in observed electron signal in ZnO over tens of picoseconds, suggesting that dissociation of the charge-transfer complex to form oxidized C343 and ZnO conduction band electrons is the dominating pathway for injection rather than direct excited-state electron transfer. At later time delay, as shown in the right panel of Figure 4.13, the mid-IR electron absorption is compared with the ground state bleach kinetics of C343 at 420 nm (blue triangles) and cation absorption at 630 nm. We see that the ground state bleach recovers by ~25%, while the absorption corresponding to oxidized C343 absorption decays by ~60%. This may indicate different extinction coefficients for the C343 cation in the exciplex state and the fully charge-separated state and/or an additional decay pathway of the cation feature that does not lead to the reformation of ground state. This is supported by the long-lived mid-IR electron absorption in ZnO that exhibits negligible decay up to 1 ns, indicating that recombination from ZnO to oxidized C343 is negligible within the time delays probed.

4.2.5. Comparison of mid-IR electron absorption kinetics from C343 to TiO_2, SnO_2 and ZnO films.

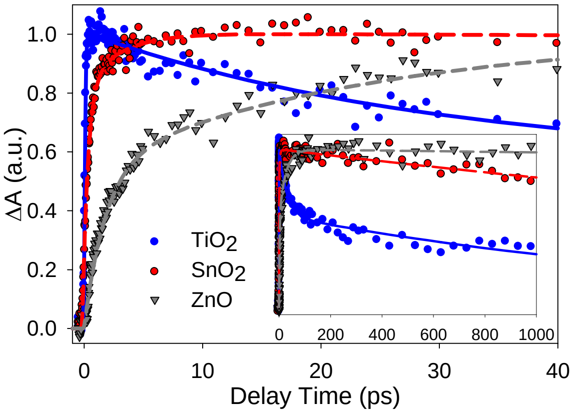

Figure 4.14. IR electron absorption kinetics traces of C343 on TiO_2, SnO_2 and ZnO films averaged over multiple trials. All kinetic traces have been normalized to maximum amplitude for better comparison. The inset shows kinetics up to 1000 ps.

Shown in Figure 4.14 are the averaged IR absorption kinetics for C343 on TiO_2, SnO_2 and ZnO films. The traces are normalized to maximum amplitude for better comparison. They were obtained by averaging the multiple trials for each sample completed at both low excitation power and dye coverage as described in the previous sections. Under these conditions, both aggregation of C343 and excitation of neighboring dye molecules on the semiconductor surfaces are understood to be negligible. With this assumption, we find that the injection rates for the three semiconductors follow the trend of TiO_2> SnO_2 >> ZnO.

In order to numerically quantify the rates, we adopt a method used in previous work. The injection kinetics for the three semiconductors are well fit by a minimum of two exponential rise functions, where the amplitudes of each rise component and their associated time constants are summarized in Table 4.1. To make a relative comparison of injection times for each semiconductor with a single quantity, the effective weighted injection timescale τ_{eff} has also been shown in Table 4.1. For each semiconductor, τ_{eff} is calculated as:

$$\tau_{eff} = \frac{A_1\tau_1 + A_2\tau_2}{A_1 + A_2} \tag{4.2}$$

The weighted electron injection times for C343 to TiO_2, SnO_2 and ZnO are <150 fs, .94 and 12.1 ps, respectively, as shown in Table 4.1. These rates describe injection of the electron from excited C343 to the bulk semiconductor conduction band, as our results described previously indicate different coupling-dependent pathways through which injection is mediated based on C343-semiconductor interactions. The results we observe for instrument-response limited injection time from C343 to TiO_2 are consistent with previous studies performed by other groups demonstrating electron injection from C343 to colloidal TiO_2 nanocrystals.[19,39,41,47,49] To our knowledge, detailed investigations of electron transfer from C343 to SnO_2 have not been reported. However, in similar studies of electron transfer from organic dyes to SnO_2 nanocrystals, injection times were reported on the order of our observations for C343.[51,52] Injection from C343 to ZnO is consistent with a previously-studied C343 derivative in which exciplex-mediated charge dissociation was observed and characterized.[53]

The decays in electron absorption signal in the TiO_2 and SnO_2 nanocrystalline films are assigned to different processes. We have shown in a comparison of the visible and mid-IR transient absorption results that while the decay in mid-IR absorption is a result of conduction band electron relaxation in TiO_2, the decay observed in the C343-SnO_2 film is a direct result of ground-state C343 regeneration as the electron recombines with the oxidized dye. In the C343-ZnO system, the negligible decay of electron absorption at later time is difficult to quantify, suggesting that the reverse electron transfer process takes place over a timescale much longer than the course of our measurements. We have unambiguously demonstrated the forward injection process, however, through the mid-IR electron absorption rise time. Recombination dynamics from the various semiconductors are outside of the scope of this investigation, although their importance is of significant interest for future studies.

Table 4.1. Fitting parameters for C343/semiconductor film mid-IR injection kinetics averaged over multiple trials.

	A_1	τ_1 (ps)	A_2	τ_2 (ps)	τ_{eff} (ps)
TiO_2	1	< .150			< .150
SnO_2	0.81	0.45	0.19	3.0	0.94
ZnO	0.55	1.8	0.45	24.7	12.1

4.3. Discussion

It has been previously demonstrated that the observed rate dependence on accepting semiconductor, where TiO_2>SnO_2>>ZnO, is observed for many dye/semiconductor systems. Energetically, the excited state redox potential of C343 lies at –1.1 eV.[54] The conduction band edges of TiO_2, SnO_2, and ZnO at pH 7 are reported as -0.57, -0.05 , and -0.57 eV (vs NHE ref.)[4,55] respectively. Sufficient driving force is present in the case of all three semiconductors for electron transfer to occur to C343; however, the small variance in energetics of the three semiconductor systems relative to the excited state redox potential of C343 is most likely not the significant factor influencing the orders-of-magnitude difference in relative injection rates for the three semiconductors. It is useful to consider all possible aspects of electron transfer rate determination in order to compare the differences in the three semiconductors. Adopting an approach similar to that of Marcus and coworkers, the total electron transfer rate from adsorbate to semiconductor can be expressed as:

$$k_{ET} = \frac{2\pi}{\hbar}\int_0^\infty dE\rho(E)\left|\bar{H}(E)\right|^2 \frac{1}{\sqrt{4\pi\lambda k_B T}}\exp[-\frac{(\lambda + \Delta G_0 - E)^2}{4\lambda k_B T}] \qquad (4.3)$$

where $\rho(E)$: density of states at energy E; $\boldsymbol{H}(E)$: the average electronic coupling matrix elements between the adsorbate excited state and accepting states in the semiconductor conduction band at energy E; λ: the reorganization energy; $\Delta G_0 = E_{cb}-E_{ox}$: the redox potential difference between the conduction band edge and the excited state of the adsorbed dye.

It has been theorized that the electronic structure of the different semiconductor conduction bands is a major contributor to variation in injection rate regardless of band-edge injection potential.[17,19,56] The conduction band of TiO_2 is composed mainly of empty d orbitals of Ti^{4+}, while the conduction bands of SnO_2 and ZnO consist of empty s and p orbitals of Sn^{4+} and Zn^{2+} respectively, with s-type character dominating.[57] The TiO_2 d-band character is thought to allow for greater electronic coupling between the accepting conduction band states and the injecting state of C343, in this case the π^* molecular orbital conjugated though the salicylate anchoring group.[46] In addition, d-bands have densities of states orders of magnitude larger than sp-bands, which when combined with greatly increased coupling to the organic dyes, provides justification into the observed sub-150 fs injection rate to TiO_2.[57,58] Although both SnO_2 and ZnO have s-type conduction bands, it does not fully explain why injection from adsorbates to SnO_2 is consistently faster than injection to ZnO. The conduction band edge of SnO_2 is ~0.5 eV lower than that of ZnO, which may play a significant role in the observed injection rate dependence in offering a higher density of states to accept the injecting electron.

In addition to the conduction band electronic character of the accepting semiconductor, the observed results suggest that exciplex formation at the boundary layer between donor and acceptor are influencing the C343 injection rate to ZnO, which may help explain the slower electron diffusion rate into the bulk ZnO nanocrystals. In the transient visible results of C343 on ZnO, we observe that charge transfer across the dye-semiconductor interface is instantaneous. This instantaneous charge separation is indicated by the formation of a broad cation-like absorption at 650 nm, which indicates that a meta-stable intermediate exciplex is formed, consisting of a surface-bound dye-semiconductor state in which the electron is already separated across the interfacial layer, possessing character associated with the oxidized form of C343. As indicated in Equation 4.1, which shows the various pathways for charge separation to occur, the dissociation of this ionic-type exciplex mediates the overall rate of electron transfer. We have demonstrated in our comparison of the mid-IR electron absorption in bulk ZnO with the decay of the exciplex absorption that dissociation of the intermediate is directly correlated with detection of conduction band electrons, indicating that the exciplex dissociates with a time constant of ~12 ps, determining the rate of overall electron transfer to ZnO. These results are supported by similar studies performed on ZnO with a variety of adsorbates. The results of a recent study by Furube et al indicated that multiple pathways were available for exciplex formation based on the energetic stability of the intermediate, which were subsequently called neutral and ionic exciplexes, depending on the adsorbate and semiconductor states participating in the stabilized intermediate.[53] The presence of an absorption corresponding to the cationic bound state of C343 in combination with the lack of any stimulated emission that might indicate the formation of a neutral-type exciplex supports our observation that charge separation across the interfacial layer is instantaneous resulting in the ionic-type exciplex.[53] It is possible that the fast quenching of stimulated emission we observe at very early time delays corresponds to multiple exciplex species, but due to the limited signal to noise and probe spectral region in our experiment, as well as the overlap of the various spectral features, we are unable to make a clear determination of other species at this time.

It is interesting to note that long-lived exciplex states are only observed between C343 and ZnO, in that electron transfer to TiO_2 and SnO2 exhibits instantaneous dissociation of any intermediate leading to a charge separation model described by the excited state deactivation of C343 to form oxidized C343 and conduction band electrons. This is consistent with the results of another study performed by our group on a series of oligoene dyes to these three semiconductors.[52] The conditions under which exciplex stabilization is optimized are still under investigation, however there have been several theories proposed in order to explain why they exhibit persistence on ZnO. In order for an exciplex to exhibit an observable lifetime before it dissociates into the fully charge separated state, it is required to be stabilized by a surface interaction with states not directly associated with the bulk conduction band character of ZnO. In the explanation put forth by Furube et al, the surface states of ZnO that contribute to trap formation below the conduction band edge couple strongly to the partially charge-separated state associated with an ionic exciplex.[53] This results in an exciplex dissociation determined by the extent of the coupling integral between the trap states and the exciplex, which has been observed in the past with other systems.[23] However, the conduction band of ZnO, at -0.57 V vs. NHE at pH 7, is ~0.5 V below the excited state redox potential of C343 (-1.1 V vs. NHE). In the mechanism proposed by Furube et al, the lowering of the exciplex energy with respect to the conduction band would most likely still result in coupling to states well above the conduction band edge of ZnO. We observe a time constant for exciplex dissociation of ~12 ps and an electron injection yield of near unity, which would indicate that the states involved in diffusion of the electron into bulk ZnO are well above the conduction band edge. It has been shown in previous experiments that coupling to trap states results in a significant population of separated charges recombining with the oxidized adsorbate,[36,59,60] which we do not significantly observe in our C343 results.

In an additional explanation put forth by our group, we explain the results based on the dielectric properties of the accepting semiconductor and the chemical interactions between C343 and the interfacial semiconductor layer. First, the dielectric constants of ZnO, SnO_2 and TiO_2 are reported as 8.5, 12.5 and 112, respectively.[59] The Coulomb interaction energy is inversely proportional to the dielectric constant, which upon photoexcitation of C343 and formation of a charge-separated exciplex determines the amount of charge shielding influencing the stability of exciplex lifetime. The smaller dielectric constant of ZnO allows for a greater interaction of the charge-separated states. In addition, it is known that ZnO exhibits Zn^{4+} surface resonances above the conduction band edge, which when combined with the strong C343 salicylate anchoring group binding can be stabilized, further weakening the coupling between the bulk ZnO conduction states and the localized surface acceptor states.[60] The salicylate anchoring group has been shown to provide an additional interaction, in that it interacts strongly with metal oxide groups. Its acidic character due to deprotonation upon solvation for semiconductor sensitization has the ability to dissolve Zn^{4+} ions from the surface of ZnO, demonstrated by previously published results.[17,49,61] While not observable in the results of this study, similar studies of exciplex formation on ZnO with salicylate anchoring groups would seem to support this explanation. It is of note that in molecules with sufficient steric hindrance, such as Rhodamine B and Fluorescein 548, we do not observe exciplex intermediate formation, possibly due to a weaker interaction with the ZnO surface than the smaller molecules with which we see evidence of charge transfer intermediates.[51,62]

4.4. Summary

The electron transfer kinetics from C343 to TiO_2, SnO_2 and ZnO have been compared in an effort to probe the role of exciplex intermediates. The kinetics of the decay of C343 excited state and/or the formation of oxidized C343 are measured by transient visible absorption spectroscopy to probe the rate of charge separation across the interface to form exciplexes. The dissociation of exciplexes to form free electrons in semiconductors is probed by growth of the free carrier absorption in the mid-IR, and compared with results measured in the visible region. For C343 on TiO_2 and SnO_2, the rate of the overall electron transfer process is determined by the rate of initial charge separation across the interface to form the exciplex, which dissociates with negligible lifetime. The charge separation rate to TiO_2 is instrument response function limited (< 150 fs). The injection rate to SnO_2 is ~1 ps, which is significantly slower than that to TiO_2. The trend of ET rate to these oxides from C343 is similar to that from N3 and is attributed to the higher density of conduction band states in TiO_2 than in SnO_2. For C343 on ZnO, the initial charge separation across the interface is also instrument response time limited (< 150 fs), but the exciplex dissociates in ~ 12 ps. In this case, the overall electron transfer process is determined by the rate of electron escape from the interface bound intermediate to the conduction band states. In comparison with previous reports of N3 and Rhodamine B on ZnO, our results show that the role of exciplexes depends on the nature of both the semiconductor and the adsorbate.

References

(1) Miller, R. J. D.; McLendon, G. L.; Nozik, A. J.; Schmickler, W.; Willig, F. *Surface electron transfer processes*; VCH publishers, Inc., 1995.

(2) O'Regan, B.; Gratzel, M. *Nature* **1991**, *353*, 737.

(3) Kamat, P. V. *Chem. Rev.* **1993**, *93*, 267.

(4) Hagfeldt, A.; Gratzel, M. *Chem. Rev.* **1995**, *95*, 49.

(5) Ellingson, R. J.; Asbury, J. B.; Ferrere, S.; Ghosh, H. N.; Sprague, J. R.; Lian, T.; Nozik, A. J. *Z. Phys. Chem. (Muenchen)* **1999**, *212*, 77.

(6) Ellingson, R. J.; Asbury, J. B.; Ferrere, S.; Ghosh, H. N.; Sprague, J. R.; Lian, T.; Nozik, A. J. *J. Phys. Chem. B* **1998**, *102*, 6455.

(7) Tachibana, Y.; Haque, S. A.; Mercer, I. P.; Durrant, J. R.; Klug, D. R. *J. Phys. Chem. B* **2000**, *104*, 1198.

(8) Tachibana, Y.; Moser, J. E.; Graetzel, M.; Klug, D. R.; Durrant, J. R. *J. Phys. Chem.* **1996**, *100*, 20056.

(9) Kuciauskas, D.; Monat, J. E.; Villahermosa, R.; Gray, H. B.; Lewis, N. S.; McCusker, J. K. *J. Phys. Chem. B* **2002**, *106*, 9347.

(10) Hannappel, T.; Burfeindt, B.; Storck, W.; Willig, F. *J. Phys. Chem. B* **1997**, *101*, 6799.

(11) Kallioinen, J.; Benko, G.; Sundstrom, V.; Korppi-Tommola, J. E. I.; Yartsev, A. P. *J. Phys. Chem. B* **2002**, *106*, 4396.

(12) Benko, G.; Kallioinen, J.; Korppi-Tommola, J. E. I.; Yartsev, A. P.; Sundstrom, V. *J. Am. Chem. Soc.* **2002**, *124*, 489.

(13) Heimer, T. A.; Heilweil, E. J.; Bignozzi, C. A.; Meyer, G. J. *J. Phys. Chem. A* **2000**, *104*, 4256.

(14) Haque, S. A.; Tachibana, Y.; Willis, R. L.; Moser, J. E.; Graetzel, M.; Klug, D. R.; Durrant, J. R. *J. Phys. Chem. B* **2000**, *104*, 538.

(15) Asbury, J. B.; Ellingson, R. J.; Ghosh, H. N.; Ferrere, S.; Nozik, A. J.; Lian, T. *J. Phys. Chem. B* **1999**, *103*, 3110.

(16) Stergiopoulos, T.; Arabatzis, I. M.; Cachet, H.; Falaras, P. *J. Photochem. Photobiol., A* **2003**, *155*, 163.

(17) Anderson, N. A.; Ai, X.; Lian, T. *J. Phys, Chem. B* **2003**, *107*, 14414.

(18) Ai, X.; Anderson, N. A.; Guo, J.; Lian, T. *J. Phys. Chem. B* **2005**, *109*, 7088.

(19) Asbury, J. B.; Hao, E.; Wang, Y.; Ghosh, H. N.; Lian, T. *J. Phys. Chem. B* **2001**, *105*, 4545.

(20) Ottolenghi, M. *Accounts Chem. Res.* **1973**, *6*, 153.

(21) Ueda, T.; Fujisawa, R.; Fukumura, H.; Itaya, A.; Masuhara, H. *J. Phys. Chem.* **1995**, *99*, 3629.

(22) Tahara, T.; Hamaguchi, H. *J. Phys. Chem.* **1992**, *96*, 8252.

(23) Furube, A.; Katoh, R.; Hara, K.; Murata, S.; Arakawa, H.; Tachiya, M. *J. Phys. Chem. B* **2003**, *107*, 4162.

(24) Furube, A.; Murai, M.; Watanabe, S.; Hara, K.; Katoh, R.; Tachiya, M. *J. Photochem. Photobiol., A* **2006**, *182*, 273.

(25) Furube, A. K., Ryuzi; Yoshihara, Toshitada; Hara, Kohjiro; Murata, Shigeo; Arakawa, Hironori; Tachiya, M. *J. Phys. Chem. B.* **2004**, *108*, 12583.

(26) Szarko, J. M.; Neubauer, A.; Bartelt, A.; Socaciu-Siebert, L.; Birkner, F.; Schwarzburg, K.; Hannappel, T.; Eichberger, R. *J. Phys. Chem. C* **2008**, *112*, 10542.

(27) Ramakrishna, G.; Verma, S.; Jose, D. A.; Kumar, D. K.; Das, A.; Palit, D. K.; Ghosh, H. N. *J. Phys. Chem. B* **2006**, *110*, 9012.

(28) Furube, A.; Katoh, R.; Hara, K.; Tachiya, M. *Proc. SPIE-Int. Soc. Opt. Eng.* **2005**, *5725*, 136.

(29) Hilgendorff, M.; Sundstroem, V. *J. Phys. Chem. B* **1998**, *102*, 10505.

(30) Huang, J.; Stockwell, D.; Boulesbaa, A.; Guo, J.; Lian, T. *J. Phys. Chem. C* **2008**, *112*, 5203.

(31) Anderson, N. A.; Hao, E.; Ai, X.; Hastings, G.; Lian, T. *Physica E: Low-Dimensional Systems & Nanostructures (Amsterdam, Netherlands)* **2002**, *14*, 215.

(32) Ghosh, H. N.; Asbury, J. B.; Weng, Y.; Lian, T. *J. Phys. Chem. B* **1998**, *102*, 10208.

(33) Anderson, N. A.; Ai, X.; Chen, D.; Mohler, D. L.; Lian, T. *J. Phys. Chem. B* **2003**, *107*, 14231.

(34) Kitamura, T.; Ikeda, M.; Shigaki, K.; Inoue, T.; Anderson, N. A.; Ai, X.; Lian, T.; Yanagida, S. *Chem. Mater.* **2004**, *16*, 1806.

(35) Ramakrishna, G. G., Hirendra N. *J. Phys. Chem. A.* **2002**, *106*, 2545.

(36) Hao, E.; Anderson, N. A.; Asbury, J. B.; Lian, T. *J. Phys. Chem. B* **2002**, *106*, 10191.

(37) Morandeira, A.; Boschloo, G.; Hagfeldt, A.; Hammarstroem, L. *J. Phys. Chem. B FIELD Full Journal Title:Journal of Physical Chemistry B* **2005**, *109*, 19403.

(38) Furube, A.; Katoh, R.; Hara, K.; Sato, T.; Murata, S.; Arakawa, H.; Tachiya, M. *J. Phys. Chem. B* **2005**, *109*, 16406.

(39) Wachtveitl, J.; Huber, R.; Sporlein, S.; Moser, J. E.; Gratzel, M. In *Int. J. Photoenergy* 1999; Vol. 1, p 153.

(40) Wang, Z.-S.; Hara, K.; Danoh, Y.; Kasada, C.; Shinpo, A.; Suga, S.; Arakawa, H.; Sugihara, H. *J. Phys. Chem. B* **2005**, *109*, 3907.

(41) Ghosh, H. N.; Asbury, J. B.; Lian, T. *J. Phys. Chem. B* **1998**, *102*, 6482.

(42) Cave, R. J.; Burke, K.; Castner, E. W., Jr. *Journal of Physical Chemistry A* **2002**, *106*, 9294.

(43) Cave, R. J.; Castner, E. W., Jr. *Journal of Physical Chemistry A* **2002**, *106*, 12117.

(44) Maroncelli, M.; Fleming, G. R. *J. Chem. Phys.* **1987**, *86*, 6221.

(45) Singh, T. S.; Madhava Rao, B. S.; Mohan, H.; Mittal, J. P. *J. Photochem. Photobiol., A* **2002**, *153*, 163.

(46) Rehm, J. M.; McLendon, G. L.; Nagasawa, Y.; Yoshihara, K.; Moser, J.; Gratzel, M. *J. Phys. Chem.* **1996**, *100*, 9577.

(47) Ghosh, H. N. *J. Phys. Chem.* **1999**, *103,* 10382.

(48) Kondov, I.; Thoss, M.; Wang, H. *Journal of Physical Chemistry A* **2006**, *110*, 1364.

(49) Moser, J. E.; Gratzel, M. *Chem. Phys.* **1993**, *176*, 493.

(50) Stockwell, D.; Yang, Y.; Huang, J.; Anfuso-Cleary, C.; Huang, Z.; Lian, T. *J. Phys. Chem. C* **2010 (accepted)**.

(51) Huang, J.; Stockwell, D.; Boulesbaa, A.; Guo, J.; Lian, T. *J. Phys. Chem. C* **2008**, *112*, 5203.

(52) Stockwell, D.; Ai, X.; Anderson, N. A.; Kitamura, T.; Ikeda, M.; Shigaki, K.; Inoue, T.; Yanagida, S.; Lian, T. **Manuscript in preparation**.

(53) Furube, A.; Katoh, R.; Yoshihara, T.; Hara, K.; Murata, S.; Arakawa, H.; Tachiya, M. *J. Phys. Chem. C* **2004**, *108*, 12583.

(54) Murakoshi, K.; Yanagida, S.; Capel, M.; Castner, J. E. W. In *ACS Symposium Series 679*; Shalaev, V. M., Moskovits, M., Eds.; American Chemical Society: 1997, p 221.

(55) Enright, B.; Fitzmaurice, D. *J. Phys. Chem.* **1996**, *100*, 1027.

(56) Anderson, N. A.; Lian, T. *Coord. Chem. Rev.* **2004**, *248*, 1231.

(57) Henrich, V.; Cox, P. *The Surface Science of Metal Oxides*; Cambridge University Press: Cambridge, 1996.

(58) Pankove, J. I. *Optical Processes in Semiconductors*; Dover: New York, 1975.

(59) *CRC Handbook of Chemistry and Physics*; 86th ed.; Lide, D. R., Ed.; CRC press: Boca Raton, 2005.

(60) Tisdale, W. A.; Muntwiler, M.; Norris, D. J.; Aydil, E. S.; Zhu, X.-Y. *J. Phys. Chem. C* **2008**, 14682.

(61) Horiuchi, H.; Katoh, R.; Hara, K.; Yanagida, M.; Murata, S.; Arakawa, H.; Tachiya, M. *J. Phys. Chem. B* **2003**, *107*, 2570.

(62) Stockwell, D.; Huang, J.; Yang, Y.; Huang, Z.; Lian, T. **Manuscript in preparation**.

Chapter 5. Interfacial electron transfer from Oligoene Dyes to TiO_2, SnO_2 and ZnO nanocrystalline thin films

5.1 Introduction

Interfacial electron transfer between dye sensitizers and semiconductor nanoparticles has been of intense interest recently due to the wide variety of applications in which nanoparticles have proven themselves beneficial. These applications range from catalysis and bio-medical uses to light-harvesting structures, including the field of dye-sensitized solar cells (DSSCs).[1-4] The promise these DSSCs show for low-cost, high-efficiency energy substitutes makes them ideal for study as a potential replacement for the current silicon-based technologies, which are more environmentally destructive and costly to produce than DSSCs. Currently, the highest solar to electric conversion efficiencies of ~10% have been achieved in DSSCs based on Ru-(4,4'-dicarboxy-2,2'-bipyridine)$_2$(NCS)$_2$ (RuN3)-sensitized TiO_2 cells, with incident photon to current efficiencies (IPCE) near unity at absorption maxima.[2,5] The high IPCE in RuN3-based TiO_2 solar cells is attributed to ultrafast electron injection from photoexcited RuN3 to the TiO_2 conduction band, with a long-lived charge separation where the electron has a much slower rate of recombination with oxidized dye or redox mediator. As well as TiO_2, other semiconductors such as SnO_2 and ZnO have been studied in detail with RuN3 in order to investigate the effects of the accepting medium on the charge transfer mechanism. It was observed that TiO_2 showed a biphasic injection mechanism, with an ultrafast (<100 fs) charge separation component of >50% and a slower component over several picoseconds. SnO_2 and ZnO showed much smaller ultrafast components and injection was dominated by the slower component (several picoseconds or longer), attributed to the conduction band characteristics of the particular semiconductor.

In the practical application of DSSC's, however, the development of alternative light-harvesters is of significant interest. RuN3 is expensive to produce, and the available limited resources make mass production of DSSCs impractical for commercial operation. In this regard, the use of synthetic organic dyes is desirable over metal complexes due to their relatively high absorption coefficients and ease of derivative synthesis in order to control absorption properties. The requirements for these dyes in order to provide useful in DSSC application are several fold; they must be panchromatic with high absorption coefficients giving high light harvesting ability, with acceptable anchoring groups to adsorb on semiconductor surfaces giving a high quantum yield of charge transfer. Additionally, absorption must be a charge-transfer type in order to give a favorable re-reduction of the oxidized dye over sufficient cycles to provide long-term stability.

In this chapter, we present a comparison of both the time-resolved mid-infrared and visible electron transfer dynamics, and emission lifetimes of oligoene dyes adsorbed on TiO_2, SnO_2 and ZnO. The oligoene dyes were chosen based on the structural variance in the series that allowed a systematic investigation of each change in dye electronic character, and the effect on electron transfer to the semiconductors.[6] Each dye increases in conjugated ethylene spacer length, shifting the absorption band and redox energetics relative to the accepting SC, so that driving force for electron transfer is varied over ~0.5 V throughout the dye series. In addition, the number of anchoring groups of two otherwise identical dyes is changed, allowing a study of the effect on electron injection rate. The processes of interest can be represented in Equation 1 as

$$Dye - SC \xrightarrow{h\upsilon} Dye^* - SC \xrightarrow{k_{CS}} Dye^+ - SC^- \xrightarrow{k_{CR}} Dye - SC \qquad (5.1)$$

where *Dye*, *Dye** and *Dye*$^+$ represent the ground, excited and oxidized states of the oligoene sensitizers, respectively, and k_{CS} and k_{CR} are charge separation and recombination rates. Using transient mid-IR measurements, we directly measure arrival of an injected electron into the semiconductor conduction band while avoiding overlap of oligoene species in this region. Transient visible measurements allow spectral observation of oligoene-related features that would otherwise be neglected in the mid-IR region. By combining these two techniques, we show a direct relationship between the dynamics of electron injection as measured by ultrafast mid-IR measurements, and the transient donor species measured by ultrafast visible measurements.

5.2 Results

5.2.1. EtOH solution

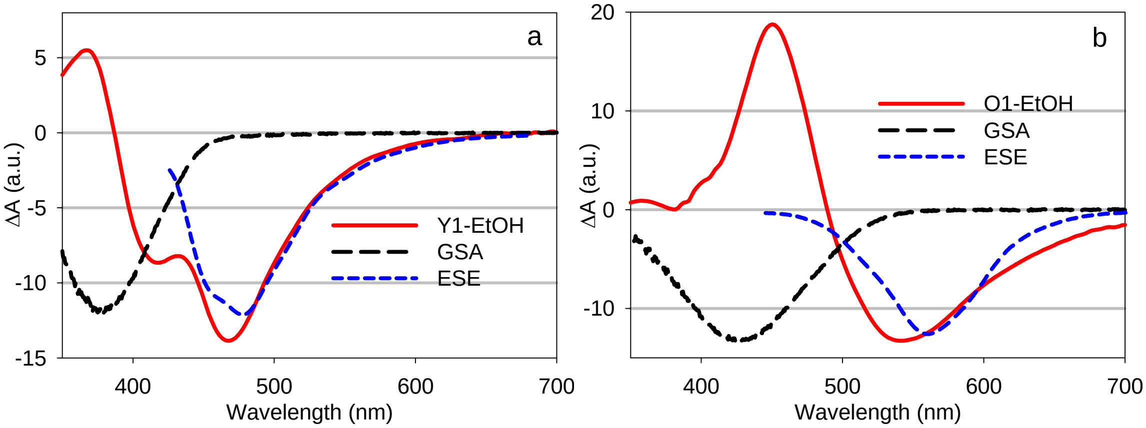

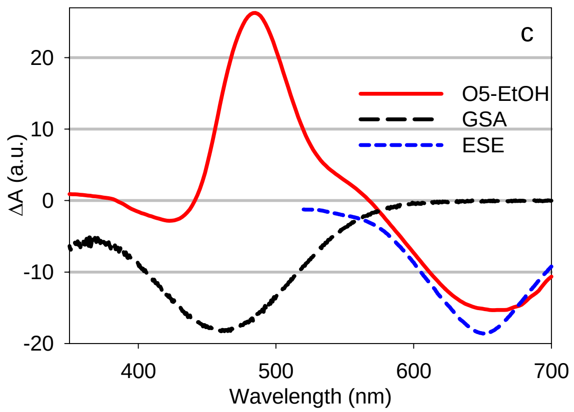

Figure 5.1. Difference spectra of (a) Y1, (b) O1 and (c) O5 in EtOH solution 5 ps after 400 nm excitation (red). Also shown are the inverted and scaled UV-visible ground state absorption (GSA) and excited state emission (ESE) spectra to compare spectral features. For each dye, the strong excited state absorption lies in the same spectral region as the ground state absorption, and stimulated emission associated with the excited state is redshifted. There are no other spectral signatures to indicate additional species outside of photoexcited dye.

In a previous study of this oligoene series, ultrafast electron transfer from dyes to TiO_2 was observed using transient mid-infrared absorption of the conduction band electrons in order to probe the charge transfer process.[6] In addition to presenting the results of this technique in other semiconductor systems, we complement the infrared measurements with transient visible signatures of the dye species themselves to better explain the observed electron absorption data. To our knowledge, no full assignments of experimentally-observed dye species other than ground state absorption and emission spectra have been made, making the investigation of such species a critical factor. In order to assign the spectral features associated with the oligoene dyes from direct photoexcitation with no charge transfer pathways, we used solutions of the dyes Y1, O1 and O5 in ethanol (EtOH). Oligene dye O2 is an analogue of O1 differing only by an additional carboxylate anchoring group, and thus we expect the electronic and spectral properties to be quite similar between the two.

Figure 5.1 shows the difference spectra of ethanolic solutions of (a) Y1, (b) O1 and (c) O5, 5 ps after photoexcitation at 400 nm with pulse energy 500 nJ. In each spectrum, the transient signal from each dye (red) is compared with the ground state absorption spectrum (GSA, black) and excited state emission spectrum (ESE, blue). The GSA and ESE spectra have been inverted and scaled for better comparison with the transient features observed for each dye. After photoexcitation of the dyes, no dominant pathway exists for electron transfer, resulting in spectral signatures of excited oligoene dyes which persist on the order of nanoseconds corresponding to expected radiative relaxation lifetimes. In Figure 5.1a, showing the spectral characteristics of dye Y1, the ground state absorption is observed to have a peak maximum at 380 nm, while the excited state emission corresponding to fluorescence is observed to peak at 478 nm. After photoexcitation, we expect the transient features observed in the difference spectrum to reflect the change in population from ground state Y1 dye to excited Y1, and the features observed are in agreement with this expectation. In pump-probe measurements, excited populations can exhibit both absorption due to further excitation to higher-lying states and stimulated emission associated with the probe-induced transition from excited to ground state. The excited state features in Figure 5.1a consist of an absorption peak observed at 365 nm and stimulated emission at 470 nm, which corresponds to the static emission spectrum. The absorption peak maximum as observed is quite close to our visible probe cutoff wavelength of 350 nm, and may not accurately reflect the real peak maximum due to insufficient probe intensity at all absorption wavelengths. However, in addition to the excited state absorption, the stimulated emission provides information about excited state population that can be unambiguously assigned to changes in the number of excited molecules. This is especially relevant as the strong excited state absorption is seen to overlap significantly with the ground state bleach, convoluting the spectrum and making characterization of Y1 excited state using this absorption complicated.

In Figure 5.1b and 5.1c, similar spectral behavior of dyes O1 and O5, respectively, are observed as was seen for Y1. Dye O1 in Figure 5.1b is observed to have a GSA peak maximum at 430 nm and ESE peak maximum at 563 nm. The transient excited state absorption of O1 is convoluted with the ground state bleach, resulting in an excited state absorption peak at 451 nm and stimulated emission at 545 nm. The ground state bleach of O1 is difficult to observe in this case due to the strong absorption of excited state, as was observed for Y1. Dye O5, as shown in Figure 5.1c, has a GSA maximum at 465 nm and ESE maximum at 652 nm. The stimulated emission observed at 660 nm correlates well with the steady-state emission, but as in dyes Y1 and O1 shown in Figure 5.1, the excited state absorption has higher oscillator strength than the ground-state absorption and convolutes the transient spectrum such that the observed GSB is negligible.

The strong excited state absorption/ground state bleach interference for these dyes suggests that in order to correlate excited state population change with charge transfer, it is convenient to use the clearly observable stimulated emission, which exhibits no overlap with species that exist from direct photoexcitation. Once charge transfer is complete, where excited state population can be considered negligible and no longer has a direct effect on transient spectra, the ground state recovery dynamics can be observed by any region of the ground stage bleach reflected by the steady-state GSA spectrum.

5.2.2. Oligoene/SnO_2

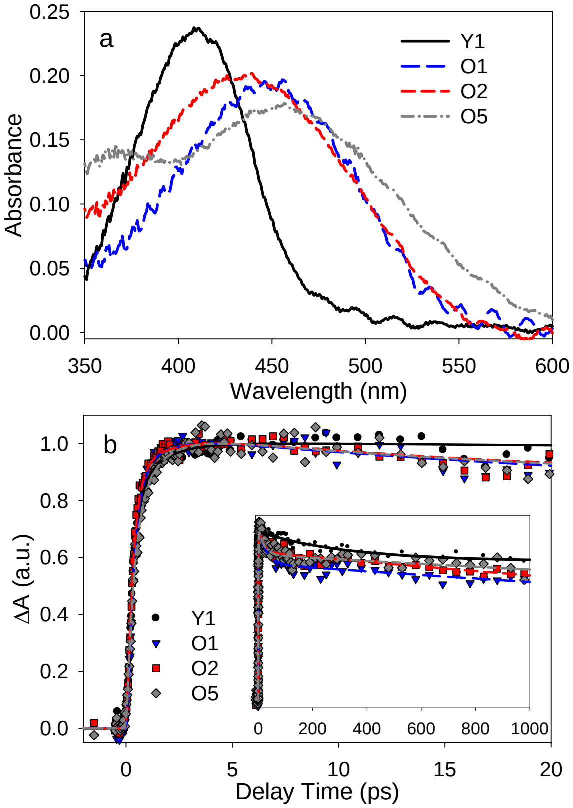

Figure 5.2. (a) UV-visible spectra of Oligoene/SnO_2 films used in transient mid-IR measurements. (b) IR transient absorption kinetic traces after 400 nm excitation. The inset shows the data extended to longer time scale. Signal sizes have been normalized to absorption maximum in order to compare injection timescales.

5.2.2.1. Transient IR measurement of electron transfer kinetics.

In similar studies by our group and others of electron transfer from organic dye systems to semiconductor nanoparticles, it has been demonstrated that several experimental conditions are limiting factors in achieving optimal electron injection efficiency. The first of these is aggregation of the adsorbate dyes on semiconductor surfaces, a phenomenon observed in organic dyes with significant structural conjugation and π-ring systems. Increasing surface coverage of these dyes leads to greater molecular order on the surface and a higher probability of intermolecular energy transfer, thus decreasing the proportion of molecules participating in electron transfer and lowering the electron transfer efficiency based on the number of absorbed photons. It was shown through systematic studies of dye loading on the nanoparticle surfaces that aggregation could be observed by loading-dependent chromatic shifting of the steady state absorption peak. The dye aggregation was subsequently controlled by eliminating the chromatic peak shift at low loading levels, and the electron transfer kinetics of these samples as measured by mid-infrared spectroscopy confirmed that aggregate formation was not a significant factor in limiting electron injection efficiency of the systems.

The second experimental consideration in dye/semiconductor systems is the effect of incident photon density on electron transfer efficiency. The probability of intermolecular energy transfer, which quenches excited molecules and decreases injection efficiency, increases with the number of excited molecules in close proximity. Even in cases where adsorbate aggregation is minimized as described previously, it is possible for neighboring molecules to become excited given sufficient photon density, leading to quenching that deactivates states otherwise involved in electron transfer to the semiconductors. The studies performed to examine this effect involved investigating the pump power dependence of electron transfer efficiency and rates from dyes to different semiconductors, demonstrating that under conditions where aggregation was minimized, sufficiently low excitation photon densities had negligible effects on electron transfer efficiencies, while higher photon densities led to significant quenching between excited adsorbate molecules and a lower overall charge transfer efficiency.

These two factors were similarly accounted for in this investigation, where a thorough study of aggregation and pump power was performed for each oligoene dye and semiconductor thin film in order to determine the optimum loading level in which aggregation was minimized. As published previously, it was observed that increasing chain length of the dyes led to greater aggregation effects at low coverage levels. Taking this under consideration, all experiments were performed under similar loading conditions for the semiconductor films that were demonstrated to exhibit minimal aggregation for all dyes. The threshold for this condition was found to be <0.25 OD for each dye, and a separate comparison of dye loading versus electron transfer efficiency (not shown) confirmed that this loading level resulted in peak efficiency values, with quenching of excited dye molecules occurring at higher surface concentration. A similar study to examine the pump power dependence on electron injection efficiency (not shown) indicated that a threshold of <450 nJ/pulse (637 $\mu J/cm^2$ excitation density) resulted in minimal quenching between neighboring dyes and no decrease in injection efficiency.

Figure 5.2a shows the UV-visible spectra for each oligoene dye on SnO_2, where the peak maxima for dyes Y1, O1, O2 and O5 were recorded as 409, 450, 437 and 458 nm, respectively. The respective transient mid-IR absorption traces for each dye are shown in Figure 5.3a. The inset shows the data extended to our 1 ns time window limit. The kinetic traces were measured at ~5000 nm probe wavelength with a pump wavelength of 400 nm. The excitation energy was 175 nJ/pulse, corresponding to an energy density of 248 μJ/cm^2. At the indicated probe wavelength, there is no transient IR absorption of the dye molecules, and the absorption profiles shown accurately reflect electron transfer from each dye to the SnO_2 conduction band. The traces have been normalized to the amplitude maximum of each dye for better comparison of differences in the injection rate. We observe that the injection dynamics for each dye to SnO_2 appear nearly identical <1 ps rise time), the possible reasons for which will be discussed in a later section.

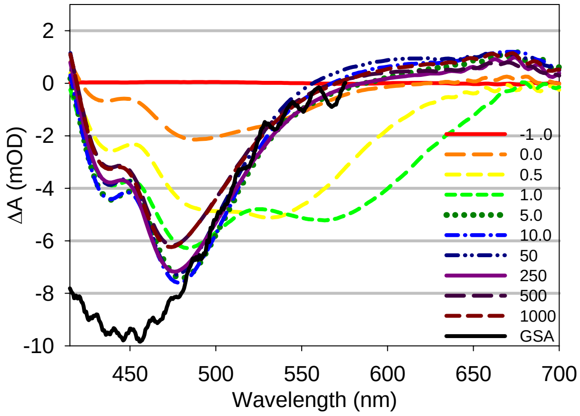

Figure 5.3. Transient visible absorption spectra of O1/SnO_2 at delay times -1.0 to 1000 ps after 400 nm excitation. The ground state absorption (GSA, thick black line) has been inverted and scaled for a better comparison with the corresponding bleach. The legends indicate the delay time for each spectrum in picoseconds. At early time delays (0-5.0 ps), the spectra show the formation and rapid decay of stimulated emission corresponding to

excited state O1 at 560 nm. The growth of O1 cation absorption from 415-470 nm is convoluted with the ground state bleach at 450 nm and excited state absorption at 451 nm. The broad, small absorption from 575-700 nm is also believed to arise from a small O1 cation contribution and extend further to the near infrared. The decay of stimulated emission is indicative of complete electron transfer from O1 to SnO_2. At later delay times (10-1000 ps), the spectra show only the decay of the O1 cation absorption convoluted with recovery of the ground state bleach at 450 nm. The recovery of pure ground state bleach from 480-550 nm can be attributed to the recombination of injected electrons with oxidized O1.

5.2.2.2. Transient visible spectra of O1/SnO_2.

In order to better understand the observed mid-IR absorption of electrons in SnO_2 and other semiconductors, we monitor the interfacial electron transfer process using transient visible spectroscopy to compare dynamic features associated with the adsorbate. As shown in section 5.1, each oligoene dye exhibits similar features upon photoexcitation, where the strong excited state absorption is heavily convoluted with the corresponding ground state bleach. The presence of stimulated emission is shown to be a more convenient and unobstructed indicator of excited state population, while the ground state bleach is expected to be the primary gauge of dye reduction dynamics once excited state is depleted due to electron transfer. With this in mind, we use oligoene dye O1 as a representative measurement of electron transfer dynamics in the visible region to both assign features associated with the electron transfer process and correlate these features with the mid-IR injection kinetics. The spectral characteristics of O1 as shown in section

5.1 are best represented within the spectral limits of our white-light probe compared to the other oligoene dyes, and we observe in separate measurements for the remaining dyes (not shown) that features associated with the electron transfer process are shifted in wavelength similarly to our EtOH solution results.

Figure 5.3 shows the transient visible spectra from 415-700 nm of oligoene dye O1 over the time range -1.0-1000 ps (sample absorbance 0.15 OD at 400 nm, with pump energy at 400 nm of 150 nJ/pulse, corresponding to 212 $\mu J/cm^2$). The spectral window shown is determined by both the absorption of the dye/semiconductor film at blue wavelengths and the scattering of the pump at 400 nm due to film inhomogeneity. The ground state absorption (GSA, black) is shown inverted and scaled to better compare the transient ground state bleach with the steady-state measurement. Immediately after excitation (0-1.0 ps), the dominant features in the transient spectra consist of the ground state bleach of O1 at 450 nm overlapped with the excited state absorption at 451 nm. In addition to these two convoluted lineshapes, we observe the stimulated emission associated with excited O1 from 550-650 nm. At later time delays after 1.0 ps, the stimulated emission is seen to decay quickly, corresponding to deactivation of excited state O1 as a result of electron transfer to SnO_2. After electron transfer is complete (within 5.0 ps), we observe an additional lineshape convoluted with the ground state bleach from 415-470 nm, which we assign to the cation radical of O1. It has been shown in calculations performed by Myllyperkio et al. of O1 on TiO_2 that this assignment is valid.[7] The depletion of excited state based on SE indicates that the absorption overlapping the GSB is not a result of long-lived excited molecules, and the appearance of a broader band extending to further blue wavelengths suggests the observed cation absorption is shifted with regards to the ESA. Also present after the disappearance of SE is a broad band with small amplitude extending into the near infrared region with an isosbestic point at ~570 nm, indicating that cation absorption may extend into the near-infrared, since at later time delay we expect only features due to oxidized O1 and the associated GSB, which matches the GSA where not convoluted by cation absorption. At delay times up to 1000 ps we see a recovery of the GSB, indicating the process of recombination of the injected electron with oxidized O1 to repopulate the ground state.

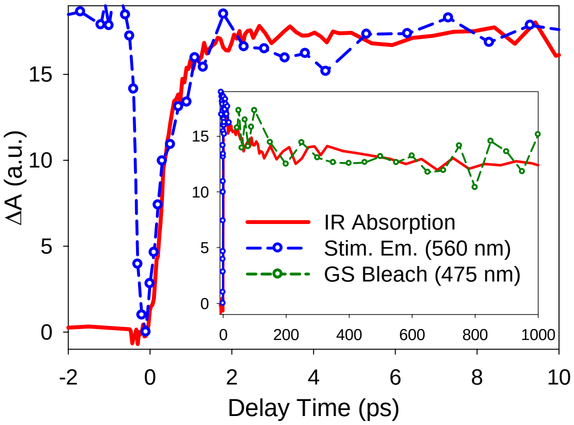

Figure 5.4. Comparison of early-time dynamics of mid-IR electron absorption in SnO_2 (red solid line) and O1 stimulated emission (SE) quenching at 560 nm (blue open circles, dashed line). The signal from SE has been averaged over 550-570 nm to increase signal-to-noise, and inverted and scaled to provide better comparison with the IR injection dynamics. The good agreement confirms the process of electron injection. Inset: comparison of late-time dynamics of mid-IR electron absorption with O1 ground state bleach at 475 nm (green open circles, dashed line). The signal from O1 GS bleach has been scaled accordingly for comparison with the IR absorption. The good agreement in

kinetics between the two signals indicates recombination of the injected electron with O1, returning oxidized molecules to the ground state.

5.2.2.3. Comparison of IR absorption and visible spectral signatures.

A comparison of the O1 transient mid-IR electron injection kinetics to SnO_2 versus transient visible kinetics of O1 excited state decay from stimulated emission are presented in Figure 5.4. The stimulated emission kinetics were obtained by averaging the transient signal for each time step from 550-570 nm in order to increase signal-to-noise ratio, where there no contributions from other signals. The SE signal decay has been inverted and scaled to the maximum of mid-IR electron absorption in order to better compare the timescale of excited state quenching with electron absorption in the SnO_2 conduction band. Clearly, the good agreement of SE decay with mid-IR electron absorption rise suggests that the decay of excited state population in O1 is a direct result of O1 oxidation through charge transfer to create conduction band electron population in SnO_2. Since the effects of aggregation have been minimized and excitation density has been determined to be below the threshold of excited state quenching through intermolecular interactions, this indicates that electron transfer from O1 to SnO_2 can be well-demonstrated by the mid-IR electron absorption, where the amplitude maximum is representative of complete injection. Due to the gross overlap of excited state and cation absorptions with the ground state bleach of O1, a similar comparison is not able to be carried out using these spectral features.

At later time delay, as shown in the inset of Figure 5.4 up to 1 ns, the decay in mid-IR electron absorption is compared with the recovery kinetics of the O1 ground state bleach. Depletion of excited state at early time delay due to the electron transfer process indicates that the only features present in the visible transient spectra are indicative of oxidized O1 and the corresponding ground state bleach. The GSB kinetics shown are averaged from 470-480 in order to demonstrate the bleach recovery in the spectral region where cation absorption is not convoluted with the GSB. The signal has been inverted and scaled for better comparison with the mid-IR absorption, which shows ~30% decay in signal amplitude up to 1 ns. The GSB recovery agrees well with the decay in electron absorption, suggesting that mid-IR decay is a clear indication of electron recombination with oxidized O1 rather than cross-section relaxation processes within the SnO_2 conduction band.

5.2.3. Oligoene/TiO_2

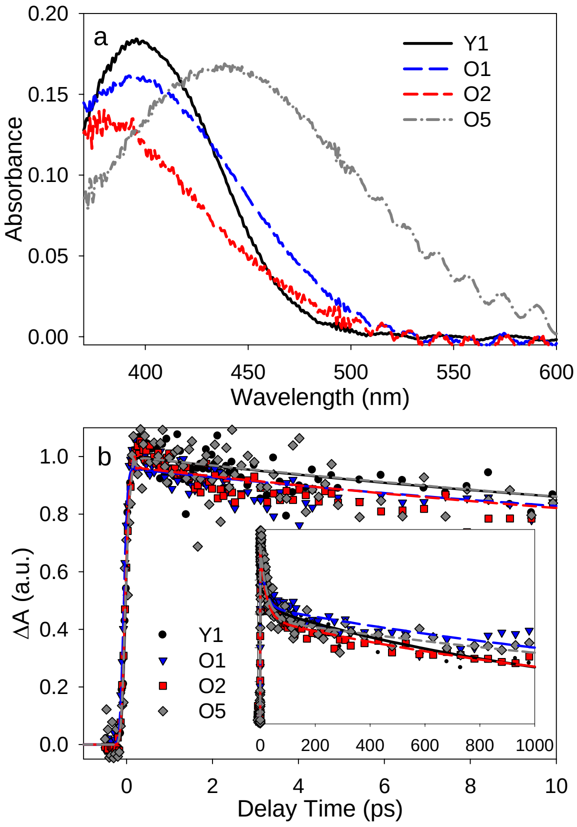

Figure 5.5. (a) UV-visible spectra of Oligoene/TiO_2 films used in transient mid-IR measurements. (b) IR transient absorption kinetic traces after 400 nm excitation. The inset shows the data extended to longer time scale. Signal sizes have been normalized to absorption maximum in order to compare injection timescales.

5.2.3.1. Transient IR measurement of electron transfer kinetics.

Figure 5.5a shows the UV-visible spectra of the oligoene dyes used in transient measurements adsorbed on nanoporous films of TiO_2, where the peak maxima for dyes Y1, O1, O2 and O5 were recorded as 397, 396, 387 and 439 nm, respectively. Studies of concentration-induced aggregation were performed on the TiO_2 films for each dye, and it was observed that under dye loading conditions where peak absorption was kept <0.2 OD, the effects of dye aggregation on UV-visible chromatic peak shift and decreased electron transfer efficiency were negligible. Under conditions in which pump excitation density was controlled to monitor injection efficiency compared to the number of incident photons, the pump power threshold at which efficiency was observed to peak was <500 nJ/pulse at 400 nm (corresponding to 707 $\mu J/cm^2$).

The transient mid-IR absorption of injected electrons in TiO_2 for each oligoene dye is shown in Figure 5.5b. The inset shows the data extended to 1 ns delay time. The kinetic traces were measured at ~5000 nm probe wavelength with a pump wavelength of 400 nm. The excitation energy was 317 nJ/pulse, corresponding to an energy density of 448 $\mu J/cm^2$. The traces have been normalized to the amplitude maximum of each dye for better comparison of differences in the injection rate. We observe that the injection dynamics for each dye to TiO_2 all exhibit an ultrafast (<150 fs) rise in electron absorption, which is faster than the instrument response limit of our pump-probe experiments. After initial ultrafast electron transfer, the mid-IR absorption signals decay in amplitude, which is explained by the transient visible measurements.

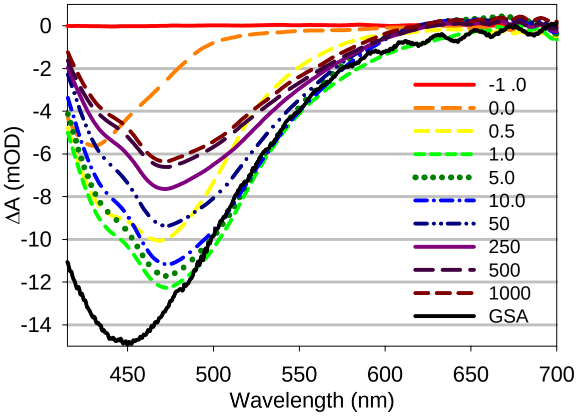

Figure 5.6. Transient visible absorption spectra of O1/TiO_2 at delay times -1.0 to 1000 ps after 400 nm excitation. The ground state absorption (GSA, thick black line) has been inverted and scaled for a better comparison with the corresponding bleach. The legends indicate the delay time for each spectrum in picoseconds. At early time delays (0-1.0 ps), stimulated emission corresponding to excited state O1 is shown to be instantaneously quenched, corresponding to sub-picosecond electron transfer. The O1 cation absorption after injection from 415-470 nm is convoluted with the ground state bleach at 450 nm. At later delay times (10-1000 ps), the spectra show only the decay of the O1 cation absorption convoluted with recovery of the ground state bleach at 450 nm. The decay of pure ground state bleach from 480-550 nm is attributed to the recombination of injected electrons with oxidized O1.

5.2.3.2. Transient visible spectra of O1/TiO$_2$.

Figure 5.6 shows the transient visible spectra from 415-700 nm of oligoene dye O1 adsorbed on nanoporous TiO$_2$ over the time range -1.0-1000 ps (sample absorbance 0.13 OD at 400 nm, with pump energy at 400 nm of 325 nJ/pulse, corresponding to 460 μJ/cm^2). The ground state absorption (GSA, black) is shown inverted and scaled to better compare the transient ground state bleach with the steady-state measurement. After initial photoexcitation, shown in the time durations 0-1.0 ps, the transient spectra consist of the ground state bleach of O1, with instantaneously quenched stimulated emission from 550-650 nm corresponding to ultrafast electron transfer to TiO$_2$. Supporting this observation is the immediate presence of absorption from oxidized O1 near 451 nm, indicated by convolution of the GSB as demonstrated in the case of O1/SnO$_2$. The observed signal size of the O1 cation absorption on TiO$_2$ is smaller in comparison with the ratio of GSB to cation on SnO$_2$. The interpretation of this observation is still unclear and is under further study to understand the possible factors influencing the cation absorption cross section. At later time delays after 1.0 ps, we observe a recovery of the GSB at 475 nm up to 1000 ps, indicating regeneration of ground state O1 due to the process of recombination from TiO$_2$, since excited state population is shown to be depleted by the absence of SE.

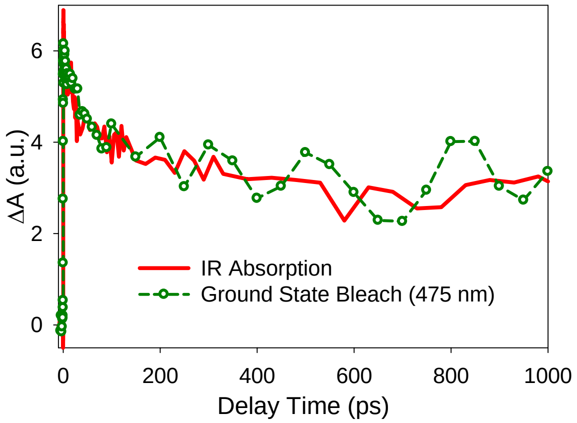

Figure 5.7. Comparison of dynamics of mid-IR electron absorption (red solid line) with O1 ground state bleach recovery at 475 nm (green circles, dashed line) up to 1 ns. The good agreement in kinetics between the two signals indicates recombination of the injected electron with O1, regenerating ground state molecules.

5.2.3.3. Comparison of IR absorption and visible spectral signatures.

Due to the ultrafast electron transfer process from O1 to TiO_2 the excited state features (SE and ESA) of O1 are instantaneously quenched, not allowing them to be compared to the rise in transient mid-IR electron absorption. However, the ultrafast deactivation of all excited state signature indicates a complete injection yield for O1 to TiO_2. Figure 5.7 shows the mid-IR electron absorption in TiO_2 (solid red line) compared to the O1 ground state bleach recovery kinetics (green circles, dashed line). The GSB kinetics shown are averaged from 470-480 in order to demonstrate the bleach recovery in the spectral region where O1 cation absorption is not convoluted with the GSB. The signal has been inverted and scaled for better comparison with the mid-IR absorption, which shows ~50% decay in signal amplitude up to 1 ns. The GSB recovery agrees well with the decay in electron absorption, suggesting that the observed decay in electron absorption is a clear indication of ground state O1 regeneration due to back electron transfer rather than cross-section decay within the TiO_2 conduction band.

5.2.4. Oligoene/ZnO

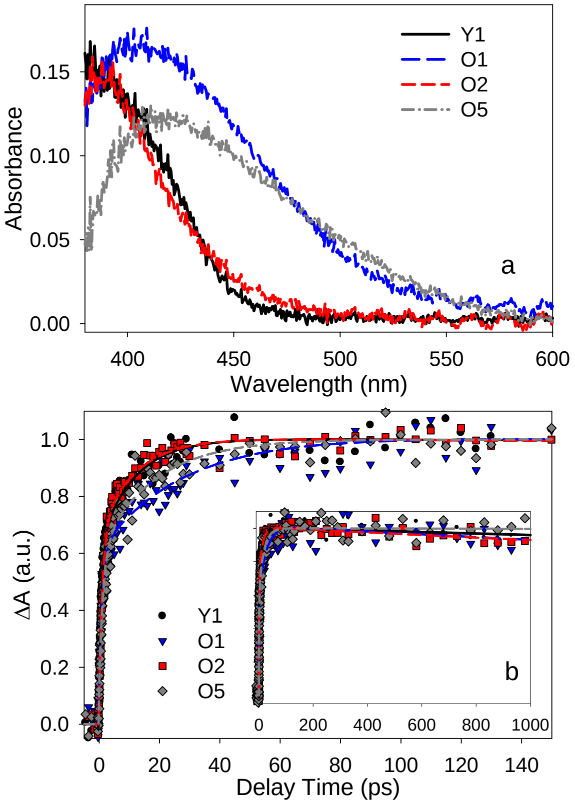

Figure 5.8. (a) UV-visible spectra of Oligoene/ZnO films used in transient mid-IR measurements. (b) IR transient absorption kinetic traces after 400 nm excitation. The inset shows the data extended to longer time scale. Signal sizes have been normalized to absorption maximum in order to compare injection timescales.

5.2.4.1. Transient IR measurement of electron transfer kinetics.

Figure 5.8a shows the UV-visible spectra of the oligoene dyes used in transient measurements adsorbed on nanoporous films of ZnO, where the peak maxima for dyes Y1, O1, O2 and O5 were recorded as 382, 406, 390 and 418 nm, respectively. Studies of concentration-induced aggregation were performed on the ZnO films for each dye, and it was observed that under dye loading conditions where peak absorption was kept <0.25 OD, the effects of dye aggregation on UV-visible chromatic peak shift and decreased electron transfer efficiency were negligible. Under conditions in which pump excitation density was controlled to monitor injection efficiency compared to the number of incident photons, the pump power threshold at which efficiency was observed to peak was <320 nJ/pulse at 400 nm (corresponding to 453 μJ/cm^2).

The transient mid-IR absorption of injected electrons in ZnO for each oligoene dye is shown in Figure 5.5b. The inset shows the data extended to 1 ns delay time. The kinetic traces were measured at ~5000 nm probe wavelength with a pump wavelength of 400 nm. The excitation energy was 180 nJ/pulse, corresponding to an energy density of 255 μJ/cm^2. The traces have been normalized to the amplitude maximum of each dye for better comparison of differences in the injection rate. We observe that the injection dynamics for each dye to ZnO exhibit rises in electron absorption on the timescale of ~40 ps, which is faster than the instrument response limit of our pump-probe experiments. After 50 ps, when electron transfer is complete, the mid-IR absorption signals do not decay in amplitude, indicating that recombination of the electron with oxidized dyes is slower than the timescale of our measurements.

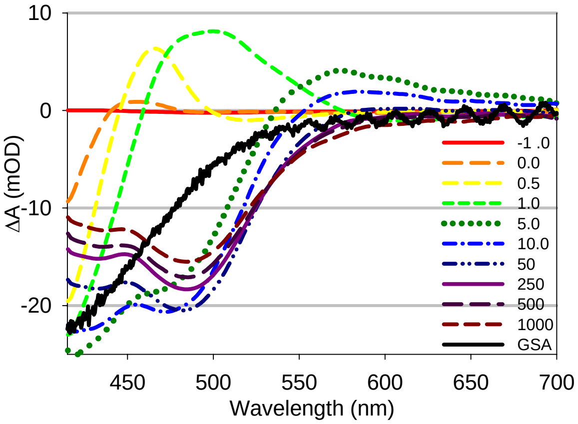

Figure 5.9. Transient visible absorption spectra of O1/ZnO at delay times -1.0 to 1000 ps after 400 nm excitation. The ground state absorption (GSA, thick black line) has been inverted and scaled for a better comparison with the corresponding bleach. The legends indicate the delay time for each spectrum in picoseconds. At early time delays (0-50.0 ps), the spectra show the instantaneous formation and ~50 ps decay of a broad charge-transfer exciplex absorption from 550-700 nm. The presence of O1 cation absorption from 415-470 nm is convoluted with the ground state bleach at 406 nm. At later delay times (100-1000 ps), the spectra show only the recovery of the ground state bleach at 450 nm convoluted with the cation absorption from 415-470 nm . The decay of the ground state bleach from 480-520 nm can be attributed to the slow recombination of injected electrons with oxidized O1.

5.2.4.2. Transient visible spectra of O1/ZnO.

The transient visible absorption spectra of O1 on ZnO are shown in Figure 5.9 (sample absorbance 0.19 OD at 400 nm, with pump energy of 225 nJ/pulse, corresponding to 318 μJ/cm^2). Directly after photoexcitation of O1 in which we see the expected GSB of O1, an instantaneous absorption forms in the region 475-650 nm, which has been assigned according to previous work by our group and others with organic dyes to an intermediate interface-bound charge-separated pair consisting of oxidized adsorbate characteristics, called a cationic exciplex.[8] This exciplex absorption decays as the intermediate dissociates into oxidized O1 and ZnO conduction band electron, as shown by the decrease in O1 cation-like absorption from 475-650 nm up to the transient spectrum corresponding to 50 ps delay time. At later delay times after 50 ps, there is a slight redshift in the GSB spectrum. In separate emission experiments we have confirmed that this redshift is not the presence of long-lived excited molecules contributing stimulated emission, and further studies are underway to explore the detailed features of the O1/ZnO transient spectra. The recovery of the O1 GSB is representative of recombination of ZnO conduction band electrons with oxidized O1 on a timescale longer than the resolution of our measurements.

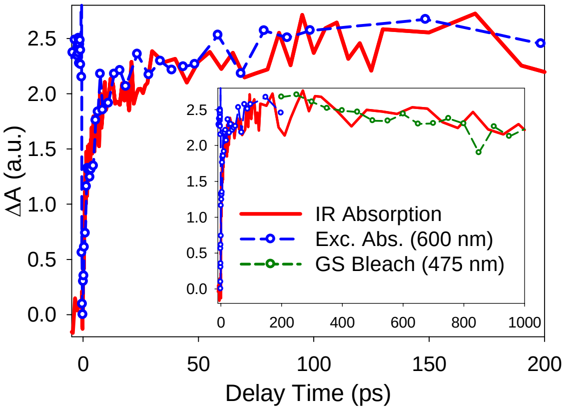

Figure 5.10. Comparison of early-time dynamics of mid-IR electron absorption in ZnO (red solid line) and O1-ZnO exciplex quenching (blue open circles, dashed line). The signal from exciplex absorption has been averaged over 590-610 nm to increase signal-to-noise, and inverted and scaled to provide better comparison with the IR injection

dynamics. The good agreement confirms the process of electron injection from an intermediate exciplex state. The inset shows a comparison of late-time dynamics of mid-IR electron absorption (solid line) with O1 ground state bleach at 475 nm (green open circles, dashed line). The signal from O1 GS bleach has been inverted and scaled accordingly for comparison with the IR absorption. The good agreement in kinetics between the two signals indicates that recombination of the injected electron with O1 is slower than the timescale of our measurements.

5.2.4.3. Comparison of IR absorption and visible spectral signatures.

The O1 transient mid-IR electron injection kinetics to ZnO versus the transient visible kinetics of O1 charge-transfer intermediate decay are presented in Figure 5.10. The kinetics of the exciplex absorption were obtained by averaging the transient signal for each time step from 590-610 nm in order to increase signal-to-noise ratio. The exciplex absorption decay has been inverted and scaled so that the maximum of mid-IR electron absorption corresponds to the absorption decay minimum in order to better compare the timescale of exciplex dissociation with electron absorption in the ZnO conduction band. The good agreement of exciplex decay with mid-IR electron absorption rise suggests that dissociation of the charge-separated intermediate is the dominant pathway for electron injection into ZnO. At later time delay up to 1 ns, as shown in the inset of Figure 5.10, the mid-IR electron absorption is compared with the recovery kinetics of the O1 ground state bleach at 475 nm. The GSB kinetics are averaged from 470-480 in order to improve signal-to-noise, and have been inverted and scaled for better comparison with the mid-IR absorption. The GSB shows a small recovery that agrees well with the slight decay in electron absorption at 1 ns, suggesting that the recombination of conduction band electrons with O1 cations is a slower process than we are able to observe on a 1 ns timescale.

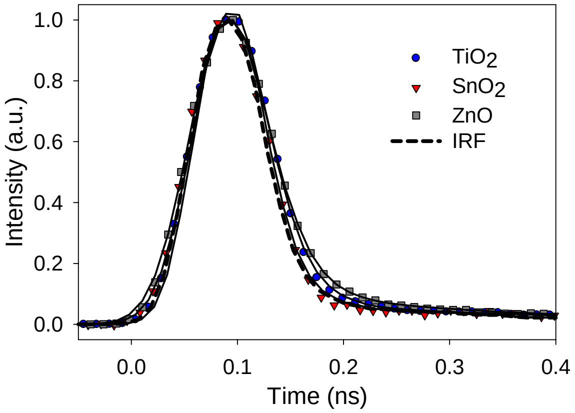

Figure 5.11. Comparison of normalized fluorescence decay measurements for O1-sensitized TiO_2 (blue circles), SnO_2 (red triangles) and ZnO (gray squares) nanoporous films. The thin solid lines are single exponential fits of the emission decays. The decay curves are compared to the instrument response function of the fluorescence measurements, showing complete excited state quenching corresponding to an injection yield of unity.

5.2.5. Emission lifetime/relative injection yield measurements.

In addition to a comparison of the transient electron and adsorbate signals in order to understand the electron transfer process from oligoene dyes to semiconductor films, we performed fluorescence lifetime experiments to examine the excited state population of the dyes as a result of photoexcitation. In dye samples on TiO_2 and SnO_2 in our femtosecond measurements, we observe complete excited state quenching on the sub-ps and ps timescales, respectively; however the transient visible spectra of ZnO are less clear. Figure 5.11 shows the normalized fluorescence lifetime decay measurements of dye O1 on films of TiO_2, SnO_2 and ZnO compared to the instrument response function. The excited state quenching for O1 on each semiconductor is clearly instrument-response limited, supporting the observations made previously in our transient measurements. An injection yield of near unity is indicated by this data in conjunction with the transient measurements, in which the ultrafast electron injection observed in TiO_2 and SnO_2 occurs as a result of charge transfer from the O1 excited state. In ZnO, where excited state population is quenched as a result of instantaneous exciplex formation, dissociation of the exciplex mediates electron diffusion into ZnO as discussed in the next section.

5.3. Discussion

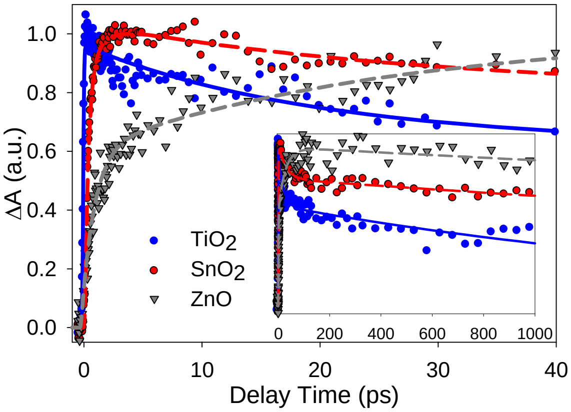

Figure 5.12. IR electron absorption kinetics traces of O1 on TiO_2, SnO_2 and ZnO films averaged over multiple trials. All kinetic traces have been normalized to maximum amplitude for better comparison. The inset shows kinetics up to 1000 ps.

Shown in Figure 5.12 are the averaged mid-IR absorption kinetics for O1 on TiO_2, SnO_2 and ZnO films for a comparison of the semiconductor-dependent injection rates. The traces are normalized to maximum amplitude for better comparison. They were obtained by averaging the multiple trials for each sample completed at both low excitation power and dye coverage as described in the previous sections. Under these conditions, both aggregation of the oligoene dyes and excitation of neighboring dye molecules on the semiconductor surfaces are understood to be negligible.[6,9-12] With this assumption, we find that the injection rates for the three semiconductors using all oligoene dyes follow the trend of $TiO_2 > SnO_2 >> ZnO$. Figure 5.12 shows only the semiconductor dependence of oligoene dye O1, but as shown in the results sections for each individual semiconductor, the trend is consistent with all other oligoene dyes.

In order to numerically quantify the rates, we adopt a method used in previous work. The injection kinetics for the three semiconductors are well fit by a minimum of two exponential rise functions, where the amplitudes of each rise component and their associated time constants are summarized in Table 5.1. To make a relative comparison of injection times for each semiconductor with a single quantity, the effective weighted injection timescale τ_{eff} has also been shown in Table 5.1. For each semiconductor, τ_{eff} is calculated as:

$$\tau_{eff} = \frac{A_1\tau_1 + A_2\tau_2}{A_1 + A_2} \tag{5.2}$$

The electron injection times for the oligoene dyes to TiO_2 are instrument-response limited, and estimated to be < 150 fs. The measured injection time is similar to those previously reported in the literature from typical sensitizer organic dyes to both colloidal TiO_2 and nanocrystalline thin films.[6,7,13-16] Electron injection times from this series of oligoene dyes to SnO_2 have not been previously reported, but the rates of electron transfer are similar to those observed from C343 and rhodamine B to SnO_2.[8,9] The electron transfer times into ZnO from the oligoene dyes are also similar to results obtained with coumarin 343 and rhodamine B, as well as the results of other groups measuring electron injection from organic dye derivatives to ZnO.[17-21]

	A_1	**τ_1 (ps)**	**A_2**	**τ_2 (ps)**	**τ_{eff} (ps)**
TiO_2					
Y1	1	< 0.150			< 0.150
O1	1	< 0.150			< 0.150
O2	1	< 0.150			< 0.150
O5	1	< 0.150			< 0.150
SnO_2					
Y1	0.78	0.28	0.22	1.31	0.50
O1	0.79	0.30	0.21	1.20	0.49
O2	0.83	0.30	0.17	1.66	0.52
O5	0.66	0.33	0.34	1.18	0.62
ZnO					
Y1	0.64	0.85	0.36	11.6	4.7
O1	0.60	1.10	0.40	27.3	11.5
O2	0.66	1.16	0.34	12.0	4.9
O5	0.56	1.37	0.44	18.0	8.8

Table 5.1. Fitting parameters for oligoene/semiconductor film mid-IR injection kinetics averaged over multiple trials.

The forward electron transfer process to TiO_2 is believed to be well-understood, where in the classic Marcus model of electron transfer theory the overall rate of charge transfer is described by

$$k_{ET} = \frac{2\pi}{\hbar}\int_0^\infty dE\rho(E)\left|\bar{H}(E)\right|^2 \frac{1}{\sqrt{4\pi\lambda k_B T}}\exp[-\frac{(\lambda+\Delta G_0 - E)^2}{4\lambda k_B T}] \qquad (5.3)$$

where $\rho(E)$: density of states at energy E; $\boldsymbol{H}(E)$: the average electronic coupling matrix elements between the adsorbate excited state and accepting states in the semiconductor conduction band at energy E; λ: the reorganization energy; $\Delta G_0 = E_{cb} - E_{ox}$: the redox potential difference between the conduction band edge and the excited state of the adsorbed dye.[22-28] Previous studies of RuN3 comparing the rate of electron injection between TiO_2 and SnO_2 have theorized that the greater density of accepting states in the TiO2 conduction band results in a much faster rate of electron transfer.[27,28] In addition, the electronic characteristics of the conduction band are suggested to have a significant effect, where the empty d orbitals of Ti^{4+} in the TiO_2 conduction band provide much greater electronic coupling to systems anchored to the semiconductor surface with π-type LUMO electronic states.[29,30] Computational studies performed on this series of oligoene dyes or close derivatives support this argument, where upon photoexcitation, promotion of an electron from the HOMO to LUMO shifts electron density away from the dimethylamine moiety into the conjugated π system that couples through the bi-dentate carboxylate anchoring group to the TiO_2 conduction band.[7,31-33]

In comparison with TiO_2, the electron injection rate from the oligoene dyes to SnO_2 is well described using the same principles, where the effective electron injection rate is on average ~ 0.55 ps. Using the same model, although the conduction band of SnO_2 is ~ 0.5 eV lower than that of TiO_2, the electron transfer rate is much slower. This is consistent with results comparing the electron transfer process between RuN3 and other organic dyes, in which the rates of charge transfer are significantly less than those to TiO_2.[8,18,27,28,34-49] It is argued that because of the lower density of accepting states in the SnO_2 conduction band compared to that of TiO_2, as well as because of the SnO_2

conduction band electronic character composed of s-type Sn^{2+}, the electron transfer rate is considerably smaller.[8,27,28] Our results indicate that the charge dissociation after forming the photoexcited donor-acceptor pair is not hindered by any long-lived intermediates in both oligoene-sensitized TiO_2 and SnO_2, which supports the prevailing model describing differences in charge transfer rate between the two semiconductors.

For the oligoene dyes on ZnO, our results in the transient visible measurements indicate that charge transfer across the dye-semiconductor interface is nearly instantaneous, as evidenced by the instrument response-limited formation of an absorption corresponding to an interface-bound exciplex. Based on the mid-infrared transient results that directly show formation of electron absorption in bulk ZnO on the timescale of picoseconds, this suggests that the dissociation of the interface-bound charge-separated exciplex to form free electrons in the ZnO conduction band is the rate-limiting step in the electron transfer process. As indicated in Table 5.1, exciplex dissociation occurs several picoseconds after initial intermediate formation. The formation and subsequent dissociation of this charge-transfer intermediate is consistent with findings in recent studies of photoexcited adsorbates on ZnO, which has been demonstrated with both organic and inorganic dyes alike.[8,18,20,50] In the findings of a recent study by Furube et al, it was proposed that the character of the charge-transfer exciplex is affected by the adsorbate donor-state coupling to the acceptor states of ZnO, which in turn gives the exciplex neutral or ionic-type spectral signatures and directly influences the rate of exciplex dissociation.[20] The absence of excited oligoene emission observed even at very early time delays, as well as the complete quenching of fluorescence in our emission studies, suggests that the intermediate exciplex formed after oligoene photoexcitation already possesses the ionic-type character associated with stabilized charge separation across the oligoene-ZnO interface. Unfortunately, we are not able to directly assign the various forms of the intermediate due to limited signal-to-noise and various spectral features that heavily convolute the spectral lineshape in the regions of interest.

In the mechanism proposed by Furube et al, formation of a cationic exciplex occurs when the excited state of the donor couples strongly to surface states of the acceptor, possibly at or near the conduction band edge.[20] However, in the case of the oligoene dyes, the excited state redox potentials are well above the ZnO conduction band edge of -0.81 V (at pH 7 vs SCE) as indicated in Figure 5.13.[4] This suggests that the acceptor states contributing to formation of the exciplex are above the conduction band edge, supported by the relatively efficient electron diffusion into bulk ZnO with a yield of near unity. Also, within the 1 ns time window probed by our transient measurements, we observe no regeneration of ground state oligoene dyes that would indicate dissociation of the exciplex intermediate in a non charge-transfer capacity. In a previous study performed on C343-sensitized ZnO, we suggested that the lower dielectric constant of ZnO (8.5) compared to that of TiO_2 (114) and SnO_2 (12.5) allowed greater stability of a long-lived intermediate exciplex, where the effect of charge-shielding is greatly diminished.[8,20,51] In addition, it is known that ZnO exhibits Zn^{4+} surface resonances above the conduction band edge, which when combined with the strong oligoene salicylate anchoring group binding can be stabilized, further weakening the coupling between the bulk ZnO conduction states and the localized surface acceptor states.[52,53] Due to this interaction, the intermediate exciplex lifetime on ZnO is much longer-lived than those on

TiO_2 and SnO_2, where interface-bound dissociation is limited to the electronic coupling between excited adsorbate donor and bulk conduction band acceptor states. It is of note that in studies of Rhodamine B and Fluorescein 548 on ZnO, we observed no such formation of an interface-bound charge separated state, which may be related to the steric hindrance of the larger xanthene molecules when binding to the semiconductor surface.[9,54,55] Exploring this consideration is of interest for future studies, but for the time being is outside the scope of this work.

5.4 Summary

The electron transfer kinetics from oligoene dyes to TiO_2, SnO_2 and ZnO have been compared in an effort to probe the role of interface-bound charge separated pair (exciplex) intermediates, as well as the dependence of accepting semiconductor on electron transfer rate. The kinetics of the deactivation of oligoene dye O1 excited state or the decay of exciplex absorptions are measured by transient visible absorption spectroscopy to probe the rate of charge separation across the interface to form intermediates. The dissociation of exciplex intermediates to form free electrons in semiconductors is probed by growth of the free carrier absorption in the mid-IR, and compared with results measured in the visible region. For the oligoene dyes on TiO_2 and SnO_2, the rate of the overall electron transfer process is determined by the rate of initial charge separation across the interface to form the exciplex, which dissociates with negligible lifetime. The charge separation rate to TiO_2 is instrument response function limited (< 150 fs). The injection rate to SnO_2 is ~ 0.5 ps, depending on the excited state redox potential of each dye, which is slower than that to TiO_2. The trend of ET rate to these oxides from the oligoene dyes is similar to that from C343 and is attributed to the higher density of conduction band states in TiO_2 than in SnO_2. For the oligoene dyes on ZnO, the initial charge separation across the interface is also instrument response time limited (< 150 fs), but the exciplex dissociates on the order of picoseconds depending on the dye. In this case, the overall electron transfer process is determined by the rate of electron escape from the interface bound exciplex intermediate to the ZnO conduction band states. In comparison with previous reports of C343 and Rhodamine B on ZnO, our results suggest that the role of exciplexes depends on the nature of both the semiconductor and the adsorbate.

References

(1) Miller, R. J. D.; McLendon, G. L.; Nozik, A. J.; Schmickler, W.; Willig, F. *Surface electron transfer processes*; VCH publishers, Inc., 1995.

(2) O'Regan, B.; Gratzel, M. *Nature* **1991**, *353*, 737.

(3) Kamat, P. V. *Chem. Rev.* **1993**, *93*, 267.

(4) Hagfeldt, A.; Gratzel, M. *Chem. Rev.* **1995**, *95*, 49.

(5) Nazeeruddin, M. K.; Kay, A.; Rodicio, I.; Humphrybaker, R.; Muller, E.; Liska, P.; Vlachopoulos, N.; Gratzel, M. *J. Am. Chem. Soc.* **1993**, *115*, 6382.

(6) Kitamura, T.; Ikeda, M.; Shigaki, K.; Inoue, T.; Anderson, N. A.; Ai, X.; Lian, T.; Yanagida, S. *Chem. Mater*. **2004**, *16*, 1806.

(7) Myllyperkio, P.; Manzoni, C.; Polli, D.; Cerullo, G.; Korppi-Tommola Jouko, E. I. *J. Phys. Chem. C* **2009**, *113*, 13985.

(8) Stockwell, D.; Yang, Y.; Huang, J.; Anfuso-Cleary, C.; Huang, Z.; Lian, T. *J. Phys. Chem. C* **2010 (accepted)**.

(9) Huang, J.; Stockwell, D.; Boulesbaa, A.; Guo, J.; Lian, T. *J. Phys. Chem. C* **2008**, *112*, 5203.

(10) Sayama, K.; Tsukagoshi, S.; Hara, K.; Ohga, Y.; Shinpou, A.; Abe, Y.; Suga, S.; Arakawa, H. *J. Phys. Chem. B* **2002**, *106*, 1363.

(11) Ruseckas, A.; Namdas, E. B.; Theander, M.; Svensson, M.; Yartsev, A.; Zigmantas, D.; Andersson, M. R.; Inganas, O.; Sundstrom, V. *J. Photochem. Photobiol., A* **2001**, *144*, 3.

(12) Khazraji, A. C.; Hotchandani, S.; Das, S.; Kamat, P. V. *J. Phys. Chem. B* **1999**, *103*, 4693.

(13) Ghosh, H. N.; Asbury, J. B.; Lian, T. *J. Phys. Chem. B* **1998**, *102*, 6482.

(14) Ferrere, S.; Zaban, A.; Gregg, B. A. *J. Phys. Chem. B* **1997**, *101*, 4490.

(15) Hara, K.; Kurashige, M.; Dan-oh, Y.; Kasada, C.; Shinpo, A.; Suga, S.; Sayama, K.; Arakawa, H. *New J. Chem.* **2003**, *27*, 783.

(16) Wachtveitl, J.; Huber, R.; Sporlein, S.; Moser, J. E.; Gratzel, M. In *Int. J. Photoenergy* 1999; Vol. 1, p 153.

(17) Huber, R.; Sporlein, S.; Moser, J. E.; Gratzel, M.; Wachtveitl, J. *J. Phys. Chem. B* **2000**, *104*, 8995.

(18) Szarko, J.; Neubauer, A.; Bartelt, A.; Socaciu-Siebert, L.; Birkner, F.; Schwarzburg, K.; Hannappel, T.; Eichberger, R. *J. Phys. Chem. C* **2008**, *112*, 10542.

(19) Yoshihara, T.; Katoh, R.; Furube, A.; Murai, M.; Tamaki, Y.; Hara, K.; Murata, S.; Arakawa, H.; Tachiya, M. *Journal of Physical Chemistry B* **2004**, *108*, 2643.

(20) Furube, A. K., Ryuzi; Yoshihara, Toshitada; Hara, Kohjiro; Murata, Shigeo; Arakawa, Hironori; Tachiya, M. *J. Phys. Chem. B.* **2004**, *108*, 12583.

(21) Murakoshi, K.; Yanagida, S.; Capel, M.; Castner, J. E. W. In *ACS Symposium Series 679*; Shalaev, V. M., Moskovits, M., Eds.; American Chemical Society: 1997, p 221.

(22) Marcus, R. A. *J. Chem. Phys.* **1965**, *43*, 679.

(23) Gao, Y. Q.; Georgievskii, Y.; Marcus, R. A. *J. Chem. Phys.* **2000**, *112*, 3358.

(24) Gao, Y. Q.; Marcus, R. A. *J. Chem. Phys.* **2000**, *113*, 6351.

(25) Gosavi, S.; Marcus, R. A. *J. Phys. Chem. B* **2000**, *104*, 2067.

(26) She, C.; Anderson, N. A.; Guo, J.; Liu, F.; Goh, W.; Chen, D.-T.; Mohler, D. L.; Tian, Z.-Q.; Hupp, J.; Lian, T. *J. Phys. Chem. B.* **2005**, *109*, 19345.

(27) Anderson, N. A.; Lian, T. *Annu. Rev. Phys. Chem.* **2005**, *56*, 491.

(28) Asbury, J. B.; Hao, E.; Wang, Y.; Ghosh, H. N.; Lian, T. *J. Phys. Chem. B* **2001**, *105*, 4545.

(29) Henrich, V.; Cox, P. *The Surface Science of Metal Oxides*; Cambridge University Press: Cambridge, 1996.

(30) Rehm, J. M.; McLendon, G. L.; Nagasawa, Y.; Yoshihara, K.; Moser, J.; Gratzel, M. *J. Phys. Chem.* **1996**, *100*, 9577.

(31) Hara, K.; Sato, T.; Katoh, R.; Furube, A.; Yoshihara, T.; Murai, M.; Kurashige, M.; Ito, S.; Shinpo, A.; Suga, S.; Arakawa, H. *Adv. Func. Mat.* **2005**, *15*, 246.

(32) Qin, P.; Yang, X.; Chen, R.; Sun, L.; Marinado, T.; Edvinsson, T.; Boschloo, G.; Hagfeldt, A. *j. Phys. Chem. C* **2007**, *111*, 1853.

(33) Hara, K.; Wang, Z.; Sato, T.; Furube, A.; Katoh, R.; Sugihara, H.; Dan-oh, Y.; Kasada, C.; Shinpo, A.; Suga, S. *J. Phys. Chem. B* **2005**, *109*, 15476.

(34) Fessenden, R. W.; Kamat, P. V. *J. Phys. Chem.* **1995**, *99*, 12902.

(35) Ellingson, R. J.; Asbury, J. B.; Ferrere, S.; Ghosh, H. N.; Sprague, J. R.; Lian, T.; Nozik, A. J. *Z. Phys. Chem. (Muenchen)* **1999**, *212*, 77.

(36) Asbury, J. B.; Ellingson, R. J.; Ghosh, H. N.; Ferrere, S.; Nozik, A. J.; Lian, T. *J. Phys. Chem. B* **1999**, *103*, 3110.

(37) Ellingson, R. J.; Asbury, J. B.; Ferrere, S.; Ghosh, H. N.; Sprague, J. R.; Lian, T.; Nozik, A. J. *J. Phys. Chem. B* **1998**, *102*, 6455.

(38) Tachibana, Y.; Haque, S. A.; Mercer, I. P.; Moser, J. E.; Klug, D. R.; Durrant, J. R. *J. Phys. Chem. B* **2001**, *105*, 7424.

(39) Tachibana, Y.; Moser, J. E.; Graetzel, M.; Klug, D. R.; Durrant, J. R. *J. Phys. Chem.* **1996**, *100*, 20056.

(40) Haque, S. A.; Tachibana, Y.; Willis, R. L.; Moser, J. E.; Graetzel, M.; Klug, D. R.; Durrant, J. R. *J. Phys. Chem. B* **2000**, *104*, 538.

(41) Hannappel, T.; Burfeindt, B.; Storck, W.; Willig, F. *J. Phys. Chem. B* **1997**, *101*, 6799.

(42) Benko, G.; Kallioinen, J.; Korppi-Tommola, J. E. I.; Yartsev, A. P.; Sundstrom, V. *J. Am. Chem. Soc.* **2002**, *124*, 489.

(43) Kallioinen, J.; Benko, G.; Sundstrom, V.; Korppi-Tommola, J. E. I.; Yartsev, A. P. *J. Phys. Chem. B* **2002**, *106*, 4396.

(44) Heimer, T. A.; Heilweil, E. J.; Bignozzi, C. A.; Meyer, G. J. *J. Phys. Chem. A* **2000**, *104*, 4256.

(45) Kuciauskas, D.; Monat, J. E.; Villahermosa, R.; Gray, H. B.; Lewis, N. S.; McCusker, J. K. *J. Phys. Chem. B* **2002**, *106*, 9347.

(46) Sayama, K.; Sugihara, H.; Arakawa, H. *Chem. Mater.* **1998**, *10*, 3825.

(47) Iwai, S.; Hara, K.; Murata, S.; Katoh, R.; Sugihara, H.; Arakawa, H. *J. Chem. Phys.* **2000**, *113*, 3366.

(48) Benko, G.; Myllyperkio, P.; Pan, J.; Yartsev, A. P.; Sundstrom, V. *J. Am. Chem. Soc* **2003**, *125*, 1118.

(49) Ai, X.; Anderson, N. A.; Guo, J.; Lian, T. *J. Phys. Chem. B* **2005**, *109*, 7088.

(50) Furube, A.; Katoh, R.; Hara, K.; Murata, S.; Arakawa, H.; Tachiya, M. *J. Phys. Chem. B* **2003**, *107*, 4162.

(51) *CRC Handbook of Chemistry and Physics*; 77th ed.; Lide, D. R., Ed.; CRC press: Boca Raton, 1996.

(52) Tisdale, W.; Muntwiler, M.; Norris, D.; Aydil, E.; Zhu, X.-Y. *J. Phys. Chem. C* **2008**, *112*, 14682.

(53) Moser, J. E.; Gratzel, M. *Chem. Phys.* **1993**, *176*, 493.

(54) Stockwell, D.; Huang, J.; Yang, Y.; Huang, Z.; Lian, T. **in preparation**.

(55) Labat, F.; Ciofini, I.; Hratchian, H.; Frisch, M.; Raghavachari, K.; Adamo, C. *J. Am. Chem. Soc.* **2009**, *131*, 14290.

Chapter 6. Interfacial electron transfer from Fluorescein 548 to SnO_2, In_2O_3 and ZnO nanocrystalline thin films

6.1 Introduction

The application of dye-sensitized solar cells (DSSC) has been a research area of intense interest, with particular focus specifically dedicated to the charge-transfer properties between photoexcited molecules and the semiconductor nanoparticles upon which they adsorb.[1-3] Currently, the highest efficiency DSSCs have been composed of TiO_2 nanocrystals, which show fast, efficient charge separation, with solar-to-electric power efficiencies of up to 10% being reported using $Ru(dcbpy)_2(NCS)_2$ [dcbpy = 2,2'-bipyridine-4,4'-dicarboxylate] (RuN3) as the light-harvesting adsorbate.[4,5] While TiO_2 has been an area of focus, other DSSC systems using semiconductors such as SnO_2,[6-8] ZnO,[6,9,10] Nb_2O_3,[6,9,11-15] and In_2O_3[6,9] have been investigated in course of gaining a better understanding of the semiconductor characteristics that positively influence DSSC efficiency and incident-photon-to-current (IPCE) yield.[6,16] Although the conversion efficiencies of DSSCs composed of these alternative semiconductors have been typically lower than that of the RuN3-sensitized TiO2 system, they have provided useful information as to the acceptor character influencing the forward and reverse electron transfer (ET) processes.

In addition to exploring the nature of the accepting semiconductor in the DSSC, of fundamental interest has also been the wide range of sensitizers available for light-harvesting capabilities and their individual properties as related to the forward ET process. Although ruthenium-based sensitizers have exhibited the highest conversion efficiencies to date, organic dyes such as perylenes,[8,17,18] coumarins,[19-30] xanthenes[31-37] and merocyanines[38-41] are alternative sensitizers being widely explored due to their low cost of production compared to transition metal complexes, large absorption cross sections due to strong π-π* or n-π* transitions and design-based wide tunability across the solar spectral region.[42] Their ease of functionalization makes them especially attractive, as slight structural modification can result in large changes in electronic character, giving insight as to details underlying the basic electron transfer process.

In recent studies of several dye series on nanocrystalline thin films, results have indicated that the interface-bound charge-separated pair (IBCSP) formed immediately after photoexcitation of the adsorbate plays a significant part on influencing the injection kinetics into the bulk semiconductor.[18,19,43-50] Although the role of this IBCSP is not well understood, the nature of its dissociation is suggested to be dependent on the coupling between the donor states formed after photoexcitation and the accepting semiconductor states that locally influence the charge-transfer intermediate.[19,51,52] It is theorized that in dye-semiconductor systems where the IBCSP can couple to localized surface states with character separate of the bulk conduction band states, electron transfer to the bulk states is hindered by the stabilized intermediate. Studies by our group using both mid-infrared and visible transient spectroscopic techniques have indicated that the IBCSP dissociation of several organic dye-sensitized ZnO films is significantly slower than that of the dyes on TiO_2, SnO_2 and In_2O_3 films.[19,53] Interestingly enough, this phenomenon was not observed in a similar study of the electron-injection kinetics from Rhodamine B (RhB) to SnO_2, In_2O_3 and ZnO films.[33] One explanation proposed was that the steric hindrance introduced by the large conjugated-ring xanthene structure did not allow significant coupling of the RhB anchoring group to the surface states of ZnO to the same degree as the smaller coumarin and oligoene dye structures in which the IBCSP dissociation was observed to mediate ET rate.

In order to further examine the possible effects of charge-transfer intermediate formation on electron transfer, it is useful to observe electron transfer in dye systems similar to RhB. A xanthene analogue, Fluorescein 548 (Fluorescein 27 / Fl) is similar in structure to RhB, and has been well-studied in charge-transfer studies to TiO2 nanocrystalline thin films.[31,37,54,55] To our knowledge, little work has been done characterizing the electron transfer properties of Fluorescein 548 to other semiconductor substrates, which makes it attractive as a comparison to the previous work by our group involving the electron injection dynamics from RhB to SnO_2, In_2O_3 and ZnO. The following presents the results of our Fl study on SnO_2, In_2O_3 and ZnO, which indicates that little to no IBCSP persistence is seen as in previous dye-ZnO studies. We also observe a difference in electron injection rates dependent on the accepting semiconductor that is consistent with previous arguments, where $SnO_2 \sim In_2O_3 > ZnO$, as seen with RhB. These differences are discussed in later sections.

6.2. Results

6.2.1. Fl/ZrO$_2$

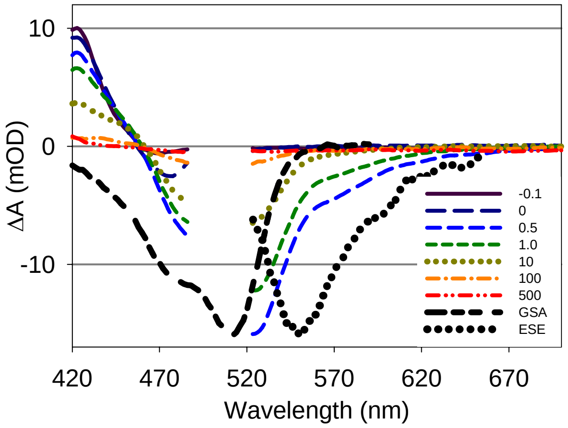

Figure 6.1. Transient visible absorption spectra of Fl/ZrO$_2$ at different delay times after excitation at 500 nm. Also plotted against the negative vertical axis for comparison are the static UV-vis absorption spectrum (thick dashed line) and fluorescence emission spectrum (thick dotted line) of Fl/ZrO$_2$. Features in the transient spectra consist of the bleach of Fl ground state absorption at 530 nm, and both stimulated emission (550-650 nm, corresponding to the emission spectrum) and absorption (423 nm) corresponding to excited Fl dye. All features are formed instantaneously and decay with identical kinetics.

In order to present a clear assignment of features associated with transient visible spectroscopy and correlate them with the electron transfer process as described previously, we first monitor the dynamics of photoexcited Fl on a nanoporous ZrO$_2$ film. The band edge of ZrO$_2$ lies at -1.9 V SCE (at pH 7), considerably more negative than the excited state oxidation potential of -0.89 V for Fl. Therefore, it is reasonable to assume that photoexcitation of the adsorbed Fl will only result in the excited state of the adsorbed dye, with no charge transfer occurring. When probing with transient visible spectroscopy, the only expected features will be associated with depopulation of the ground state and the corresponding number of newly excited molecules. No electron transfer-related features should be observed, which has been correlated with transient measurements in the mid-infrared showing negligible absorption as a result of no injection processes from the adsorbed Fl.

Figure 6.1 shows the transient visible absorption spectra of Fl/ZrO_2 at different delay times after 500 nm excitation. The deleted portion of the spectra (485-523 nm) corresponds to detection of the pump, which introduces fluctuations in the calculated values of ΔA at those wavelengths orders of magnitude greater than the observed signal. For comparison, the static UV-vis absorption and fluorescence emission spectra are also plotted along the negative vertical axis in order to make a clear assignment of observed features. The transient spectra consist of two components: the first is an increased transmission from ~465-650 nm, which contains contributions from both the bleach associated with depopulation of ground state Fl and stimulated emission of excited molecules, and the second is an increased absorption band centered at 423 nm. Both components form instantaneously and decay with identical kinetics at all wavelengths. The two-state picture of the observed results is further supported by the presence of an isosbestic point at 460 nm, indicating formation of no additional species within the time window probed. The excited state lifetime of Fl on ZrO_2 is well represented by a biexponential fit, with a large amplitude fast component on the order of ~100 ps, and a long-lived component of several nanoseconds that corresponds well to the lifetime of excited Fl in EtOH solution. The fast lifetime component can be attributed to intermolecular quenching processes resulting from dye molecule proximity as well as incident photon flux. These quenching processes should be carefully examined in the future, but are considered to be inconsequential in this instance where quenching affects only excited state dynamics.

6.2.2. Fl/In_2O_3

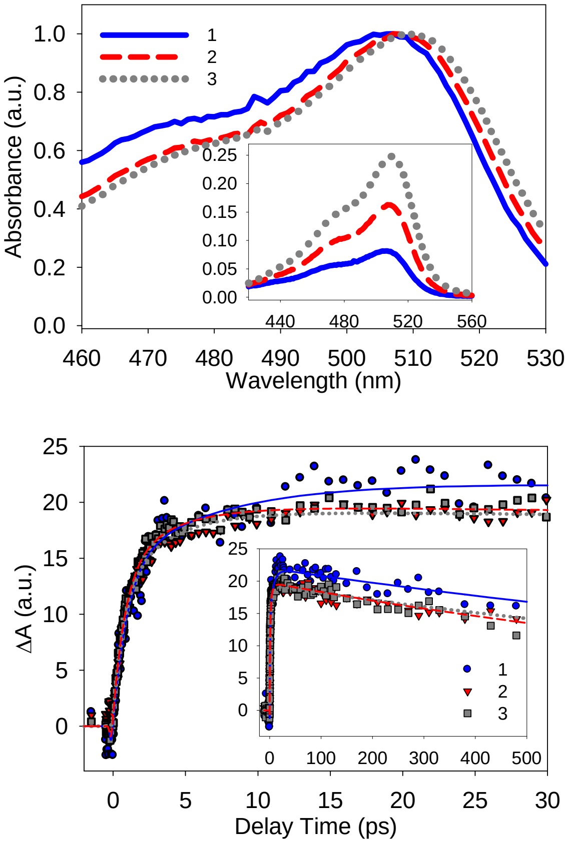

Figure 6.2. (a) UV-visible spectra of Fl/In_2O_3 films at three different dye coverage levels, 1 (0.08 OD), 2 (0.16 OD) and 3 (0.24 OD). The spectra have been normalized to compare the coverage levels with peak maxima. The inset shows the original spectra. (b) IR transient absorption kinetic traces after 500 nm excitation. The inset shows the data extended to longer time scale. Signal sizes have been scaled by the number of absorbed excitation photons, reflecting the relative injection yield of each sample.

6.2.2.1. Transient IR measurement of dye coverage dependence.

As mentioned in the previous section and shown in Figure 6.1, intramolecular quenching as a result of dye aggregation on the semiconductor surface affects the excited state lifetime of Fl when compared to solution-phase measurements. It is well known that organic molecules with large π conjugated systems form ordered aggregates at sufficiently high coverage, requiring a study into the effects of Fl coverage on other substrates, and how these potential aggregates influence injection at varying surface concentration levels. Figure 6.2a shows the normalized UV-visible absorption spectra of Fl adsorbed on In_2O_3 at three different loading levels, and the inset shows the actual absorbances of the films, with loading levels at 505 nm of 0.08, 0.16 and 0.24 OD for samples 1, 2 and 3, respectively. Immediately evident from examination of the normalized spectra is a 5 nm redshift of the absorption maximum as Fl loading increases. From a more detailed study of loading versus absorption peak (not shown), this change begins nearly immediately, indicating that Fl tends to aggregate on In_2O_3 even at very low levels. It is believed that this redshift of absorption maximum is a direct result of J-aggregation on the surface.

Shown in Figure 6.2b are the early time absorption dynamics of injected electrons in In_2O_3 following 500 nm excitation of the adsorbed Fl. The inset shows dynamics extended to later time scale. The probe wavelength used was ~5000 nm, where the absorbance of Fl is neglible, resulting in signal that reflects only the population of injected electrons at a given delay time. The signal amplitudes are scaled to reflect the number of absorbed excitation photons at 500 nm in order to reflect the relative injection yields at each coverage level. A comparison of the three different loading levels shows a noticeable effect of changing dye concentration on injection dynamics. At early time, the growth kinetics appear to be similar up to ~5 ps. However, at the lowest loading level (sample 1), there exists a slower injection component not present in samples 2 and 3. In addition, the relative injection yields of the higher-loading samples are ~10% lower when compared to sample 1. These two changes in dynamics at higher loading levels are attributed to intermolecular quenching of the Fl excited state as a result of aggregation. At low coverage, the slower injection component results from longer-lived excited states of Fl which are subsequently suppressed once surface concentration allows for aggregation to occur. Therefore, at higher dye coverage, the percentage of molecules that would normally undergo slower electron transfer is negligible, resulting in an overall decrease in injection efficiency between Fl and In_2O_3.

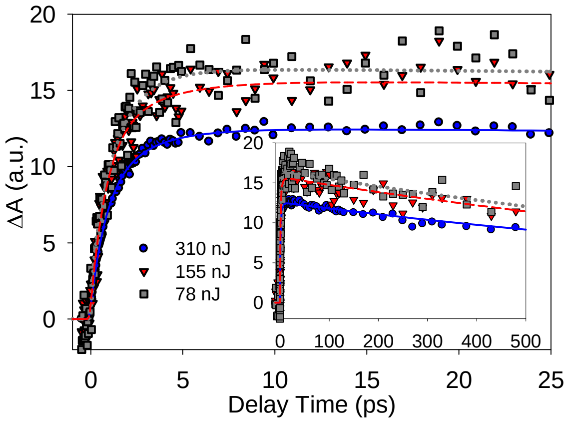

Figure 6.3. Transient IR absorption kinetics of Fl/In_2O_3 (0.09 OD) at different excitation densities of 631, 316 and 159 μJ/cm^2 (shown as 310, 155 and 78 nJ/pulse). Signal sizes

have been scaled by the corresponding pump powers in order to compare the relative injection yield. The inset indicates signal at later time delay.

6.2.2.2. Transient IR measurement and excitation power dependence.

At sufficiently low dye coverage levels, the excited state deactivation pathway due to molecular aggregation becomes negligible. However, it has been previously shown using RuN3-sensitized SnO_2 that molecular proximity is not necessarily required for competive quenching processes. Even in samples with negligible aggregation formation, high excitation power densities have the capability to introduce nonradiative intermolecular energy transfer by exciting sufficient quantities of neighboring adsorbates. In order to examine this effect on injection dynamics, three different excitation densities of 631, 316 and 159 $\mu J/cm^2$ (corresponding to 310, 155 and 78 nJ/pulse, respectively) at 500 nm were used to pump a Fl/In_2O_3 film with peak absorbance of 0.09 OD. By removing aggregate-induced quenching, we were able to make a determination of the excitation powers necessary to minimize intermolecular interactions. Figure 6.3 shows the IR transient absorption kinetics of Fl/In_2O_3 at the three pump powers mentioned previously. The signal sizes have been scaled by the corresponding pump powers in order to reflect the relative injection yields as affected by excitation density. Clearly, at the highest pump power (310 nJ) the injection yield is decreased compared to the two lower pump powers. At these two pump powers (155 and 78 nJ), the kinetics and injection yield are nearly identical, suggesting that at these excitation powers and Fl coverage level, quenching between excited adsorbates is unaffected by either molecular aggregation or overpumping of neighboring dyes. Further comparison of Fl/In_2O_3 injection kinetics with other systems will subsequently use similar conditions for analysis and discussion.

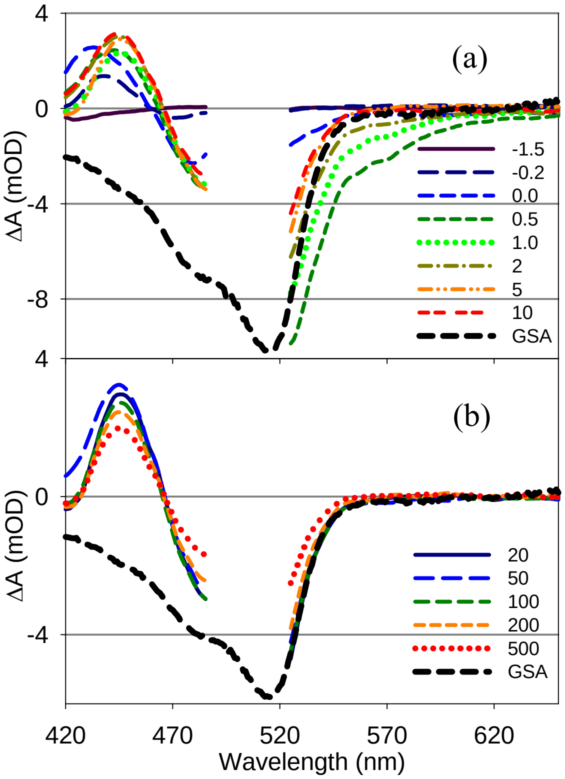

Figure 6.4. Transient visible absorption spectra of Fl/In_2O_3 at delay times (a) -1.5 to 10 ps and (b) 20 to 500 ps after 500 nm excitation. The ground state absorption (GSA, thick black dashed line) has been inverted and scaled for a better comparison with the corresponding bleach. The legends indicate the delay time for each spectrum in picoseconds. At early time delays (a), the spectra show the formation and rapid decay of both excited state Fl absorption at 430 nm and stimulated emission at 570-620 nm. The growth of Fl cation absorption at 450 nm follows the decay of both excited state and stimulated emission, indicating electron transfer from Fl to In_2O_3. At later delay times (b)

after 10 ps, the spectra show only the decay of the Fl cation absorption and recovery of the ground state bleach, which exhibit identical kinetics and can be attributed to the recombination of injected electrons with oxidized Fl.

6.2.2.3. Transient visible spectra of Fl/In_2O_3.

In addition to probing the mid-IR absorption of injected electrons in In_2O_3, we use transient visible absorption spectroscopy in order to observe the dynamics of Fl species during the charge transfer process. Figure 6.4 shows the transient visible absorption spectra of Fl/In_2O_3 (sample absorbance 0.15 OD at 505 nm, pumped with 125 nK/pulse) at both early (a) and late (b) delay times. Figure 6.4a, representing the transient spectra up to 10 ps, shows features identical to the Fl/ZrO_2 spectra in Figure 6.1 at very early delay time (0.5 ps). The observed species consist of a ground state bleach at 505 nm, and excited state absorption and stimulated emission at 430 nm and 560-620 nm, respectively. The static UV-visible ground state absorption (GSA) of Fl/In_2O_3, shown as a thick dashed line, has been inverted and scaled for comparison. After initial excitation of Fl, at later times from 0.5-10 ps we observe quenching of the excited state through both decay in the stimulated emission and decay in the excited state absorption. In addition to these features, we observe the simultaneous formation of an additional absorption band centered at 445 nm, which has been assigned to the oxidized form of Fl.[56,57] As shown in Figure 6.4b, after 10 ps the transient spectra consist of only two features, corresponding to the ground state bleach of Fl and the absorption due to Fl cation. This can be confirmed by the presence of an isosbestic point at 466 nm through the entire later time delay windows, indicating that no other species are formed or depleted, as well as the good agreement of the GSA of Fl/In_2O_3 with the transient ground state bleach. This suggests that the observed decrease in cation absorbance and ground state bleach intensities over time results from recombination of injected electrons with Fl, repopulating the ground state and depleting the number of cations.

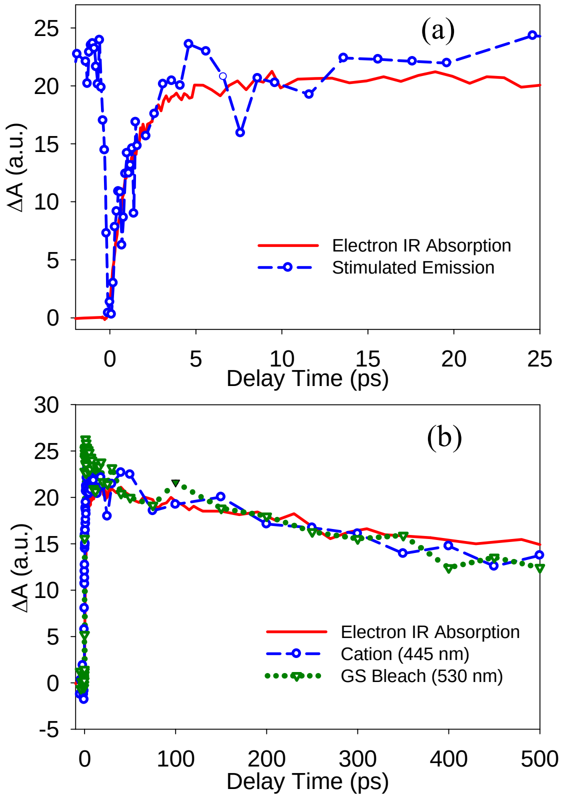

Figure 6.5. (a) Comparison of early-time dynamics of mid-IR electron absorption in In_2O_3 (solid line) and Fl stimulated emission quenching (open circles, dashed line). The signal from SE has been averaged over 565-620 nm to increase signal-to-noise, and inverted and scaled to provide better comparison with the IR injection dynamics. The good agreement confirms the process of electron injection. (b) Comparison of late-time dynamics of mid-IR electron absorption (solid line) with Fl cation absorption at 445 nm (open circles, dashed line) and ground state bleach at 530 nm (open triangles, dotted

line). The signals from Fl cation absorption and GS bleach have been scaled accordingly for comparison with the IR absorption. The good agreement in kinetics between the three species indicates recombination of the injected electron with Fl, reforming molecules in the ground state.

6.2.2.4. Comparison of IR absorption and visible spectral signatures.

By comparing kinetics of the different species formed through charge transfer using mid-IR and visible transient absorption, we provide a clear comparison of injection dynamics from both the donor and acceptor standpoints, allowing an unambiguous assignment of the observed signals. Figure 6.5a shows the early time dynamics of mid-IR electron absorption in Fl/In_2O_3 compared to the quenching of Fl stimulated emission from 565-620 nm. The IR signal was obtained from a Fl/In_2O_3 film with sample absorbance of 0.11 OD using a pump power of 125 nJ in order to minimize both aggregate- and excitation-dependent quenching effects. The kinetics of stimulated emission were obtained by averaging the total SE from 565-620 nm, where it is shown in Figure 6.4a to be the only contribution to the spectra in that region. The SE signal is scaled and displaced vertically in order to present a better comparison with the IR injection kinetics. Clearly, the good agreement between both signals indicates a complete injection process in which all excited Fl is depopulated, forming the Fl cation and injected electrons in In_2O_3. Because of the low sample concentration and low excitation density used for comparison of the two spectral features, the kinetics measured by both SE quenching and mid-IR absorption can be used to represent the electron transfer process from Fl molecules to In_2O_3 film. An accurate comparison of Fl excited state absorption decay with SE quenching and electron absorption was unable to be made, due to the spectral overlap of the excited state absorption at 425 nm with Fl cation at 445 nm and broad Fl ground state bleach at early time.

Figure 6.5b shows the late-time dynamics as a comparison of IR electron absorption in In_2O_3 with absorption of Fl cation at 445 nm and Fl ground state bleach at 530 nm. The signal for Fl cation absorption was averaged from 442-447 nm in order to increase signal to noise, and scaled to provide better comparison with IR electron absorption. Signal for Fl ground state bleach was obtained by averaging from 525-535 nm, and scaling and inverting the signal for comparison. After 10 ps, when injection is shown to be complete as in Figure 6.4b, the three signals decay with identical kinetics. The good agreement between IR electron absorption and Fl species suggests that the decay in IR signal results from a recombination process between In_2O_3 and Fl, rather than a decrease in electron cross section through relaxation in In_2O_3. By correlating charge transfer through both IR and visible features, we show that injection dynamics in different semiconductors can be well represented by their IR absorption, due to greater signal-to noise ratio.

6.2.3. Fl/SnO$_2$

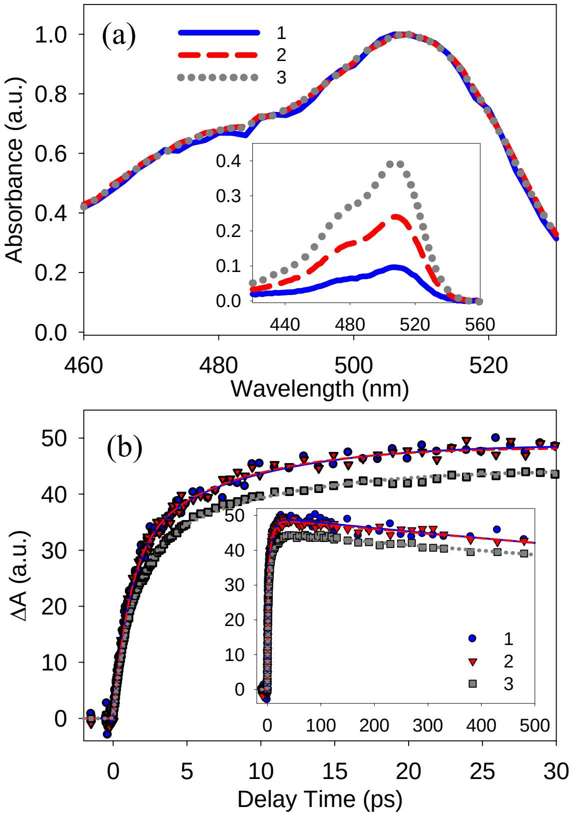

Figure 6.6. (a) UV-visible spectra of Fl/SnO$_2$ films at three different dye coverage levels, 1 (0.1 OD), 2 (0.24 OD) and 3 (0.39 OD). The spectra have been normalized to compare the coverage levels with peak maxima. The inset shows the original spectra. (b) IR transient absorption kinetic traces after 500 nm excitation. The inset shows the data extended to longer time scale. Signal sizes have been scaled by the number of absorbed excitation photons, reflecting the relative injection yield of each sample.

6.2.3.1 Transient IR measurement of dye coverage dependence.

Figure 6.6a shows the UV-visible spectra of different Fl/SnO_2 films at different dye coverage levels (0.1, 0.24, and 0.39 OD for samples 1, 2 and 3 respectively). The spectra have been normalized for comparison and show no absorption peak shift resulting from aggregation as Fl concentration increases. The inset shows the absorbance of the films before normalization. The IR absorption of injected electrons in these films is shown in Figure 6.6b, where after 500 nm excitation (~100 nJ/pulse) the transient absorption was recorded, centered at 5000 nm. The signal amplitudes have been scaled by the number of absorbed photons (sample OD) in order to show a better comparison of the effect of increasing Fl concentration. Injection kinetics for the three samples are identical, even at longer delay time (inset), but samples 1 and 2 (corresponding to 0.1 and 0.24 OD, respectively) show a higher injection yield than sample 3 (0.39 OD). Since aggregation has been determined to be negligible, the lower injection yield resulting from high Fl concentration is attributed to intermolecular energy transfer, quenching excited state Fl as a result of molecular proximity on the SnO_2 surface.

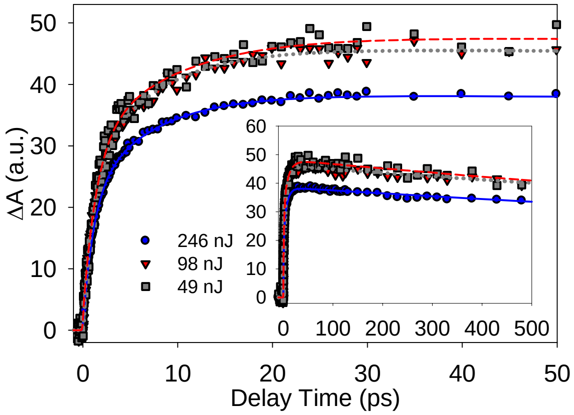

Figure 6.7. Transient IR absorption kinetics of Fl/SnO_2 (0.11 OD) at different excitation densities of 501, 200 and 100 μJ/cm^2 (shown as 246, 98 and 49 nJ/pulse). Signal sizes have been scaled by the corresponding pump powers in order to compare the relative injection yield. The inset indicates signal at later time delay.

6.2.3.2 Transient IR measurement and excitation power dependence.

Figure 6.7 shows the IR absorption kinetics of a Fl/SnO_2 film (absorbance 0.11 OD at 505 nm) pumped with three excitation densities at 500 nm of 501, 200 and 100 μJ/cm^2 (shown in Figure 6.7 as 246, 98 and 49 nJ/pulse). The signal sizes have been scaled by the corresponding pump powers in order to reflect the relative injection yields, with longer time delays shown in the inset. At all excitation densities, the electron absorption follows identical kinetics, but for samples 1 and 2 (lower pump powers), the relative injection yield is the same while the highest pump power sample gives a relative yield ~20% less. This suggests that at pump powers of significant intensity, quenching between neighboring excited Fl becomes a competitive relaxation pathway even in the absence of aggregation. At sufficiently low pump powers, as in samples 1 and 2, this quenching is shown to be negligible. Comparisons of dynamics of Fl/SnO_2 will subsequently be shown using conditions that minimize the quenching effects of molecular proximity and excitation density.

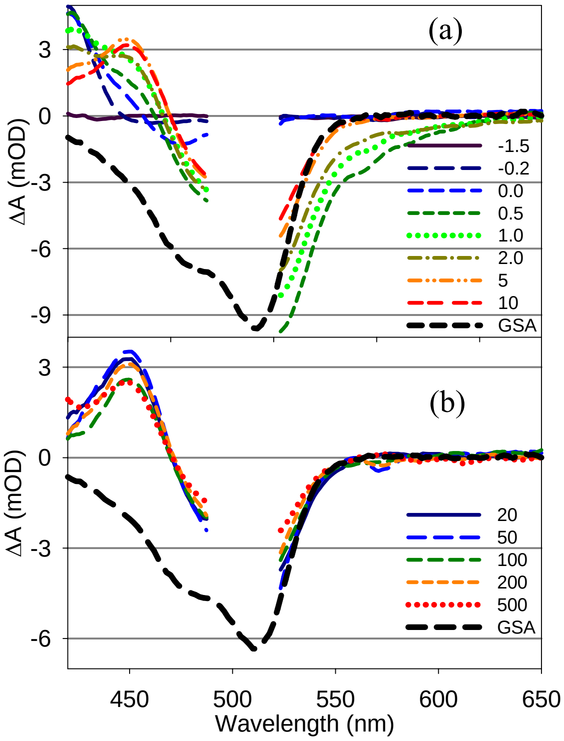

Figure 6.8. Transient visible absorption spectra of Fl/SnO$_2$ at delay times (a) -1.5 to 10 ps and (b) 20 to 500 ps after 500 nm excitation. The ground state absorption (GSA, thick black dashed line) has been inverted and scaled for a better comparison with the corresponding bleach. The legends indicate the delay time for each spectrum in picoseconds. At early time delays (a), the spectra show the formation and rapid decay of both excited state Fl absorption at 430 nm and stimulated emission at 570-620 nm. The growth of Fl cation absorption at 450 nm follows the decay of both excited state and stimulated emission, indicating electron transfer from Fl to SnO$_2$. At later delay times (b) after 10 ps, the spectra show only the decay of the Fl cation absorption and recovery of the ground state bleach, which exhibit identical kinetics and can be attributed to the recombination of injected electrons with oxidized Fl.

6.2.3.3 Transient visible spectra of Fl/SnO_2.

Figures 6.8a and 6.8b show the visible transient absorption spectra of Fl/SnO_2 at different delay times after excitation (sample absorbance 0.12 OD at 505 nm, with pump power 78 nJ/pulse at 500 nm). The transient spectra at early delay time (up to 10 ps) are shown in Figure 6.8a, which exhibit nearly identical features as observed for Fl/In_2O_3 visible absorption measurements. Directly after excitation, the simultaneous excited state absorption of Fl at 425 nm and ground state bleach at 505 nm is observed. The ground state absorption spectrum (GSA) is shown inverted for comparison (thick dashed line). As well as excited state absorption, the associated stimulated emission from 560-620 nm is evident. Up to 5 ps, we observe the decay in signal from both excited Fl absorption and stimulated emission, and the formation of the Fl cation absorption at 445 nm, indicating electron injection within this window from excited Fl to SnO_2. After 10 ps, as shown in Figure 6.8b, the only features contributing to the difference spectra are the Fl cation absorption and ground state bleach, as evidenced by the identical relative absorption magnitudes and isosbestic point present at 470 nm. This gives additional evidence that the electron transfer process is completed well within the early time window, and any changes in relative signal intensities for oxidized and ground state Fl are directly related to the process of electron recombination from SnO_2 to Fl cations.

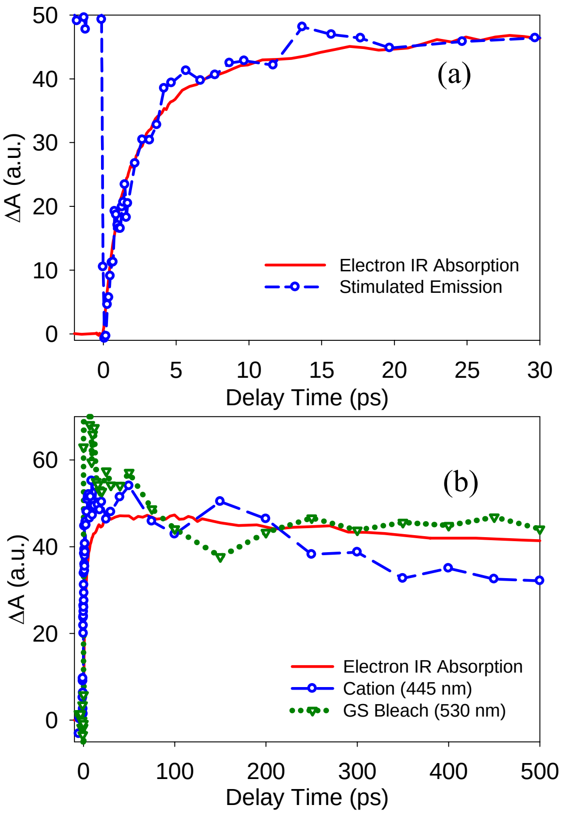

Figure 6.9. (a) Comparison of early-time dynamics of mid-IR electron absorption in SnO_2 (solid line) and Fl stimulated emission quenching (open circles, dashed line). The signal from SE has been averaged over 565-620 nm to increase signal-to-noise, and inverted and scaled to provide better comparison with the IR injection dynamics. The good agreement confirms the process of electron injection. (b) Comparison of late-time dynamics of mid-IR electron absorption (solid line) with Fl cation absorption at 445 nm (open circles, dashed line) and ground state bleach at 530 nm (open triangles, dotted line). The signals from Fl cation absorption and GS bleach have been scaled accordingly for comparison with the IR absorption. The good agreement in kinetics between the three species indicates recombination of the injected electron with Fl, reforming molecules in the ground state.

6.2.3.4 Comparison of IR absorption and visible spectral signatures.

A comparison of the IR electron absorption kinetics in SnO_2 with the excited state (stimulated emission) quenching of Fl is shown in Figure 6.9a. The stimulated emission kinetics were obtained by averaging the signal from 565-620 nm at different time delays, and scaled for a better comparison with the electron absorption kinetics at 5000 nm. The kinetics of electron absorption agree well with the Fl excited state quenching, indicating electron transfer from Fl to SnO_2 with negligible competitive deactivation pathways contributing to the observed signal.

At later time delay, as shown in Figure 6.9b, the decay in oxidized Fl absorption (445 nm) and ground state bleach recovery (530 nm) agree well with the observed decay in electron absorption. As in the case of Fl/In_2O_3, these signals indicate that at later times, the decrease in electron absorption is a direct observation of recombination from SnO_2 to oxidized Fl, rather than electron cross section decay as a result of relaxation through the SnO_2 conduction band.

6.2.4. Fl/ZnO

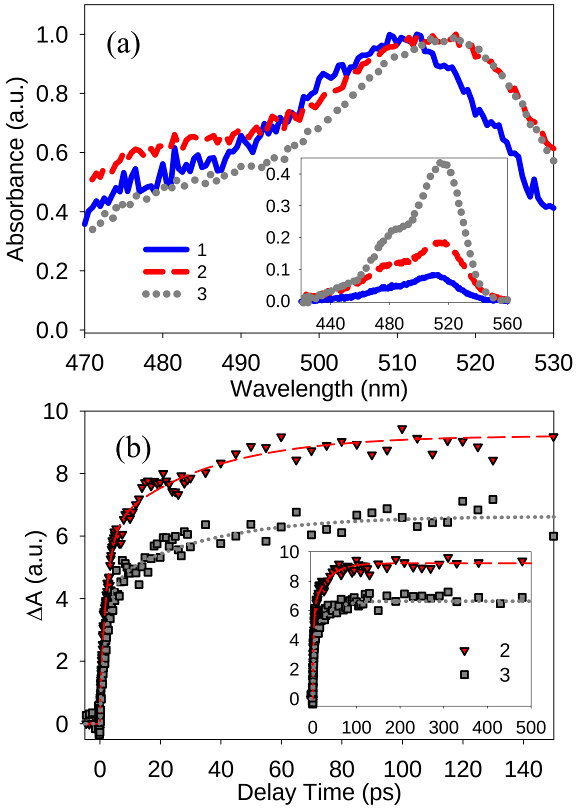

Figure 6.10. (a) UV-visible spectra of Fl/ZnO films at three different dye coverage levels, 1 (0.08 OD), 2 (0.18 OD) and 3 (0.44 OD). The spectra have been normalized to compare the coverage levels with peak maxima. The inset shows the original spectra. (b) IR transient absorption kinetic traces for samples 2 and 3 after 500 nm excitation. The inset shows the data extended to longer time scale. Signal sizes have been scaled by the number of absorbed excitation photons, reflecting the relative injection yield of each sample.

6.2.4.1 Transient IR measurement of dye coverage dependence.

The normalized absorption spectra for samples of Fl/ZnO with different dye coverages (0.08, 0.18 and 0.44 OD for samples 1, 2 and 3, respectively) are shown in

Figure 6.10a, where the inset shows the actual absorbances of the three films. A 6 nm redshift of absorption peak maximum is evident as dye loading increases, from 511 nm at low coverage to 517 at high coverage. This shift in absorption maximum is attributed to J-aggregation of the Fl dyes as concentration on the ZnO surface increases.

Shown in Figure 6.10b are the transient electron absorption measurements for samples 2 and 3. The samples were pumped at 500 nm with ~500 nJ/pulse and probed at 5000 nm. The signal sizes are scaled to reflect the relative injection yield of each sample based on number of absorbed photons. Because of the smaller electron cross section in ZnO and surface inhomogeneity of the nanoporous films, sample 1 (lowest coverage) was unusable for an accurate comparison of relative injection yield due to signal to noise considerations. The injection kinetics appear to be quite similar for both coverage samples, however the high loading sample (3) shows a ~30% decrease in relative injection yield when compared to sample 2. There are several possible explanations for the reduced injection yield. The first of these is excited state quenching as a result of aggregation as mentioned previously. A second source of reduced injection efficiency may also arise from the high loading level in sample 3 in a manner similar to that of the Fl/SnO_2 high coverage sample presented in the previous section. At sufficiently high coverage where aggregation is already known to have occurred, the Fl excited state may be deactivated by both aggregation and excited state quenching resulting from intermolecular proximity even when not preferentially ordered on the surface.

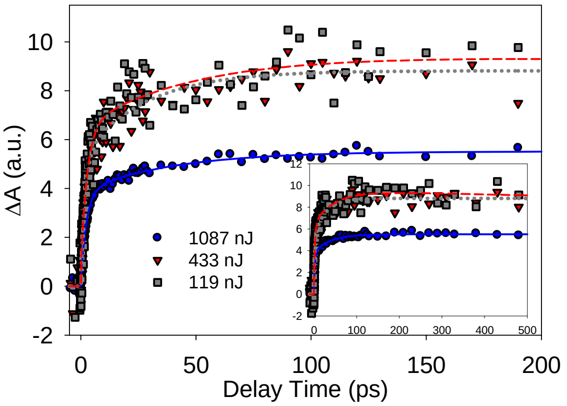

Figure 6.11. Transient IR absorption kinetics of Fl/ZnO (0.19 OD) at different excitation densities of 2214, 882 and 405 μJ/cm^2 (shown as 1087, 433 and 119 nJ/pulse). Signal sizes have been scaled by the corresponding pump powers in order to compare the relative injection yield. The inset indicates signal at later time delay.

6.2.4.2 Transient IR measurement and excitation power dependence.

The transient electron absorption kinetics of a sample of Fl/ZnO (peak absorbance 0.19 OD at 514 nm) pumped at three different excitation densities at 500 nm (2214, 882 and 405 μJ/cm^2, represented as 1087, 433 and 119 nJ/pulse for samples 1, 2 and 3, respectively) are shown in Figure 6.11. The transient absorptions for each sample have been normalized to correspond to the excitation densities used, in order to reflect the relative injection yields. At the two lowest pump powers, the injection kinetics of the electron in ZnO are nearly identical, with relative yields invariant to the number of excitation photons. This indicates that at these lower pump powers, quenching between nearby excited Fl dyes is negligible at this coverage level. The highest pump power sample shows similar injection kinetics, however has an injection yield ~40% lower than the samples under lower power irradiation.

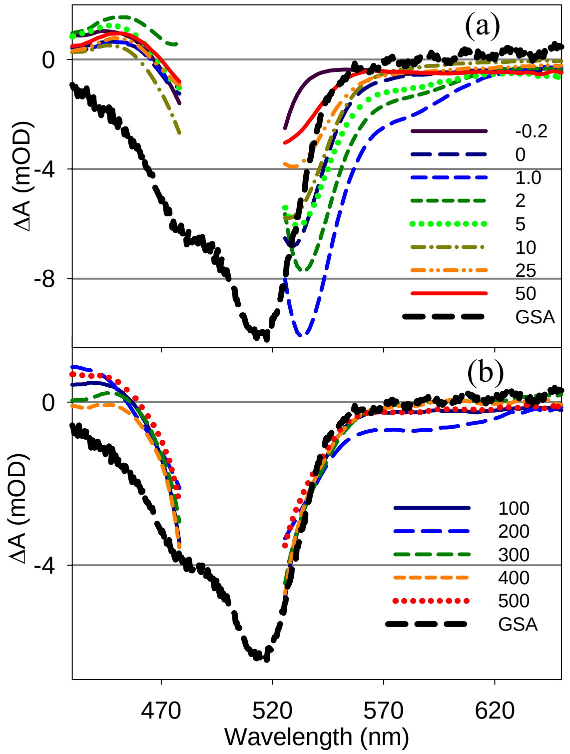

Figure 6.12. Transient visible absorption spectra of Fl/ZnO at delay times (a) -1.5 to 50 ps and (b) 100 to 500 ps after 500 nm excitation. The ground state absorption (GSA, thick black dashed line) has been inverted and scaled for a better comparison with the corresponding bleach. The legends indicate the delay time for each spectrum in picoseconds. At early time delays (a), the spectra show the formation and rapid decay of both excited state Fl absorption at 430 nm and stimulated emission at 570-620 nm. The decay of stimulated emission indicates electron transfer from Fl to ZnO. At later delay times (b) after 100 ps, the spectra show only a small contribution from Fl cation absorption and presence of the ground state bleach, the latter of which is long-lived, indicating a recombination of injected electrons with oxidized Fl beyond the timescale of our measurements.

6.2.4.3 Transient visible spectra of Fl/ZnO.

The transient visible absorption spectra of Fl/ZnO are shown in Figure 6.12 (0.17 OD at 513 nm with pump power of ~320 nJ/pulse at 500 nm). At early delay time (~1 ps) as shown in Figure 6.12a, the spectrum consists of the ground state bleach of Fl at 513 nm, and contributions from excited Fl consisting of the excited state absorption at 435 nm and stimulated emission from 560-620 nm. At later time after 50 ps, shown in Figure 6.12b, the stimulated emission from excited Fl is quenched, which we attribute to electron injection to ZnO. This is supported by the persistence of the ground state bleach, which at later delay times does not appreciably decay, and the presence of a small absorption feature at ~450 nm, which we attribute to oxidized Fl as a result of complete stimulated emission quenching shorter than the excited state lifetime. There is negligible decay in amplitude for the ground state bleach at 530 nm, indicating that recombination of electron from ZnO to oxidized Fl is on a timescale longer than the course of our measurements.

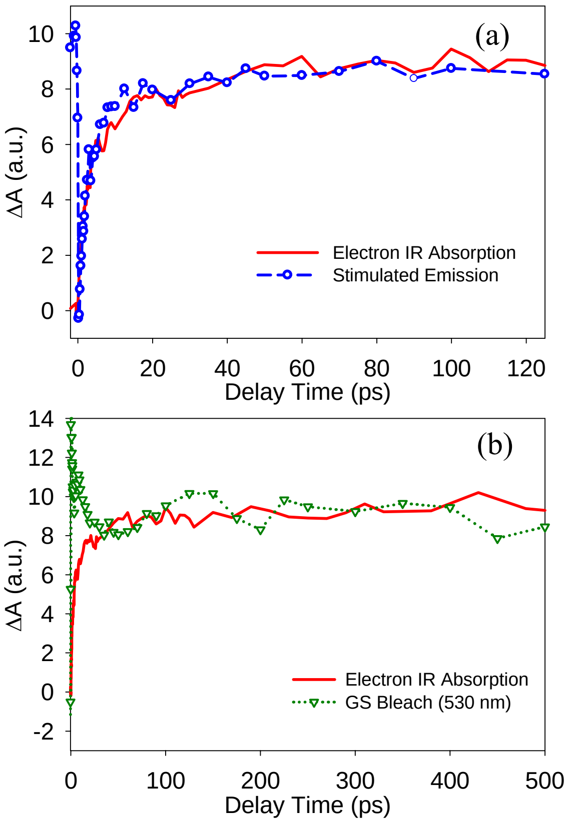

Figure 6.13. (a) Comparison of early-time dynamics of mid-IR electron absorption in ZnO (solid line) and Fl stimulated emission quenching (open circles, dashed line). The signal from SE has been averaged over 565-620 nm to increase signal-to-noise, and inverted and scaled to provide better comparison with the IR injection dynamics. The good agreement confirms the process of electron injection. (b) Comparison of late-time dynamics of mid-IR electron absorption (solid line) with Fl ground state bleach at 530 nm (open triangles, dotted line). The signal from Fl GS bleach has been scaled accordingly for comparison with the IR absorption. The good agreement in kinetics between the two species indicates that recombination of the injected electron with Fl is slower than the timescale of our measurements.

6.2.4.4 Comparison of IR absorption and visible spectral signatures.

Due to the larger ZnO particle size and sensitivity of the transient visible measurements to both surface coverage and homogeneity, the ZnO film introduced significant fluctuations in the observed signal. In the region near 430-460 nm, where the intensity of our WL continuum probe was ~15% of the maximum amplitude, the resultant noise introduced nontrivial error into the dynamics of both the Fl excited state and cation absorptions, making clear observations in that spectral region ambiguous. Regardless, the presence of stimulated emission from 560-620 nm where our probe had significant signal-to-noise allowed an unambiguous probe of excited state dynamics with regards to electron injection, as compared in Figure 6.13a with the electron absorption in ZnO at early time delay. These two signal traces are identical, indicating that excited state Fl decays as a result of electron transfer to ZnO rather than competitive quenching. This observation is consistent with the pump power and coverage dependences mentioned previously, as sample absorbance was 0.17 OD at 513 nm with an excitation power of 320 nJ/pulse at 500 nm.

At later time delay, as shown in Figure 6.13b, the electron absorption at 5000 nm is compared with the ground state recovery kinetics of Fl at 530 nm. The cation absorption at 445 nm is unresolvable within an acceptable signal to noise ratio as mentioned previously. However, it has already been demonstrated that the decay kinetics of oxidized Fl are identical to those of the ground state bleach recovery in the absence of other species. Quenching of stimulated emission corresponding to electron transfer shows that depopulation of Fl ground state is a result of the cation species rather than long-lived Fl excited states. We see that the ground state bleach exhibits no recovery on the timescale of our measurements, consistent with the electron absorption kinetics of ZnO monitored in the mid-IR. It is reasonable to assume, based on these observations, that recombination from ZnO to oxidized Fl is negligible within the time delays probed.

6.2.5. Comparison of Electron Injection from Fl to In_2O_3, SnO_2 and ZnO Films

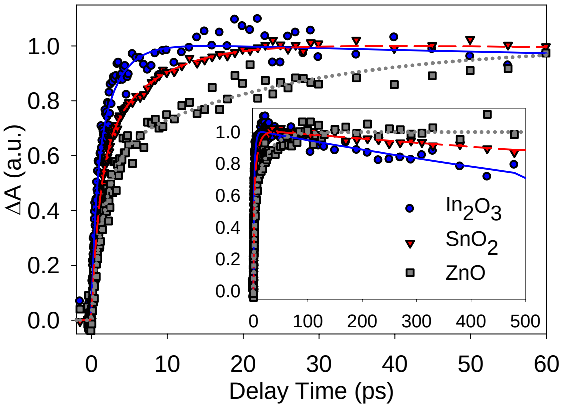

Figure 6.14. IR electron absorption kinetics traces of Fl on In_2O_3, SnO_2 and ZnO films averaged over multiple trials. All kinetic traces have been normalized to maximum amplitude for better comparison. The inset shows kinetics at longer time delays.

Shown in Figure 6.14 are the averaged IR absorption kinetics for Fl on In_2O_3, SnO_2 and ZnO films. The traces are normalized to maximum amplitude for better comparison. They were obtained by averaging the multiple trials for each sample completed at both low excitation power and dye coverage as described in the previous sections. Under these conditions, both aggregation of Fl and excitation of neighboring dye molecules on the semiconductor surfaces are understood to be negligible. With this assumption, we find that the injection rates for the three semiconductors follow the trend of $In_2O_3 \geq SnO_2 > ZnO$.

In order to numerically quantify the rates, we adopt a method used in previous work. The injection kinetics for the three semiconductors are well fit by a minimum of two exponential rise functions, where the amplitudes of each rise component and their associated time constants are summarized in Table 6.1. To make a relative comparison of injection times for each semiconductor with a single quantity, the effective weighted injection timescale τ_{ave} has also been shown in Table 6.1. For each semiconductor, τ_{ave} is calculated as:

$$\tau_{ave} = \frac{A_1\tau_1 + A_2\tau_2}{A_1 + A_2} \tag{6.1}$$

The weighted electron injection times for Fl to In_2O_3, SnO_2 and ZnO are 1.69, 3.68, and 10.9 ps, respectively. As discussed in previous sections, the decay in electron absorption signal is a feature assigned directly to recombination of injected electrons with oxidized Fl rather than cross-section relaxation. This recombination process occurs over a timescale longer (>1 ns) than the course of our measurements for all three semiconductors, and as such is outside the scope of this investigation, although interesting as a further study for future measurements.

Table 6.1. Fitting parameters for Fl/semiconductor film injection kinetics averaged over multiple trials.

	A_1	τ_1 (ps)	A_2	τ_2 (ps)	τ_{ave} (ps)
In_2O_3	0.47	0.61	0.53	2.65	1.69
SnO_2	0.58	1.14	0.42	7.17	3.68
ZnO	0.6	1.8	0.4	24.2	10.9

6.3 Discussion

As shown in Figure 6.14 and Table 6.1, the electron transfer rate from Fl to SnO_2 is roughly two times that of Fl to In_2O_3, and 6 times that of Fl to ZnO. The difference in electron transfer rate between the three can be attributed to the difference in the density of accepting states within the different semiconductors and/or the electronic coupling of Fl to the different nanocrystals according to Marcus theory of interfacial electron transfer.[58-61] In order to examine the contribution of these two factors we use a simplified model that was previously used to account for the effect of variations in density of states on the rate of electron injection to different semiconductors.[62] It is assumed that electronic interaction of the adsorbate excited state with the nanoparticle involves the first metal atom that is in direct contact with the donor, with a total strength of H_0, and that the density of electron accepting states is given by the total density of unoccupied states in the semiconductor (conduction band and defect states). Within this model, the total injection rate is given by[62,63]

$$k_{ET} = \frac{2\pi}{\hbar}\int_{-\infty}^{\infty} d\varepsilon \rho_0(\varepsilon)|H_0|^2 \frac{1}{\sqrt{4\pi\lambda k_B T}} \exp[-\frac{(\lambda + \Delta G_0 + \varepsilon)^2}{4\lambda k_B T}] \tag{6.2}$$

where ε is the energy relative to the band edge; $\rho_0(\varepsilon)$ is the density of states per unit energy within the effective volume per metal center, V_0 (defined as unit cell volume/number of metal centers per cell); ΔG_0 is the driving force for electron transfer from the adsorbate (with excited state oxidation potential of $V(S^+/S^*)$ to the conduction band edge (V_{CB})); and λ is the total reorganization energy. The density of states near the conduction band edge in a perfect oxide crystal is given by

$$\rho_{0C}(\varepsilon)d\varepsilon = V_0 \frac{(2m^*)^{3/2}}{2\pi^2\hbar^3}\sqrt{\varepsilon}d\varepsilon \tag{6.3}$$

where m* is the effective mass of electrons in the conduction band. We assume that the presence of defects perturbs the energy of a perfect crystal and the energy perturbation obeys a Gaussian distribution function with a width of Δ.[64] The density of states in nanocrystalline films can be modeled as

$$\rho_0(\varepsilon) = \int_0^\infty \rho_{0c}(\varepsilon')\frac{1}{\Delta\sqrt{2\pi}}e^{-\frac{(\varepsilon-\varepsilon)^2}{2\Delta^2}}d\varepsilon' \tag{6.4}$$

According to this model, the density of states above the band edge is similar to that of a perfect crystal, but they differ significantly near and below the band edge.

The density of states in these materials can be estimated from the electron effective mass and the effective volume, which are (0.3 m_0, 32 A^3), (0.275 m_0, 35.7 A^3) and (0.28 m_0, 23.8 A^3) for In_2O_3,[65,66] SnO_2[66,67] and ZnO,[65,68] respectively, where m_0 is the rest mass of free electron. The conduction band edge positions of metal oxides are known to shift with pH according to the Nernstian equation:

$$V_{fb} = V_{fb}^0 - pH * 0.059V \tag{6.5}$$

where V_{fb}^0 , the potential at pH=0, is reported to be -0.01 V, +0.07 V and -0.4 V (vs SCE) for In_2O_3,[69] SnO_2[70] and ZnO,[3] respectively. To illustrate the effect of density of states variation on the semiconductor dependence, we compare the calculated ET rate to these semiconductors at a fixed total coupling strength of 560 cm^{-1}, as shown in Figure 6.15. We have also assumed a defect distribution width Δ of 100 mV,[62] and a total reorganization energy of 0.3 V. All rates are plotted as a function of $\Delta G_0 = -e[V(S^+/S^*) - V_{fb}(SnO_2)]$. Because of the different band edge positions, the calculated curves have different onset points in these materials. SnO_2 and In_2O_3, with similar band edge positions and electron effective masses, are predicted to have similar densities of electron accepting states and similar ET rates at most adsorbate potentials. For ZnO, because of its higher band edge (a more negative flat band potential), both densities of accepting states and rate of ET from the same adsorbate are significantly smaller than those to SnO_2 and In_2O_3.

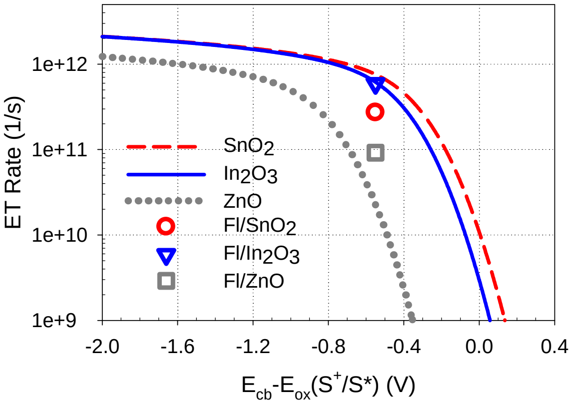

Figure 6.15. Comparison of predicted rates of ET to In_2O_3 (blue solid line), SnO_2 (red dashed line) and ZnO (grey dotted line) as a function of adsorbate excited state oxidation potential. The rates are calculated according to Equation 6.2 with a total electronic coupling strength $H_0 = 560\ cm^{-1}$ and reorganization energy of 0.3 V. The measured ET rates from Fl to In_2O_3 (triangle), SnO_2 (circle) and ZnO (square) are also plotted by assuming that their band edges were given by those at pH 7.

The excited state oxidation potential of Fl is ~-0.89 V (vs SCE). During the measurement, the films were exposed to air and were covered by adsorbed water.[71] The band edge positions under this environment have not been well determined. However, previous studies of the binding character of Fl have demonstrated that a shift in UV-vis absorption spectra is observed when the pH of the adsorbate environment is changed due to different protonation states of Fl.[72] The absorption spectra we observe in our experiments correspond to the dianionic form of Fl, indicating that the pH of our thin film samples is >5. Assuming that it is similar to those in pH 7 buffer, we have estimated a ΔG_0 [$=-e(V_{fb}(SnO_2)-V(S^+/S^*]$ value of -0.55 V. The measured rates to SnO_2, In_2O_3 and ZnO are plotted on the same curve for comparison in Figure 6.15.

For In_2O_3, the calculated ET rate is similar to the measured value. Within the current model, the measured rate would correspond to a total coupling strength of 560 cm^{-1}. The calculated value for ET to SnO_2 is nearly 3 times the measured value. Because the band edge of SnO_2 at pH 7 is calculated to be ~0.55 V lower than the excited state oxidation potential of Fl, we do not expect a significant deviation in electron transfer rate due to a slight difference in energetics, as the density of accepting states in SnO_2 changes slowly at this level. It is interesting to note that in our study of electron transfer from RhB to the same semiconductors, SnO_2 and In_2O_3 showed quite similar charge transfer rates, which was attributed to the coupling between the excited RhB and semiconductors given their comparable density of states at the RhB excited state oxidation potential of -0.94, quite close to that of Fl. This suggests that the coupling strength of Fl to SnO_2 is different than expected in our calculations. The calculated value for ZnO is significantly smaller than that measured. As shown in Figure , the Fl excited state potential is close to that of the ZnO band edge (-0.81 V at pH 7), and the calculated rate in this region depends sensitively on the reorganization energy, the band edge position, and the defect density of states,[62] none of which have been accurately determined in this case. Of particular importance to the Fl/semiconductor systems under study, especially where deviation in expected behavior is observed, is that the dianionic form of the dye is observed to be present on all three semiconductors. In our study of RhB, it was assumed that the dye coupled to the semiconductor surfaces through the single carboxylate anchoring group. While this is one possibility for attachment of Fl, it has been shown recently in computational studies that both deprotonated sites in a similar xanthene molecule (eosin-Y) contribute to adsorption to various metal sites on the surface of ZnO, changing the overall electronic coupling of the system due to a flat, rather than vertical, molecular orientation.[73] Evidence for this multi-site dianionic adsorption has also been observed in laboratory settings with Fl adsorbed on colloidal TiO_2 nanoparticles.[31,55,72] It is suggested that deviations from expected values in experimentally measured electron transfer rates are related to changes in coupling of Fl to the semiconductor surface due to this effect, as well as uncertainty into the exact surface conditions under study. The lack of any observed IBCSP intermediates would seem to support this argument, as strong coupling to acceptor states that might form intermediates would be hindered in a flat molecular geometry where the π-conjugated xanthene ring structure is out of the plane of the carboxylate-to-metal electronic binding configuration. Further investigation and evaluation of this would be of great interest, especially with the possibility of further computational studies to examine the conformational coupling dependence given multiple binding sites.

6.4 Summary

The electron transfer kinetics from Fl to In_2O_3, SnO_2 and ZnO have been compared in an effort to probe the semiconductor dependence on electron transfer rate, as well as any role that previously-observed charge-transfer intermediates might have on influencing dissociation of the electron into bulk semiconductor. The kinetics of the decay of Fl excited state are measured by transient visible absorption spectroscopy to probe the rate of charge separation by directly forming the oxidized form of Fl. The injection of electrons in the semiconductors is probed by growth of the free carrier absorption in the mid-IR, and compared with results measured in the visible region. For Fl on all three semiconductors, the rate of the overall electron transfer process is determined by the rate of initial charge separation across the interface to form the IBCSPs, which dissociate with negligible lifetimes. Direct injection of the electron into the bulk semiconductor is mediated by the electronic coupling between the excited Fl-SC donor-acceptor pair and the density of accepting states. The charge separation rate to In_2O_3 is ~ 1.7 ps, which agrees with our calculated rates based on the density of states at pH 7. The injection rate to SnO_2 is ~ 3.7 ps, which is several times slower than that to In_2O_3 and the expected rate based on our calculations. The ET rate to ZnO is ~ 10.9 ps, several times faster than the calculated values but much more sensitive to changes in the accepting density of states near the conduction band edge, which is not clear from our sample conditions. The trend of ET rate to these oxides from Fl is attributed to both the density of conduction band states and different electronic coupling values based on the manner in which the dianionic form of Fl binds itself to the semiconductor surface, which is still unclear.

References

(1) Miller, R. J. D.; McLendon, G. L.; Nozik, A. J.; Schmickler, W.; Willig, F. *Surface electron transfer processes*; VCH publishers, Inc., 1995.

(2) Kamat, P. V. *Chem. Rev.* **1993**, *93*, 267.

(3) Hagfeldt, A.; Gratzel, M. *Chem. Rev.* **1995**, *95*, 49.

(4) Nazeeruddin, M. K.; Kay, A.; Rodicio, I.; Humphrybaker, R.; Muller, E.; Liska, P.; Vlachopoulos, N.; Gratzel, M. *J. Am. Chem. Soc.* **1993**, *115*, 6382.

(5) O'Regan, B.; Gratzel, M. *Nature* **1991**, *353*, 737.

(6) Hara, K.; Horiguchi, T.; Kinoshita, T.; Sayama, K.; Sugihara, H.; Arakawa, H. *Sol. Energy Mater. Sol. Cells* **2000**, *64*, 115.

(7) Bedja, I.; Hotchandani, S.; Kamat, P. V. *J. Phys. Chem.* **1994**, *98*, 4133.

(8) Ferrere, S.; Zaban, A.; Gregg, B. A. *J. Phys. Chem. B* **1997**, *101*, 4490.

(9) Sayama, K.; Sugihara, H.; Arakawa, H. *Chem. Mater.* **1998**, *10*, 3825.

(10) Rensmo, H.; Keis, K.; Lindstrom, H.; Sodergren, S.; Solbrand, A.; Hagfeldt, A.; Lindquist, S. E.; Wang, L. N.; Muhammed, M. *J. Phys. Chem.* **1997**, *101*, 2598.

(11) Aegerter, M. A. *Sol. Energy Mater. Sol. Cells* **2001**, *68*, 401.

(12) Aegerter, M. A.; Schmitt, M.; Guo, Y. *Int. J. Photoenergy* **2002**, *4*, 1.

(13) Hu, L. L.; Wolf, M.; Gratzel, M.; Jiang, Z. H. *J. Sol-Gel Sci. Technol.* **1995**, *5*, 219.

(14) Barros Filho, D. d. A.; Abreu Filho, P. P.; Werner, U.; Aegerter, M. A. *J. Sol-Gel Sci. Technol.* **1997**, *8*, 735.

(15) Lenzmann, F.; Krueger, J.; Burnside, S.; Brooks, K.; Graetzel, M.; Gal, D.; Ruehle, S.; Cahen, D. *J. Phys. Chem. B* **2001**, *105*, 6347.

(16) Katoh, R.; Furube, A.; Yoshihara, T.; Hara, K.; Fujihashi, G.; Takano, S.; Murata, S.; Arakawa, H.; Tachiya, M. *J. Phys. Chem. B* **2004**, *108*, 4818.

(17) Wang, L.; Ernstorfer, R.; Willig, F.; May, V. *J. Phys. Chem. B* **2005**, *109*, 9589.

(18) Szarko, J.; Neubauer, A.; Bartelt, A.; Socaciu-Siebert, L.; Birkner, F.; Schwarzburg, K.; Hannappel, T.; Eichberger, R. *J. Phys. Chem. C* **2008**, *112*, 10542.

(19) Stockwell, D.; Yang, Y.; Huang, J.; Anfuso-Cleary, C.; Huang, Z.; Lian, T. *J. Phys. Chem. C* **2010 (accepted)**.

(20) Ramakrishna, G. G., Hirendra N. *J. Phys. Chem. A.* **2002**, *106*, 2545.

(21) Hao, E.; Anderson, N. A.; Asbury, J. B.; Lian, T. *J. Phys. Chem. B* **2002**, *106*, 10191.

(22) Morandeira, A.; Boschloo, G.; Hagfeldt, A.; Hammarstroem, L. *J. Phys. Chem. B FIELD Full Journal Title:Journal of Physical Chemistry B* **2005**, *109*, 19403.

(23) Furube, A.; Katoh, R.; Hara, K.; Sato, T.; Murata, S.; Arakawa, H.; Tachiya, M. *J. Phys. Chem. B* **2005**, *109*, 16406.

(24) Wachtveitl, J.; Huber, R.; Sporlein, S.; Moser, J. E.; Gratzel, M. In *Int. J. Photoenergy* 1999; Vol. 1, p 153.

(25) Wang, Z.-S.; Hara, K.; Danoh, Y.; Kasada, C.; Shinpo, A.; Suga, S.; Arakawa, H.; Sugihara, H. *J. Phys. Chem. B* **2005**, *109*, 3907.

(26) Ghosh, H. N.; Asbury, J. B.; Lian, T. *J. Phys. Chem. B* **1998**, *102*, 6482.

(27) Cave, R. J.; Burke, K.; Castner, E. W., Jr. *Journal of Physical Chemistry A* **2002**, *106*, 9294.

(28) Cave, R. J.; Castner, E. W., Jr. *Journal of Physical Chemistry A* **2002**, *106*, 12117.

(29) Maroncelli, M.; Fleming, G. R. *J. Chem. Phys.* **1987**, *86*, 6221.

(30) Singh, T. S.; Madhava Rao, B. S.; Mohan, H.; Mittal, J. P. *J. Photochem. Photobiol., A* **2002**, *153*, 163.

(31) Benko, G.; Hilgendorff, M.; Yartsev, A. P.; Sundstrom, V. *J. Phys. Chem. B* **2001**, *105*, 967.

(32) Alig Anna, R. G.; Gourdon, D.; Israelachvili, J. *J Phys Chem B FIELD Full Journal Title:The journal of physical chemistry. B* **2007**, *111*, 95.

(33) Huang, J.; Stockwell, D.; Boulesbaa, A.; Guo, J.; Lian, T. *J. Phys. Chem. C* **2008**, *112*, 5203.

(34) Biesmans, G.; Vanderauweraer, M.; Cathry, C.; Meerschaut, D.; Deschryver, F. C.; Storck, W.; Willig, F. *J. Phys. Chem.* **1991**, *95*, 3771.

(35) Hashimoto, K.; Hiramoto, M.; Sakata, T. *Chem. Phys. Lett.* **1988**, *148*, 215.

(36) He, J. J.; Chen, F.; Zhao, J. C.; Hidaka, H. *Colloids and Surfaces a-Physicochemical and Engineering Aspects* **1998**, *142*, 49.

(37) Benko, G.; Skarman, B.; Wallenberg, R.; Hagfeldt, A.; Sundstrom, V.; Yartsev, A. P. *J. Phys. Chem. B* **2003**, *107*, 1370.

(38) Khazraji, A. C.; Hotchandani, S.; Das, S.; Kamat, P. V. *J. Phys. Chem. B* **1999**, *103*, 4693.

(39) Nuesch, F.; Gratzel, M. *Chem. Phys.* **1995**, *193*, 1.

(40) Widengren, J.; Seidel, C. A. M. *Phys, Chem. Chem. Phys.* **2000**, *2*, 3435.

(41) Sayama, K.; Hara, K.; Ohga, Y.; Shinpou, A.; Suga, S.; Arakawa, H. *New J. Chem.* **2001**, *25*, 200.

(42) Hara, K.; Tachibana, Y.; Ohga, Y.; Shinpo, A.; Suga, S.; Sayama, K.; Sugihara, H.; Arakawa, H. *Sol. Energy Mater. Sol. Cells* **2003**, *77*, 89.

(43) Stockwell, D.; Ai, X.; Anderson, N. A.; Kitamura, T.; Ikeda, M.; Shigaki, K.; Inoue, T.; Yanagida, S.; Lian, T. **Manuscript in preparation**.

(44) Furube, A.; Katoh, R.; Yoshihara, T.; Hara, K.; Murata, S.; Arakawa, H.; Tachiya, M. *J. Phys. Chem. C* **2004**, *108*, 12583.

(45) Furube, A.; Katoh, R.; Hara, K.; Murata, S.; Arakawa, H.; Tachiya, M. *J. Phys. Chem. B* **2003**, *107*, 4162.

(46) Gundlach, L.; Ernstorfer, R.; Willig, F. *Prog. Surf. Sci.* **2007**, *82*, 355.

(47) Wang, Y.; Hang, K.; Anderson, N. A.; Lian, T. *J. Phys. Chem. B* **2003**, *107*, 9434.

(48) Ghosh, H. N.; Asbury, J. B.; Weng, Y.; Lian, T. *J. Phys. Chem. B* **1998**, *102*, 10208.

(49) Duncan, W. R.; Stier, W. M.; Prezhdo, O. V. *J. Am. Chem. Soc.* **2005**, *127*, 7941.

(50) Gundlach, L.; Ernstorfer, R.; Willig, F. *Phys. Rev. B* **2006**, *74*, 035324/1.

(51) Verma, S. K., Prasenjit; Das, Amitava; Palit, Dipak K.; Ghosh, Hirendra N. *Journal of Physical Chemistry C* **2008**, *112*, 2918.

(52) Furube, A. K., Ryuzi; Yoshihara, Toshitada; Hara, Kohjiro; Murata, Shigeo; Arakawa, Hironori; Tachiya, M. *J. Phys. Chem. B.* **2004**, *108*, 12583.

(53) Stockwell, D.; Ai, X.; Anderson, N. A.; Kitamura, T.; Ikeda, M.; Shigaki, K.; Inoue, T.; Yanagida, S.; Lian, T. **Manuscript in preparation**.

(54) Hilgendorff, M.; Sundstrom, V. *Chem. Phys. Lett.* **1998**, *287*, 709.

(55) Ramakrishna, G.; Ghosh, H. N. *J. Phys. Chem. B* **2001**, *105*, 7000.

(56) Linquist, L. *Ark. Kemi.* **1960**, *16*, 79.

(57) Cordier, P.; Grossweiner, L. L. *J. Phys. Chem. B* **1968**, *72*, 2018.

(58) Marcus, R. A. *J. Chem. Phys.* **1965**, *43*, 679.

(59) Gao, Y. Q.; Georgievskii, Y.; Marcus, R. A. *J. Chem. Phys.* **2000**, *112*, 3358.

(60) Gao, Y. Q.; Marcus, R. A. *J. Chem. Phys.* **2000**, *113*, 6351.

(61) Gosavi, S.; Marcus, R. A. *J. Phys. Chem. B* **2000**, *104*, 2067.

(62) She, C.; Anderson, N. A.; Guo, J.; Liu, F.; Goh, W.; Chen, D.-T.; Mohler, D. L.; Tian, Z.-Q.; Hupp, J.; Lian, T. *J. Phys. Chem. B.* **2005**, *109*, 19345.

(63) Sakata, T.; Hashimoto, K.; Hiramoto, M. *J. Phys. Chem.* **1990**, *94*, 3040.

(64) Morigaki, K. *Physics of Amorphous Semiconductors*; Imperial College Press: London, 1999.

(65) Fujiwara, H.; Kondo, M. *Physical Review B: Condensed Matter and Materials Physics* **2005**, *71*, 075109/1.

(66) *Semiconductor Electrodes*; Finklea, H., O., Ed.; Elsevier: New York, 1988; Vol. 55.

(67) Button, K. J.; Fonstad, C. G.; Dreybrodt, W. *Phys. Rev. B* **1971**, *4*, 4539.

(68) Henrich, V.; Cox, P. *The Surface Science of Metal Oxides*; Cambridge University Press: Cambridge, 1996.

(69) Erbs, W.; Kiwi, J.; Gratzel, M. *Chem. Phys. Lett.* **1984**, *110*, 648.

(70) Bolts, J. M.; Wrighton, M. S. *J. Phys. Chem.* **1976**, *80*, 2641.

(71) She, C.; Guo, J.; Lian, T. *J. Phys. Chem. B* **2007**, *111*, 6903.

(72) Hilgendorff, M.; Sundstrom, V. *J. Phys. Chem. B* **1998**, *102*, 10505.

(73) Labat, F.; Ciofini, I.; Hratchian, H.; Frisch, M.; Raghavachari, K.; Adamo, C. *J. Am. Chem. Soc.* **2009**, *131*, 14290.

Chapter 7. Sum frequency vibrational spectroscopy study of molecular sensitizers to Au/TiO_2 interfaces

7.1. Introduction

In a dye sensitized solar cell (DSSC), a dye is adsorbed to the surface of semiconductor nanoparticles, where photoexcitation of the adsorbate promotes an electron to a higher electronic state, and in the presence of sufficient driving force the electron is transferred to the semiconductor conduction band. The rate of electron transfer has been described using Marcus theory, where one of the factors in determining rate is the matrix element describing coupling between donor and acceptor electronic states.[1-4] This coupling is correlated with the orientation of the adsorbate upon the surface as it anchors to the semiconductor. Using transient infrared and visible pump-probe absorption spectroscopy, our group has investigated electron-transfer kinetics of many dye-semiconductor systems.[5-9] In the course of these investigations, it has become of particular interest to determine the molecular orientation of these adsorbed dyes in order to gain a more quantitative picture of the overall electron transfer process.

Previous research by our group has dealt in part with a series of rhenium bipyridyl complexes that are linked to the semiconductor surface through carboxylate anchoring groups attached to the bipyridine ligands through varying lengths of methyl spacers.[5,9,10] These dyes, called ReCn, where n denotes the number of CH_2 spacers in the linking chain, have been shown to exhibit a dependence on electron transfer rate based on the value of n.[5,10] What is not known currently is whether orientation of these dyes changes as the methyl chain lengthens, possibly affecting the overall electron transfer rate from dye to accepting semiconductor. In addition, it is useful to determine any conformational change in the molecule upon photoexcitation and the subsequent electron transfer, which would aid in computational studies determining the electronic coupling between molecule and semiconductor to gain a better picture of the overall process. In order to begin a study of these ReCn systems, two dyes were chosen for initial probing on the surface of TiO_2 nanocrystalline thin films. These dyes, ReC0 and ReC1P, differ by one methyl spacer group and the anchoring group with which they adsorb to the semiconductor interface. The binding constant of the phosphonate anchoring group of ReC1P is higher than the binding constant of the carboxylate group of ReC0,[10] making it preferable in order to maximize the number of SF photons generated for orientational determination, where surface number density coverage is a factor in signal intensity.[11]

A major advantage in utilizing these dyes for an analysis of average molecular orientation stems from the three carbonyl (CO) ligands they contain. The ligands have three normal modes of vibration: two symmetric stretches denoted a’(1) and a’(2) at 2027 cm^{-1} and 1890 cm^{-1}, respectively, and an asymmetric stretch a” at 1926 cm^{-1};[12] these have been used in the past to monitor dye excited and oxidized state dynamics as a result of electron transfer to semiconductor nanoparticles.[13-15] The additional benefit of using SFVS to probe these normal modes is that the transition dipole moments lie reasonably orthogonal to each other in the molecular *xyz* plane. Assuming the molecules form a somewhat ordered monolayer on the adsorbate surface, SF signal intensity is critically dependent on the orientation of the dipoles with respect to the incident IR polarization. We show evidence that the detected SF signal intensity depends highly on incident beam polarization as a result of the orientation-dependent dipole moments of the three SF-enhanced CO stretching modes, allowing the possibility of calculation of the average orientation on nanocrystalline TiO_2 surfaces.

As a substrate, TiO_2 has been studied extensively, both for its use in dye-sensitized solar cells as an electron acceptor,[16-19] and as a crystalline surface for sensitization and surface modification.[20-22] Previous studies of methanol adsorption on a nanocrystalline TiO_2 surface were successful in determining adsorbate geometry,[23,24] and as a system ideally suited for this investigation, it was chosen in order to recreate the conditions found in a dye-sensitized solar cell on a relatively flat crystalline surface that would enhance SF photon generation. In order to show unambiguously that our observed SF signal from ReC1P on nanocrystalline TiO_2 is valid, we take a stepwise approach, beginning with a standard thiol sample well-described in the past attached to a PVD-deposited Au layer.[25-27] Modification of a thiol to attach ReC0 at the terminal end then allows us to take advantage of the large nonresonant response of Au to enhance our ReC0 signal, clearly observing the CO stretching modes associated with the dye. Finally, we use the total internal reflection (TIR) technique to observe ReC1P directly adsorbed at the nanocrystalline TiO_2 surface.

7.2. Results and Discussion

7.2.1 Au-enhanced Thiol SFVS Spectra

Initial alignment of the mid-IR beam was completed using a single element mercury-cadmium-telluride (MCT) detector, and the visible pulse was matched spatially with the mid-IR using a 200 μm pinhole. Temporal and final spatial overlap of the pulses was accomplished using two methods. First, a thin BBO crystal, which showed an intense SF signal upon proper temporal overlap of the pulses, was placed in the beam path to obtain the approximate delay at which the visible pulse overlapped the mid-IR pulse. Finally, a window of Z-cut isotropic quartz, which exhibits a large interfacial SF response, was placed at the beam overlap, and the signal collected by the SFVS apparatus. Minor spatial and temporal adjustments were made to optimize the signal size by adjusting the alignment of the mid-IR beam and delay timing of the visible pulse, respectively. To lower dark counts detected by the CCD and increase the signal to noise ratio, only strips of pixels that were illuminated by SF signal were binned together to create a spectrum, usually 25-30 strips out of the total 512. Additionally, 10-20 scans were collected that when signal-averaged together greatly decreased the background noise while ensuring reproducibility of the data. Because the spectral resolution of the experiments was ~12 cm^{-1}, limited by the bandwidth of the 799 nm visible pulse, and the resolution of the CCD was 1.2 cm^{-1}, the collected signal was also horizontally binned across 4 pixels. This preserved the resolution of the experiment while increasing the signal-to-noise in order to shorten acquisition times.

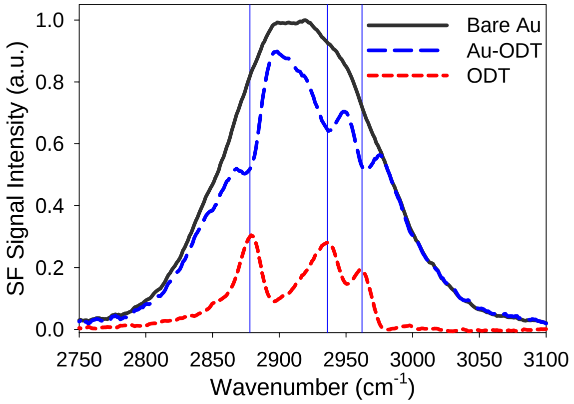

Figure 7.1: Au-enhanced SFVS spectrum of ODT used for calibration purposes. Bare Au nonresonant SF signal (solid black line) is compared with ODT-adsorbed Au (dashed blue line) and the ODT subtracted signal (short dashed red line). Methyl stretching peaks at 2877 cm^{-1} (CH_3 ν_s), 2937 cm^{-1} (CH_3 ν_s/CH_3 ν_b Fermi resonance), and 2964 cm^{-1} (CH_3 ν_{as}) agree well with previously published values[25] and are within the instrument resolution of the apparatus. Vertical blue lines denote literature values of the methyl stretching frequencies. The small shoulder at 2850 cm^{-1} corresponds to the CH_2 ν_s, observable due to disorder in SAM formation.

In order to calibrate the SFVS setup and ensure that the data collection methods as previously described were within the optimal conditions, a self-assembled monolayer (SAM) of octadecanethiol (ODT) on vapor-deposited Au was placed in the apparatus as an initial sample. ODT is known to bind strongly to the Au surface, forming a highly-ordered SAM that gives strong SF signal due to symmetry-breaking at the air-thiol interface where the surface density of terminal methyl groups is high.[28-30] The mid-IR intensity was tuned to overlap with the methyl stretching region of ODT, centered at ~2925 cm^{-1}, and a nonresonant SF spectrum of Au was collected as described previously.

The SF spectrum of ODT on Au was then collected, and the Au nonresonant background subtracted out. A comparison of these signals is shown in Figure 7.1. In Figure 7.1, the x-axis is plotted in terms of IR wavenumbers, which have been calculated based on the collected SF signal in the visible region and the peak wavelength of the narrowband upconversion pulse at 799 nm. When comparing the observed SF signal between the bare Au substrate (black line) and the ODT-functionalized Au (blue dashed line), the contributions to the ODT vibrational SF signal can clearly be seen as negative features. The subtracted spectrum indicating the pure SF vibrational spectrum of ODT (red dashed line) is inverted for comparison with the lineshape observed for Au-ODT. The vibrational bands corresponding to the stretching frequencies of the terminal methyl groups of ODT are clearly observed, where the peak at 2877 cm^{-1} corresponds to the symmetric methyl stretch ν_s, the peak at 2964 cm^{-1} corresponds to the antisymmetric methyl stretch ν_{as}, and the peak at 2937 cm^{-1} corresponds to a Fermi resonance between the methyl ν_s and an overtone of a methyl bending mode ν_b. The small shoulder at 2850 cm^{-1} corresponds to the methylene (CH_2) symmetric stretch ν_s of the alkyl chain between thiol anchoring group and terminal methyl group. This indicates that instead of having a perfectly trans configuration in the alkyl chain, disorder in SAM formation has led to defects in the alkyl chain arrangements, breaking the centrosymmetric environment between thiol and methyl groups, and allowing observation of vibrational features corresponding to the defects. The peak positions were compared to the original published values of SFVS of ODT on Au by Richter et al[31] and found to agree within 2 wavenumbers, shown as vertical blue lines in Figure 7.1, indicating that the spectrometer was well calibrated and observed SF signal is spectrally valid for the current setup.

The polarization combination used for both Au and Au-ODT samples was in the *ppp* configuration, which samples both interface-normal and in-plane vibrations at the interface. In a comparison of SF signal sizes in our lab using different polarization combinations *ppp*, *ssp* and *pss* (not shown), it was observed that the nonresonant SF enhancement due to the nonlinear response of Au was greatest using the *ppp* polarization combination.[32,33] In the cases where nonresonant background is significantly large, the observed SF signal can be described as being dominated by the cross terms in the expression for SF intensity, shown in Equation 7.1, which is described in terms of the interfacial nonlinear susceptibility $\chi^{(2)}$

$$I_{SF} \propto \left|\chi^{(2)}\right|^2 I_{vis} I_{IR} \tag{7.1}$$

where $\chi^{(2)}$ can be further broken into its individual contributions to SF signal from both the nonresonant susceptibility $\chi^{(2)}_{NR}$ and the vibrationally resonant molecular susceptibility $\chi^{(2)}_{\nu}$

$$\left|\chi^{(2)}\right| = \left|\chi^{(2)}_{NR} + \sum_{\upsilon} \chi^{(2)}_{\upsilon}\right| \tag{7.2}$$

It can be seen that the lineshape of the observed SF signal for ODT deviates from the expected Lorenztian profile given a purely resonant contribution from the thiol vibrational modes. This lineshape is due to the previously mentioned convolution of the interfacial susceptibility with the nonlinear response resulting in cross-term domination, the effects of which will be discussed in greater detail in the next section.

7.2.2. Au-enhanced ReC0-thiol SFVS Spectra

In order to observe the carbonyl vibrations of ReC0, taking advantage of the nonresonant signal enhancement given by the Au substrate surface, the use of a SAM of 11-mercaptoundecanol (11-MU) was employed to confirm adsorption of the thiol monolayer on the Au substrate surface. This was followed by covalently linking the terminal ends of the thiol layer through esterification of the ReC0 carboxyl anchoring groups to the terminal alcohol of 11-MU, and observing the new ReC0-modified sample.

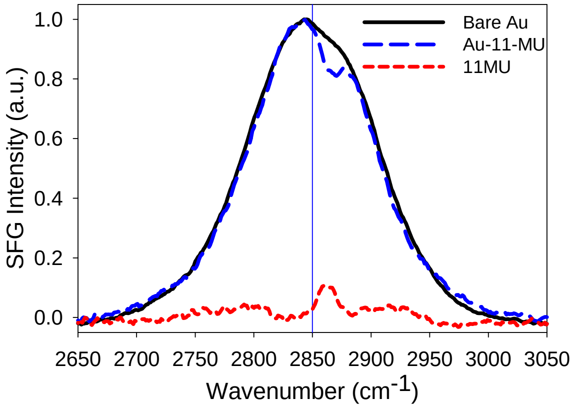

Figure 7.2: Au-enhanced SFVS spectrum of 11-MU to demonstrate thiol adsorption. Bare Au nonresonant SF signal (solid black line) is compared with 11-MU-adsorbed Au (dashed blue line) and the 11-MU subtracted signal (short dashed red line). The methylene symmetric stretching peak at 2850 cm^{-1} (CH_2 ν_s) and methylene antisymmetric stretching peak at 2923 cm^{-1} (CH ν_{as}) of 11-MU are significantly reduced in intensity due to alkane chain symmetry. The vertical blue line indicates the peak maximum of ν_s to compare to literature values.

Figure 7.2 shows a comparison of the observed *ppp*-polarization SF signal between the nonresonant signal from bare Au substrate (black line) and the 11-MU-functionalized Au (blue dashed line), as well as the subtracted SF signal resulting from the resonant contributions from the 11-MU monolayer. The subtracted spectrum indicating the pure SF vibrational spectrum of 11-MU (red dashed line) is inverted for comparison with the lineshape observed for Au-11-MU. The vibrational bands corresponding to the stretching frequencies of the alkane groups of 11-MU are clearly observed, where the peak at 2862 cm^{-1} corresponds to the symmetric methylene stretch ν_s, as indicated by the vertical blue line. In the case of 11-MU, the SF signal is considerably smaller compared to the signal observed for ODT in Figure 7.1, due to any resonant contributions being observed arising from gauche defects in the SAM alkyl chains of 11-MU from the methylene group prior to the hydroxyl tail at the end of the molecule as described previously, since the terminal OH group of 11-MU provides no resonant SF signal in this spectral region.[27,34,35] The hydroxyl group has a degree of flexibility to move at the end of the molecule, and in doing so introduces these defects in the methylene groups closest to it, breaking the local symmetry of the monolayer termination interface and allowing for generation of SF signal from the normally forbidden methylene groups.

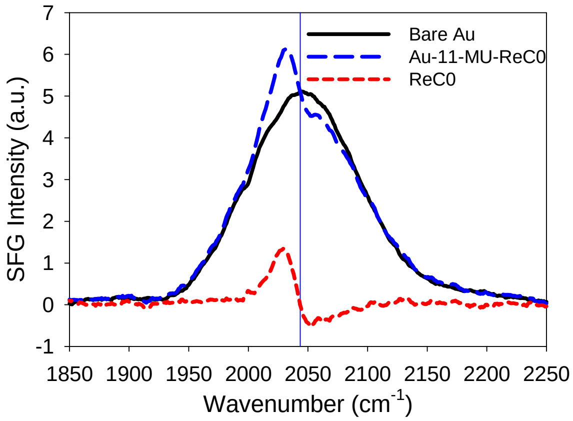

Figure 7.3: Au-enhanced SFVS spectrum of ReC0 observing the symmetric CO stretch a'(1) at 2027 cm^{-1}. Bare Au nonresonant SF signal (solid black line) is compared with ReC0-11-MU-adsorbed Au (dashed blue line) and the ReC0 subtracted signal (short dashed red line). The CO symmetric stretching peak at 2027 cm^{-1} is convoluted by the phase difference between $\chi_{NR}^{(2)}$ and $\chi_{v}^{(2)}$. The vertical blue line indicates the peak maximum of a'(1) to compare to literature values.[12]

Figure 7.3 shows a comparison of the observed *ppp*-polarization SF signal between the nonresonant signal from bare Au substrate (black line) and the ReC0-11-MU-functionalized Au (blue dashed line), as well as the subtracted SF signal resulting from the resonant contributions from the ReC0-functionalized thiol. The subtracted spectrum indicating the pure SF vibrational spectrum of ReC0 (red dashed line) is also shown to show the significance of the nonresonant contribution to the observed SF signal. The vibrational band corresponding to the CO symmetric stretching a'(1) peak of ReC0 at 2027 cm^{-1} is convoluted by the phase difference between $\chi_{NR}^{(2)}$ and $\chi_{v}^{(2)}$. The vertical blue line corresponds to the literature and experimentally observed FTIR frequency of the a'(1) CO mode.[12] The significant enhancement in SF signal intensity compared to that of

11-MU is due to the interfacial nature of ReC0 in the thiol SAM, where it sits at the boundary layer of air and linker termination. The a’(1) symmetric normal mode of the three CO ligands on ReC0 has an IR transition dipole that lies at a small angle relative to the interface normal when anchored to the thiol SAM by its carboxylate groups, leading to a high enhancement of generated SF photons.[36,37] With this experimental evidence it can be noted that normal modes of ReC0 adsorbed at an interface, specifically those with IR- and Raman-active transitions moments with a projection close to the interface normal, should result in high SF photon generation and provide for orientational analysis at a semiconductor-dye interface. We expect, and observe in our experimental results, that this normal dipole contribution to the overall susceptibility greatly increases the number of resonant SF photons, which is desired when the nonresonant enhancement of the Au substrate is removed and replaced with nanocrystalline TiO_2, which exhibits negligible nonresonant signal due to its high dielectric constant.

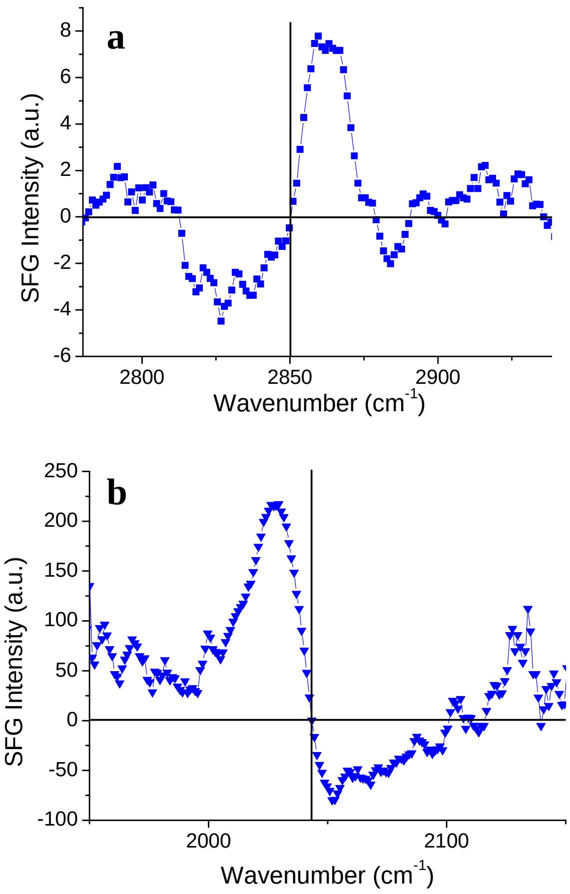

Figure 7.4: (a): Au-enhanced SFVS spectrum of 11-MU. The methylene stretching peak at 2850 cm^{-1} is weak due to signal arising from gauche defect symmetry breaking at the monolayer-air interface only. **(b):** Au-enhanced SFVS spectrum of ReC0-11-MU. The a'(1) symmetric mode of the CO ligands is greatly enhanced as a result of the transition dipole lying near interface normal. A signal enhancement from thiol to ReC0 of 30 times is observed as a result of the interface specificity. Differences in lineshape between the two spectra result from the relative phase of the vibrations with respect to the nonresonant background.

In order to qualitatively describe the complications involved with a strong nonresonant background convoluting the resonant SF lineshape, Figures 7.4a and 7.4b present a comparison of the observed SF signal from both 11-MU and ReC0-11-MU systems, where the signal for both samples was normalized to the acquisition time of 30 seconds in the *ppp* polarization configuration to take advantage of the Au nonresonant signal enhancement. In Figure 7.4a, the SF signal from the CH_2 symmetric stretch at 2850 cm^{-1} of 11-MU is observed to be ~30 times weaker than that of the CO symmetric stretch normal mode at 2040 cm^{-1} in Figure 7.4b after modification, which is expected given the interfacial symmetry involved in generating the molecularly resonant signal. However, because signal is observed for both unmodified and ReC0-modified 11-MU systems, differences can be explained about the detected signal with regards to the local environment for each system from which the signal arises.

When describing the nonlinear susceptibility that generates SF photons at an interface as shown in Equation 7.2, as mentioned previously, if the nonresonant contribution to the overall susceptibility is sufficiently large, it introduces cross terms into the generation of SF photons that significantly affect the lineshape from a typically resonant description, usually in a derivative manner. Using Equations 7.1 and 7.2, and assuming a single vibrational mode resonant within the electric fields experienced by a molecule, the SF intensity I_{SF} is shown to be proportional to

$$I_{SF} \propto \left|\chi^{(2)}\right|^2 = \left|\chi_{NR}^{(2)} + \chi_{\upsilon}^{(2)}\right|^2 \tag{7.3}$$

where following a quadratic relation,

$$\left|\chi_{NR}^{(2)} + \chi_{\upsilon}^{(2)}\right|^2 = \left|\chi_{NR}^{(2)}\right|^2 + 2\left|\chi_{NR}^{(2)}\chi_{\upsilon}^{(2)}\right| + \left|\chi_{\upsilon}^{(2)}\right|^2 \tag{7.4}$$

it is obvious that the large nonresonant contribution to the overall susceptibility is going to dominate the observed SF signal in the first two terms. Due to the coherent nature of the SFVS process, it is required to describe a relative phase between $\chi_{NR}^{(2)}$ and $\chi_{\upsilon}^{(2)}$

$$\left|\chi^{(2)}\right| = \left|\chi_{NR}^{(2)} + \sum_{\upsilon} \chi_{\upsilon}^{(2)} e^{i\gamma_{\upsilon}}\right| \tag{7.5}$$

that takes into account the instantaneous electronic response of the nonresonant susceptibility to the driving field and the molecular vibrational response with respect to the nonresonant contribution.

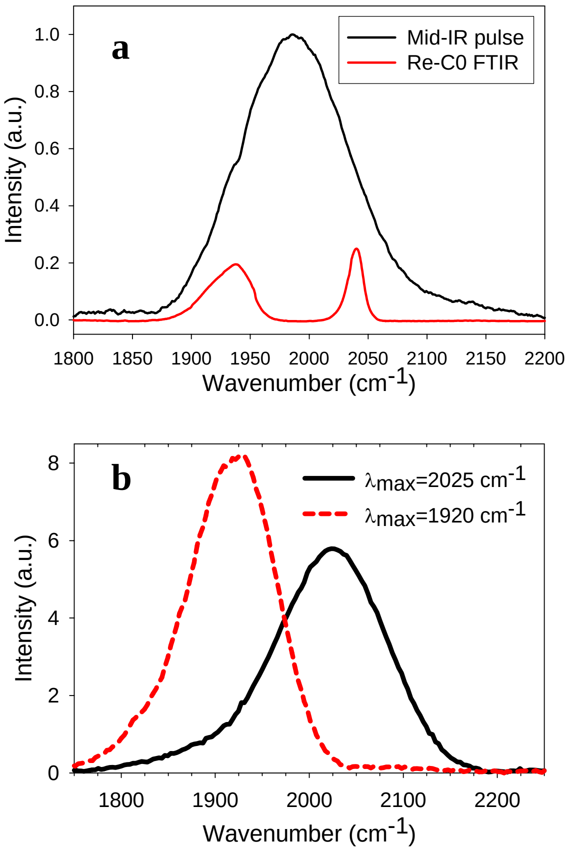

Figure 7.5: (a): Single-wavelength mid-IR pulse bandwidth measured with bare Au compared to the FTIR vibrational spectrum of ReC0. The mid-IR pulse is ~125 cm^{-1}

in bandwidth, while the ReC0 a’(1) and a’(2) modes are separated by ~140 cm^{-1}. **(b)** Demonstration of real-time mid-IR spectral shift under consecutive data acquisitions and relative intensities at different peak wavelengths for data normalization and scaling.

As observed in Figures 7.4a and 7.4b, the phases of the two vibrations for 11-MU and Re-C0 are nearly the opposite of each other with respect to the instantaneous nonresonant phase, which has been described in the literature as having a dependence on distance from the interface contributing the nonresonant susceptibility.[38,39] To this end, it was important to observe the relative phases of each individual carbonyl mode of ReC0 simultaneously in order to determine if the enhancement provided by the Au substrate was beneficial in the possibility of describing molecular orientation. As shown in Figure 7.5a, the SF signal obtained from bare Au, representing the total bandwidth of our mid-IR excitation pulse centered at 1985 cm^{-1}, gives as the spectral sampling range ~125 cm^{-1}, while the separation between various normal mode peaks in the vibrational spectrum of ReC0 CO ligands is ~140 cm^{-1}. This required that multiple mid-IR intensity profiles be collected at different peak wavelengths to avoid excessive noise enhancement when mid-IR intensity is below threshold levels for sufficient SF signal generation. In order to normalize the collected SF signal to mid-IR intensity and account for tuning-dependent mid-IR intensity changes, a standard Au sample was used to collect the wavelength-independent nonresonant SF signal at different mid-IR peak wavelengths in the *ppp* polarization combination. These wavelength standards, an example of which is shown in Figure 7.5b, provide intensity normalization and scaling without compromising data quality to low mid-IR intensity at different molecular resonant wavelengths. In Figure

7.5b, the two wavelengths defined were collected in real time under identical acquisition parameters by changing the frequency of our mid-IR excitation pulse. The intensities of the bandwidth profiles accurately reflect the intensity of the mid-IR bandwidth at each wavelength in order to better represent an entire SF spectrum of our Au-enhanced ReC0 sample.

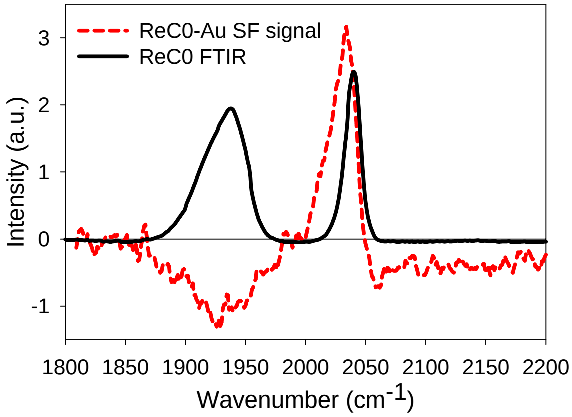

Figure 7.6: Comparison of the FTIR spectrum of ReC0 (black solid line) with the wavelength-scanned SF signal from ReC0-11-MU on Au substrate (red dashed line) showing the relative SF signal phase dependence on nonresonant susceptibility interaction.

Figure 7.6 shows the averaged results of the multiple mid-IR wavelength collection of SF signal, where the wavelengths observed correspond to the three normal mode frequencies of the ReC0 CO ligands. The black solid line in Figure 7.6 shows the standard FTIR vibrational spectrum of ReC0 for comparison to the Au-enhanced SF signal, shown as a red dashed line. In both spectra, the symmetric stretch a’(1) at 2027 cm^{-1} is shown to be separated from the symmetric stretch a’(2) at 1890 cm^{-1} and the asymmetric stretch a” at 1926 cm^{-1}, which are convoluted with each other into the single observed peak at lower frequency. As in previous examples of adsorbates attached to a Au surface, the SF spectrum represented in Figure 7.6 was collected in the *ppp* polarization configuration, where all normal modes are observed regardless of their surface orientation due to the high signal enhancement of the nonresonant background. It is immediately clear that there is a phase dependence on the modes observed, however, where both the a’(2) and a” modes exhibit a phase shifted by ~π when compared to the a’(1) mode. The parameters involved with fitting this phase dependence are outside the scope of this chapter, however, given that the necessary polarization dependence on SF mode intensity has not been sufficiently explored. The *ppp* polarization combination is utilized for its nonresonant enhancement properties rather than quantitative analysis of molecular orientation. However, from the SF signal shown in Figure 7.6, we can clearly see that the CO normal modes of ReC0 are observable in nonresonantly-enhanced SFVS, from which we expect to expand on moving towards a pure resonantly-enhanced SF spectrum.

7.2.3. Total Internal Reflection ReC1P SFVS Spectra

The signal enhancement provided by $\chi_{NR}^{(2)}$ of the Au surface is of significant value in terms of reducing data acquisition time, however introduces several complications in analysis of the recorded spectra. Most importantly, in order to fit the data to Equation 7.6

$$\left|\chi^{(2)}\right| = \left|\chi_{NR}^{(2)} + \sum_{\upsilon} \chi_{R_\upsilon}^{(2)} e^{i\gamma_\upsilon}\right| \tag{7.6}$$

the real part of the cross terms between $\chi_{NR}^{(2)}$ and $\chi_{R}^{(2)}$ dominate the spectra, leading to additional fit parameters involving the relative phase of each resonant contribution, both with regards to each normal mode observed and the nonresonant instantaneous phase, and the real and imaginary dielectric contributions from the nonresonant Au interface.[26] Coupled with this initial problem, $\chi_{NR}^{(2)}$ exhibits sensitivity to the polarization combinations being used, where the *ssp* combination (probing normal modes with interface-normal dipole moment projections) results in a nonresonant signal several orders of magnitude smaller than the *ppp* signal (probing all normal mode dipole moment projections), and *pss* signal (probing normal modes with interface-parallel dipole moment projections) is negligible, making an accurate determination of the $\chi_{NR}^{(2)}$ amplitude for a global fit of $\chi_{R}^{(2)}$ difficult in the absence of an external reference for each sample.[40] In parallel with this is the expected resonant signal size variation at different polarizations, making elimination of the nonresonant signal preferable in order to make an accurate measurement of adsorbate geometry.

In order to demonstrate the direct effects of removing the nonresonant susceptibility $\chi_{NR}^{(2)}$ from the observed signal, we compare two samples of ReC1P. By depositing a thin nanocrystalline layer of TiO_2 on a clean Au substrate as used in previous samples, we take advantage of the larger binding constant of ReC1P to TiO_2 where no structural modifications are necessary in order to directly attach the adsorbate to the interfacial substrate. In this case, we observe directly the Au nonresonant enhancement effect on SF signal lineshape. In comparison, by depositing the same nanocrystalline layer of TiO_2 on a CaF_2 prism, we take advantage of the total internal reflection (TIR) properties associated with incident beam angles greater than the critical angle of CaF_2 in collecting all surface SF photons generated by the evanescent wave at the TiO_2/ReC1P surface, resulting in a SF response purely dominated by the resonant contributions to the nonlinear susceptibility.

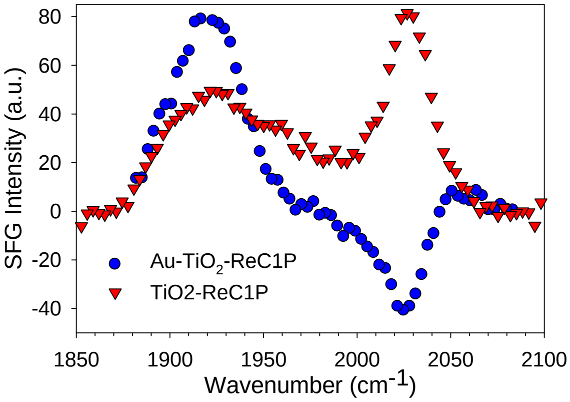

Figure 7.7: Comparison of the nonresonantly-enhanced SF spectrum of ReC1P adsorbed on TiO_2-deposited Au (blue circles) with the purely resonant total internal reflection SF signal from ReC1P adsorbed on TiO_2 (red triangles) showing the relative SF signal phase dependence on nonresonant susceptibility interaction.

Figure 7.7 shows a comparison of the Au nonresonantly-enhanced spectrum of ReC1P deposited on a thin layer of nanocrystalline TiO_2 (blue circles) with the total internal reflection SF spectrum of ReC1P adsorbed on TiO_2 (red triangles). The SF signal for both samples was collected in the *ssp* polarization geometry in order to show the dominance of the a’(1) normal mode with regards to interface normal. Of particular interest are the drastically different lineshapes of the two plots, resulting from the effect of whether $\chi_{NR}^{(2)}$ is negligible when compared to the size of $\chi_{R}^{(2)}$. It can be seen in the TIR spectrum of ReC1P that the mode with greatest intensity is the a’(1) mode, demonstrating the direct effect of probing the purely resonant dipole contribution near interface normal, while the intensities from the a'(2) and a" modes are significantly less, although their intensity indicates that they possess dipole components that can be projected on the interfacial z axis. In comparison, the convolution of the Au-enhanced ReC1P contains cross terms resulting from interference between all three normal modes with regards to the nonresonant background, generating a SF signal with both phase and nonresonant dependencies that makes analysis nontrivial. The signal resulting from $\chi_{NR}^{(2)}$ is a purely electronic effect due to material response at the interface, determined by the dielectric properties of the substrate. By removing the electronic response of the Au substrate in the TIR geometry, SF signal is no longer dominated by the convolution of $\chi_{NR}^{(2)}$ and $\chi_{R}^{(2)}$ and observed to be represented by the purely Lorentzian profiles of $\chi_{R}^{(2)}$, greatly simplifying spectral analysis.

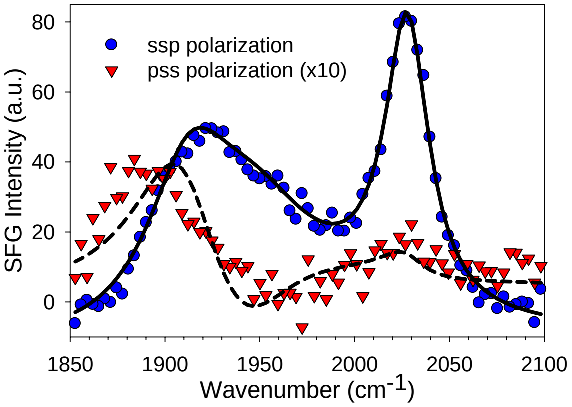

Figure 7.8: TIR SF spectra of ReC1P on TiO_2 at the polarization combinations *ssp* (blue circles) and *pss* (red triangles). The *pss* spectrum has been scaled by a factor of 10 for comparison to relative peak intensity. The solid lines are Lorentzian fits to the three CO normal modes at 2027, 1926, and 1890 cm^{-1}.

In order to demonstrate the polarization dependence of SF signal on total molecular orientation, we show the resonant TIR spectra of ReC1P at *ssp* (blue circles) and *pss* (red triangles) polarization combinations in Figure 7.8. The scale of the *pss* spectrum has been increased by a factor of 10 in order to observe qualitative differences between relative peak intensities. The lines in Figure 7.8 indicate global Lorentzian fits to the resonant peak positions in order to quantify peak intensity. The normal mode peak assignments are consistent with previously published infrared data, and are fixed to aid in the global fitting for normal mode peak analysis.[36,37] It is expected that the *pss* spectrum would be smaller in intensity than the *ssp* spectrum, as the tensor elements of $\chi_R^{(2)}$ that are probed in the *pss* beam geometry correspond to IR transition moments with components in the plane of the interface. Interface-normal transition moment contributions are observed with the *ssp* beam geometry, which have inherently less inversion symmetry at the interface resulting in a larger overall signal. Immediately evident is the large decrease in relative peak size of the symmetric stretch a’(1) at 2027 cm^{-1} between the *ssp* and *pss* polarization geometries. The transition dipole of the symmetric a’(1) mode has been shown to lie opposite the bipyridyl phosphonate anchoring groups of ReC1P,[36] in that the interface-normal projection of the dipole moment is expected to be larger than the interface-parallel projection up to a molecular tilt on the surface of ~45 degrees. Our results indicate that the projection of the a’(1) normal mode to interface normal as indicated in Figure 7.8, based on the intensities of the SF signal observed in the two polarization combinations, corresponds to an angular tilt of ~18 degrees. In the interface-plane spectrum represented by the *pss* geometry, we observe that the signal is dominated by the a’(2) stretching mode; the lack of a” antisymmetric mode in the *pss* signal while still appearing in the *ssp* spectrum indicates a degree of torsion in the molecule when compared to its presence in the interface normal projection. These results and further studies of the orientational dependence of ReC1P are still under investigation, making the present analysis uncertain. However, the unambiguous observation of a purely resonant SF vibrational response demonstrates that determination of molecular orientation is possible given the sufficient conditions described and demonstrated.

7.3 Summary

We have shown, through iterative molecular modification and adsorption schemes, that observation of dye-semiconductor systems is possible using the technique of sum frequency vibrational spectroscopy. In particular, the observation of such systems is enhanced by the nonresonant substrate response contributing to the nonlinear SF intensity, which convolutes the detected vibrational lineshape due to phase differences between the coherently excited adsorbate normal modes and the instantaneous electronic response of the substrate. We show that by removing the nonresonant enhancement of the substrate and using methods demonstrated to collect the maximum number of SF photons generated at a pure dye-semiconductor interface, it is possible to observe the orientational dependence on SF signal due to normal mode dipole projection under different probe polarization conditions. Further molecular orientational studies are being performed under the same conditions, and will expand on these studies.

References:

(1) Marcus, R. A. *J. Chem. Phys.* **1965**, *43*, 679.

(2) Gao, Y. Q.; Georgievskii, Y.; Marcus, R. A. *J. Chem. Phys.* **2000**, *112*, 3358.

(3) Gao, Y. Q.; Marcus, R. A. *J. Chem. Phys.* **2000**, *113*, 6351.

(4) Gosavi, S.; Marcus, R. A. *J. Phys. Chem. B* **2000**, *104*, 2067.

(5) Anderson, N. A.; Ai, X.; Chen, D.; Mohler, D. L.; Lian, T. *J. Phys. Chem. B* **2003**, *107*, 14231.

(6) Asbury, J. B.; Hao, E.; Wang, Y.; Ghosh, H. N.; Lian, T. *J. Phys. Chem. B* **2001**, *105*, 4545.

(7) Stockwell, D.; Yang, Y.; Huang, J.; Anfuso-Cleary, C.; Huang, Z.; Lian, T. *J. Phys. Chem. C* **2010 (accepted)**.

(8) Huang, J.; Stockwell, D.; Boulesbaa, A.; Guo, J.; Lian, T. *J. Phys. Chem. C* **2008**, *112*, 5203.

(9) She, C. A., Neil A.; Guo, Jianchang; Liu, Fang; Goh, Wan-Hee; Chen, Dai-Tao; Mohler, Debra L.; Tian, Zhong-Qun; Hupp, Joseph T.; Lian, Tianquan. *Journal of Physical Chemistry B* **2005**, *109*, 19345.

(10) She, C.; Guo, J.; Irle, S.; Morokuma, K.; Mohler, D. L.; Zabri, H.; Odobel, F.; Youm, K. T.; Liu, F.; Hupp Joseph, T.; Lian, T. *J. Phys. Chem. A.* **2007**, *111*, 6832.

(11) Buck, M.; Himmelhaus, M. *J. Vac. Sci. Tech. A* **2001**, *19*, 2717.

(12) Worl, L. A.; Duesing, R.; Chen, P.; Ciana, L. D.; Meyer, T. J. *J. Chem. Soc. Dalton Trans.* **1991**, 849.

(13) Ai, X.; Anderson, N. A.; Asbury, J. B.; Hao, E.; Lian, T. *Proceedings of SPIE-The International Society for Optical Engineering* **2003**, *5223*, 147.

(14) Wang, Y.; Asbury, J. B.; Lian, T. *J. Phys. Chem. A* **2000**, *104*, 4291.

(15) Guo, J.; She, C.; Lian, T. *J. Phys. Chem. C* **2007**, *111*, 8979.

(16) Asbury, J. B.; Anderson, N. A.; Hao, E.; Lian, T. *J. Phys. Chem. B* **2003**, *107*, 7376.

(17) O'Regan, B.; Gratzel, M. *Nature* **1991**, *353*, 737.

(18) Ellingson, R. J.; Asbury, J. B.; Ferrere, S.; Ghosh, H. N.; Sprague, J. R.; Lian, T.; Nozik, A. J. *Z. Phys. Chem. (Muenchen)* **1999**, *212*, 77.

(19) Tachibana, Y.; Moser, J. E.; Graetzel, M.; Klug, D. R.; Durrant, J. R. *J. Phys. Chem.* **1996**, *100*, 20056.

(20) Kataoka, S.; Gurau, M. C.; Albertorio, F.; Holden, M. A.; Lim, S. M.; Yang, R. D.; Cremer, P. S. *Langmuir* **2004**, *20*, 1662.

(21) Uosaki, K.; Yano, T.; Nihonyanagi, S. *J. Phys. Chem. B* **2004**, *108*, 19086.

(22) Chen, J.; Kubota, J.; Wada, A.; Kondo, J. N.; Domen, K. *J. Phys. Chem. C* **2008**, *112*, 12477.

(23) Wang, C.-Y.; Groenzin, H.; Schultz, M. J. *J. Phys. Chem. B* **2004**, *108*, 265.

(24) Wang, C.; Groenzin, H.; Schultz, M. J. *J. Am. Chem. Soc.* **2004**, *126*, 8094.

(25) Richter, L. J.; Petralli-Mallow, T. P.; Stephenson, J. C. *Opt. Lett.* **1998**, *23*, 1594.

(26) Bain, C.; Davies, P.; Ong, T.; Ward, R. *langmuir* **1991**, *7*, 1563.

(27) Hines, M. A.; Todd, J. A.; Guyotsionnest, P. *langmuir* **1995**, *11*, 493.

(28) Groat, K. A.; Creager, S. E. *langmuir* **1993**, *9*, 3668.

(29) Camillone, N.; Chidsey, C. E. D.; Liu, G. Y.; Putvinski, T. M.; Scoles, G. *J. Chem. Phys.* **1991**, *94*, 8493.

(30) Dhirani, A.; Hines, M. A.; Fisher, A. J.; Ismail, O.; Guyotsionnest, P. *langmuir* **1995**, *11*, 2609.

(31) Richter, L. J. P.-M., T. P.; Stephenson, J. C. *Opt. Lett.* **1998**, *23*, 1594.

(32) Cecchet, F.; Lis, D.; Guthmuller, J.; Champagne, B.; Caudano, Y.; Silien, C.; Mani, A. A.; Thiry, P. A.; Peremans, A. *ChemPhysChem* **2010**, *11*, 607.

(33) Zhang, H. P.; Romero, C.; Baldelli, S. *J. Phys. Chem. B* **2005**, *109*, 15520.

(34) Conboy, J. C.; Messmer, M. C.; Richmond, G. L. *langmuir* **1998**, *14*, 6722.

(35) Li, W.; Virtanen, J.; Penner, R. M. *J. Phys. Chem.* **1994**, *98*, 11751

(36) Gamelin, D. R.; George, M. W.; Glyn, P.; Grevels, F. W.; Johnson, F. P. A.; Klotzbucher, W.; Morrison, S. L.; Russell, G.; Schaffner, K.; Turner, J. J. *Inorg. Chem.* **1994**, *33*, 3246.

(37) Asbury, J. B.; Wang, Y.; Lian, T. *Bull. Chem. Soc. Japan* **2002**, *75*, 973.

(38) Lambert, A. G.; Neivandt, D. J.; Briggs, A. M.; Usadi, E. W.; Davies, P. B. *J. Phys. Chem. B* **2002**, *106*, 5461.

(39) Sovago, M.; Vartiainen, E.; Bonn, M. *J. Phys. Chem. C* **2009**, *113*, 6100.

(40) Briggman, K. A.; Stephenson, J. C.; Wallace, W. E.; Richter, L. J. *J. Phys. Chem. B* **2001**, *105*, 2785.